Alma Mater Studiorum · Università di Bologna

Scuola di Scienze
Corso di Laurea Magistrale in Fisica del Sistema Terra

Study of Jupiter's auroral regions through the measurements of the Juno/JIRAM instrument

Relatore:
Prof. Tiziano Maestri

Presentata da:
Chiara Castagnoli

Correlatori:
Dr. Bianca Maria Dinelli -
ISAC-CNR Bologna

Dr. Francesca Altieri -
IAPS-INAF Roma

Sessione II
Anno Accademico 2019/2020

Abstract

Lo strumento JIRAM (Jovian Auroral Infrared Mapper) a bordo della sonda spaziale Juno della NASA, in orbita attorno a Giove da luglio 2016, è stato progettato per eseguire il monitoraggio dell'atmosfera di Giove e delle sue aurore. Grazie all'orbita polare di Juno, i poli del pianeta sono stati osservati per la prima volta con una risoluzione spaziale molto più elevata di missioni spaziali precedenti. In questo lavoro di tesi, i dati di JIRAM, misurati nelle regioni polari, sono stati utilizzati per ricavare informazioni quantitative sulle specie CH_4 e H_3^+ e sulla variabilità della loro distribuzione spaziale. Gli spettri sono stati analizzati nella regione spettrale fra 3 μm e 4 μm, che è particolarmente favorevole per lo studio delle emissioni aurorali, a causa del quasi totale assorbimento della radiazione solare da parte degli strati più bassi dell'atmosfera Gioviana. A partire dai dati precedentemente analizzati per l'orbita JM0003 [Dinelli et al., Adriani et al. e Moriconi et al., 2017], il dataset è stato ampliato includendo osservazioni al di fuori degli ovali aurorali con un segnale più basso ed estendendo l'analisi ad orbite successive. Le prime orbite di Juno, dalla JM0003 alla JM0091, sono state esaminate per trovare quelle con una buona copertura delle zone polari da parte dello spettrometro e con un buon rapporto segnale rumore. Accanto all'orbita JM0003, sono state analizzate le orbite JM0071 e JM0081, risultate particolarmente promettenti per lo studio dell'aurora sud. Le misure spettroscopiche selezionate mostrano la presenza di emissioni di H_3^+ e CH_4 sia nell'aurora sud che nell'aurora nord e sono state analizzate usando una tecnica di inversione basata su un approccio di tipo bayesiano. Test preliminari hanno permesso di ottimizzare per il nuovo dataset il vettore di informazione a-priori e l'errore corrispondente. È stato inoltre possibile limitare i gradi di libertà dell'informazione alle sole abbondanze delle due specie emittenti e temperatura dell'H_3^+. Questo ha permesso di evitare l'insorgere nelle quantità ricavate di bias causati dalla forte correlazione con le altre variabili di stato (temperatura di CH_4 e alcuni parametri strumentali) e di diminuire i valori di χ^2. I risultati hanno confermato la presenza di una significativa concentrazione di metano in prossimità di entrambi i poli, all'interno dell'ovale aurorale, e abbondanze confrontabili di H_3^+ nelle due regioni aurorali, con valori generalmente compresi tra $2.0 \cdot 10^{12}$ cm^{-2} e $2.8 \cdot 10^{12}$ cm^{-2} e alcuni picchi superiori a $2.8 \cdot 10^{12}$ cm^{-2}. Le temperature dell'H_3^+ risultano invece inferiori nell'aurora sud, dove mediamente si osservano valori che non superano 825 K, mentre in corrispondenza dell'aurora nord le temperature si aggirano tra 800 K e 950 K. Il confronto di questi risultati con le immagini ricavate dalle osservazioni di JIRAM nella banda L ha inoltre consentito di studiare la morfologia delle aurore Gioviane e di evidenziare il dislocamento di alcuni gradi verso ovest dell'aurora sud nel periodo di tempo preso in esame.

Abstract

The Jovian Auroral Infrared Mapper (JIRAM) instrument aboard NASA's Juno spacecraft, which has been orbiting Jupiter since July 2016, was designed to monitor the atmosphere of Jupiter and its aurorae. Due to Juno's polar orbit, the poles of the planet have been observed with a much higher spatial resolution than previous space missions. In this thesis, JIRAM data measured over the polar regions, have been used to derive quantitative information on the species CH_4 and H_3^+ and on the variability of their spatial distribution. JIRAM spectra have been analysed in the spectral region from 3 to 4 μm, that is particularly favourable for the study of the auroral emissions, due to the quasi-total absorption of the incoming solar radiation from the lowest layers of Jupiter atmosphere. Starting from the data previously analysed for the orbit JM0003 [Dinelli et al., Adriani et al. e Moriconi et al., 2017], the dataset has been enlarged to include observations outside the auroral ovals with a lower signal and extending the analysis to successive orbits. The first Juno orbits, from JM0003 to JM0091, have been examined in order to find the ones with both good polar coverage of the spectrometer measurements and good signal to noise ratio. Along with the JM0003, the orbits JM0071 and JM0081 have been analysed, resulting particularly promising for the study of the southern aurora. The selected spectroscopic measurements show the presence of H_3^+ and CH_4 emissions in both the southern aurora and the northern aurora and have been analysed using an inversion technique based on a Bayesian approach. Preliminary tests have allowed to optimize for the new dataset the a-priori information vector and the corresponding error. It has also been possible to limit the degrees of freedom of the information to just the abundances of the two species and H_3^+ temperature. This has enabled to avoid the retrieved quantities to be affected by biases produced by the strong correlation with the other state variables (CH_4 temperature and some instrumental parameters) and to decrease the χ^2 values. The results have confirmed the presence of a significant concentration of methane near both poles, within the auroral oval, and comparable abundances of H_3^+ in the two auroral regions, with values generally ranging from $2.0 \cdot 10^{12}$ cm^{-2} to $2.8 \cdot 10^{12}$ cm^{-2} e some peaks larger than $2.8 \cdot 10^{12}$ cm^{-2}. Instead, the H_3^+ temperatures appear lower in the south aurora, where on average the values do not exceed 825 K, while in the northern aurora the temperatures span between 800 K and 950 K. The comparison of these results with the images obtained from the JIRAM's observations in the L band has also allowed to study the morphology of the Jovian aurorae and to highlight the displacement of a few degrees westward of the south aurora over the time.

Contents

Constants

h = 6.62607015 · 10^{-34} J·s Planck constant

k_b = 1.380649 · 10^{-23} J· K^{-1} Boltzmann constant

σ = 5.67 · 10^{-8} W· m^{-2} · K^{-4} Stefan-Boltzmann constant

c = 2.99792458 · 10^{8} $m \cdot s^{-1}$ speed of light

$c_2 = hc/k$ = 1.43878 $erg\ cm\ K$

Units of measurement

1 AU = 1.495978707 · 10^{11} m Astronomical Unit (average distance between the Earth and the Sun)

Introduction

Jupiter's aurorae were first observed by the ultraviolet spectrometer (UVS) on board of Voyager 1 spacecraft in 1979. Successively, in the 1990's, the Hubble Space Telescope collected several high-resolution images which showed bright emissions in Jupiter's polar regions, similar to those occurring on Earth, but much more intense. Actually, Jupiter exhibits the most powerful auroras of the Solar System and, just as the Earth, these auroral emissions can be considered the projection of the magnetospheric processes, such as the precipitation of energetic particles along the planet's magnetic field onto the upper atmosphere, where the collision with atmospheric gases causes the auroral phenomenon. After the discovery of the H_3^+ infrared spectrum by *Oka* (1980), and its detection in Jupiter's aurorae by *Drossart et al.* (1989), observations of the H_3^+ emissions have been used to study the complex Jovian auroral morphology and the magnetospheric mechanisms leading to the aurorae's occurrence. With this aim, the Jovian InfraRed Auroral Mapper (JIRAM) instrument, consisting in both an imager and a spectrometer has been developed and installed on board of the NASA Juno satellite. The imager of JIRAM acquires images in two spectral bands, M-band and L-band, where the L-band is dedicated to the auroral observations and allows detailed images of the H_3^+ distribution's morphology. The spectrometer measures the Jupiter spectrum in the spectral range from 2 μm to 5 μm over a slit featuring 256 pixels. This spectral range includes the infrared region from 3 to 4 μm, spectral range that is particularly suitable for mapping the H_3^+ thermal emissions, exploiting the absorption by methane of most of the light coming and reflected from the lower atmosphere. Since trihydrogen cations form because of the ionization processes in the upper atmosphere, H_3^+ lines can be detected thanks to the high contrast with respect to the dark background, enabling to map both H_3^+ concentration and temperature. During the first Juno's orbit around Jupiter a large number of measurements have been collected in the auroral regions, showing both the emissions of H_3^+ and of CH_4 in the 3-4 μm spectral range. Various analyses have then been performed on JIRAM's first sequence of observations of Jupiter's north and south poles. A first comparison of the UV and IR auroral features has revealed three main components of the aurorae's morphology: the main oval, the polar emissions (poleward of the main oval) and the satellite footprints (equatorward of the main emission) [Gerard et al. (2017)]. With the help of a retrieval code developed to analyse JIRAM spectra, the H_3^+ effective temperatures and column densities along the line of sight (LOS) of each observation have been retrieved. In particular, H_3^+ infrared emission lines have been used to derive the atmospheric temperature, being the trihydrogen cations thermalized by the surrounding neutral atmosphere shortly after their formation, while the integrated column densities retrieved from the

emission lines' intensity enabled the mapping of the ion distribution. Moreover, considering the detection of methane emissions in Jupiter's aurorae, in the retrieval analysis the CH_4 contribution to the spectral signature has been taken into account; therefore, together with the H_3^+ data, methane column density has been retrieved along the LOS [Dinelli et al. (2017); Adriani et al. (2017); Moriconi et al. (2017)]. In light of such results, this thesis is born with the purpose to integrate the work already done on JIRAM's auroral observations acquired at nadir over Jupiter's north and south pole during the first Juno's orbit and to extend it to the subsequent orbits where JIRAM provided an optimal coverage of the auroral regions. In fact, initially the focus of this work has been posed on the first ten orbits of Juno satellite. However, only two of them have a sufficient coverage to study the Jovian northern aurora, whereas four orbits have been considered for the southern auroral emissions. Throughout all the examined orbits around the planet, the Juno/JIRAM instrument collected tens thousands of spectra, but only the most promising ones have been selected and analysed using the retrieval code described by *Dinelli et al* (2017) to determine temperatures and column densities of H_3^+ and CH_4. The analysis's outputs have been further filtered to reject those with higher χ-test values and/or larger errors associated to the retrieved quantities and retain only the more reliable retrievals. Lastly, these ultimate results have been used to determine the morphological evolution of Jupiter's aurorae over time, from one orbit to another, by comparing the resultant horizontal distributions of H_3^+ and CH_4 temperatures and concentrations. Moreover, the final maps have been confronted with the images from the imager, which differently from the spectrometer, cannot discern the two emitting species. All the procedures and methodologies adopted to draw the final conclusions are here presented in Chapter 5, preceded by four theoretical chapters having the purpose to provide the necessary background information for better understanding the target of this work and to introduce the JIRAM instrument.

- Chapter 1 consists in a general introduction to molecular spectroscopy and radiative transfer theory.
- Chapter 2 presents the Bayesian approach used for the inversion of JIRAM measurements.
- Chapter 3 recalls the theory behind Jupiter and, in particular, describes the Jovian magnetosphere and the auroral phenomena.
- Chapter 4 provides an overview of the physics that drives the Jovian aurorae and an accurate description of Juno/JIRAM instrument.
- Chapter 5 focuses on the data analysis performed in this thesis and on the discussion of the final results.

1. Radiative Transfer

1.1 Molecular spectroscopy

Spectroscopy is the science concerned with the investigation and measurement of spectra produced when materials interact with or emit electromagnetic (EM) radiation [van der Meer (2018)]. Based on the study of the EM radiation emitted, absorbed, or scattered by molecules, chemical information and molecular structure (bond lengths, angles, energy levels etc.) can be found.

1.1.1 General principles

A molecule is usually defined as a system of atoms, whose properties depend on

- the type of atoms constituting the molecule;
- the spatial structure of the molecule, i.e. the way in which the atoms are arranged,
- the binding energy of atoms or atomic groups,

The molecule stability results from a balance among the attractive and repulsive forces of the positively atomic nuclei (positively charged) and electrons (negatively charged). The molecule's total energy resulting from these interacting forces can be sorted either as a potential energy or kinetic energy in

1. *Translational energy*: the kinetic energy of the molecules in a free environment due to their motion.
2. *Rotational energy*: the kinetic energy associated with the rotational motion of the molecules.
3. *Vibrational energy*: the oscillatory motion of the atoms or groups of atoms within a molecule, featuring a kinetic and potential energy exchange.
4. *Electronic energy*: energy stored as potential energy in excited electronic configurations.

Thus,

$$E_{mol} = E_{trans} + E_{in} = E_{trans} + E_{rot} + E_{vib} + E_{el} \tag{1.1}$$

where E_{mol} is the total molecular energy given by the sum of translational energy and internal energies (rotational, vibrational, and electronic). All these energies, except the translational one, are quantized: a quantum mechanical system (or particle) that is bond (i.e. spatially confined) can only assume certain discrete values, called *energy levels*. If a molecule (or atom) is at the lowest possible energy level, it and its electrons are said to be at the *ground state,* while if it is at a higher energy level, it is

said to be *excited*; also, if more than one quantum mechanical state is at the same energy, the energy level is said *degenerate*.

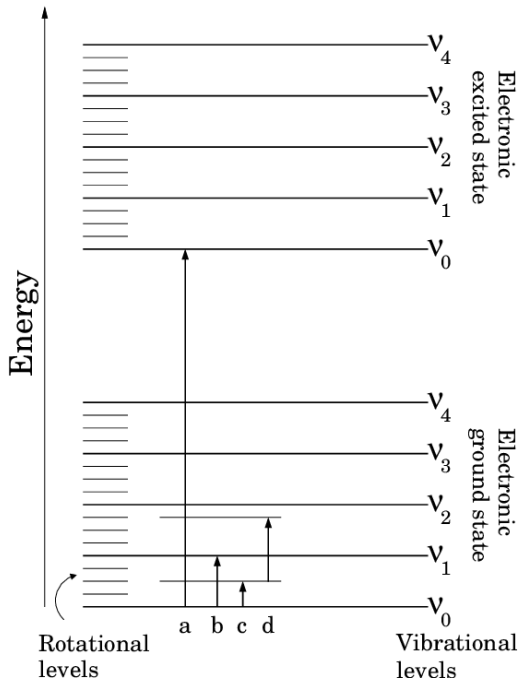

Fig 1.1 Molecular energy level diagram: (a) electronic transition, (b) vibrational transition, (c) rotational transition and (d) roto-vibrational transition.

A molecular spectrum results when a molecule undergoes the absorption or emission of EM radiation jumping from a quantized energy state to another (Fig 1.1), however not all the transitions are allowed. In this regard, quantum mechanics laws define which pairs of energy levels can participate in energy exchange and the extent of the radiation absorbed or emitted. In first place, the condition for the absorption of EM radiation by a molecule going from a lower energy state, E'', to a higher one, E', is that the frequency of the absorbed radiation must be related to the energy change, according to the relation

$$E' - E'' = h\tilde{\nu} = hc\nu \tag{1.2}$$

where, $h\nu$ is the energy of the absorbed or emitted electromagnetic radiation, h is the Plank's constant, ν is the radiation frequency, $\nu = \tilde{\nu}/c$ is the radiation wavenumber, E'' is the initial energy state and E' the final energy state (see section 1.3.1). This phenomenon is referred to as *stimulated absorption* (Fig 1.2b). On the other hand, if a molecule in an excited energy state interact with an EM radiation of frequency $\tilde{\nu}$, and the transition to a lower energy state results in the emission of additional radiation

at the same frequency $\tilde{\nu}$, this is the case of *stimulated emission* (Fig 1.2c). Also, emission can happen spontaneously (*spontaneous emission*) (Fig 1.2a), without the presence of inducing radiation.

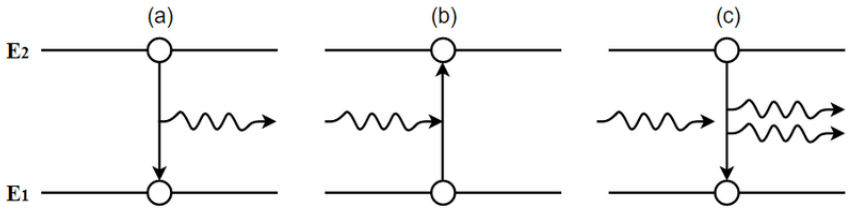

Fig 1.2 (a) spontaneous emission, **(b)** stimulated absorption and **(c)** stimulated emission.

According to what just said, the interaction of an electromagnetic radiation with the molecule can modify the incident wave, leaving a characteristic signature. For this interaction to take place, a force must act on the molecule in presence of an external magnetic field, and the existence of such a force does depend on the presence on the molecule of an electric or magnetic instantaneous dipole moment. In case of interactions through an electric dipole moment, the dipole moment $\vec{\mu}$ is directed from the negative to the positive charge and it is defined as

$$\vec{\mu} = \sum_i e_i \vec{d}_i \ [\mathrm{Cm}] \tag{1.3}$$

where e_i are the electronic charges and $\vec{d}_i$ are the relative position vectors. The moment induced per unit incident field is called polarizability of the molecule and it is related to the extent to which a molecule has a permanent dipole moment or can acquire an oscillating dipole moment through its vibrational motion.

1.1.2 Molecular spectra

The quantization of molecular energy levels and the resulting emission/absorption of radiation involving these levels depends on several mechanisms, as the interaction of the nuclei with each other and with the electrons. Thanks to their differences in magnitude, all these mechanisms, even if not clearly separated, can be examined independently by using a diatomic molecule model as an example.

Rotational energy levels

Molecules in gas phase are relatively far apart and free to rotate around their axis. Rotational energy depends on the moment of the inertia of the system, *I*: diatomic or linear triatomic molecules have two equal moments of inertia and two degrees of rotational freedom, while asymmetric top molecules have three unequal moments of inertia and three degrees of freedom (Fig 1.3, *left*).

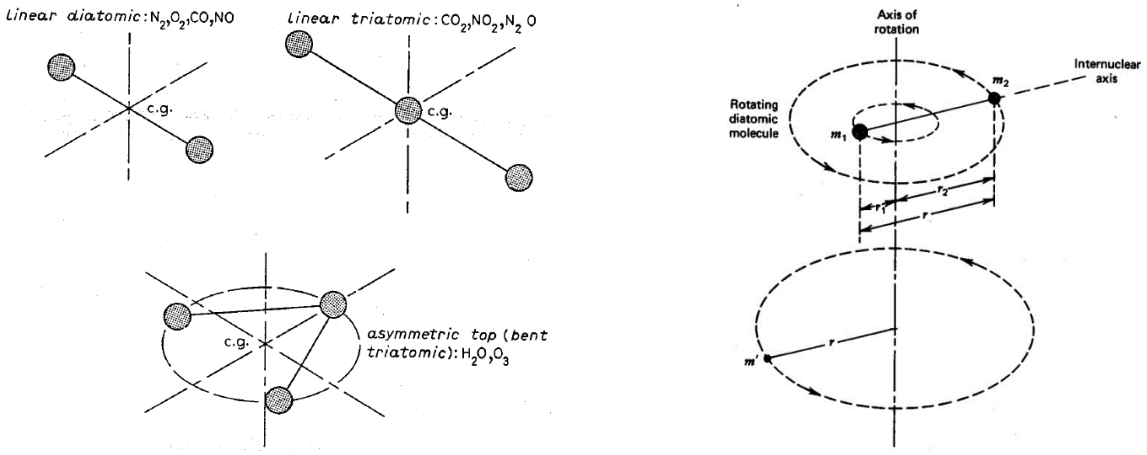

Fig 1.3 (*left*) Axes of rotational freedom for linear diatomic, linear triatomic and asymmetric top molecules. (*right*) Rigid rotor.

In quantum mechanics if a diatomic molecule is assumed to be rigid (internal vibrations are ignored), to predict its rotational energy a *linear rigid rotor* model can be used. The diatomic molecule is then considered to be a system of two-point masses, m_1 and m_2 located at fixed distances to their centre of mass, with an internuclear distance r (Fig 1.3, *right*). The moment of inertia is then estimated for each molecule as a function of the reduced mass m' and the internuclear distance r. For a two-body rigid rotator *I* is equal to

$$I = m_1 r + m_2 r = m' r \tag{1.4}$$

where the reduce mass is defined as $m' = \frac{m_1 m_2}{m_1 + m_2}$. Then, the kinetic energy of a rigid rotator is

$$E_{rot} = \frac{1}{2} I \omega^2 \tag{1.5}$$

While for a classical rotator the angular velocity ω, hence E_{rot}, can assume any value, for a quantized rotator quantum limitations occur, which result from a solution of the time-independent Schrödinger equation for reduced mass and null potential energy, i.e.

$$I\,\omega = \frac{h}{2\pi}\sqrt{J\,(J+1)}\,, \quad J = 0, 1, \ldots \tag{1.6}$$

where *J* is the *rotational quantum number*. Consequently, the quantized rotational energy can be written

$$E_{rot,\ J} = \frac{h^2}{8\pi^2 I} J(J+1) = BhcJ(J+1) \tag{1.7}$$

with $B = \frac{h}{8\pi^2 Ic}$, is called the *rotational constant.*

Molecular rotational spectra result when a molecule undergoes a transition from a rotational level to another. The allowed transitions are determined by quantum mechanics' selection rules, which are defined in terms of allowed change in the quantum number characterizing the energy states. For a diatomic molecule, a transition between two rotational energy levels can occur when

1. the diatomic molecule has a permanent dipole moment;
2. the quantum condition $h\tilde{\nu} = E_{J'} - E_{J''}$ is satisfied;
3. the selection rule according to which only transitions among adjacent *J*-levels are allowed is met: $\Delta J = \pm 1$.

According to these restrictions, the difference between two energy levels with lower and upper rotational quantum numbers $J'$and J''respectively ($J' = J'' + 1$) is

$$\Delta F = \frac{\Delta E}{hc} = BJ'(J'+1) - BJ''(J''+1) = 2BJ' = \nu_{rot} \tag{1.8}$$

where ν_{rot} (cm^{-1}) is the wavenumber of the spectral line resulting from the energy transition.

Vibrational energy levels

Real molecules are not rigid, as it is assumed when dealing with the rotational motion of a diatomic molecule: an aggregate of nuclear masses held together by elastic valence bonds can vibrate in one or more directions. In a diatomic molecule the two nuclei are in constant vibrational motion relative one

to another; therefore, it can be approximated to a *two-masses vibrator* with a natural harmonic frequency

$$\tilde{\nu} = \frac{1}{2\pi}\left(\sqrt{\frac{k_e}{m'}}\right) \tag{1.9}$$

where k_e is the *elastic force constant* characteristic of the particular molecule. The resulting potential energy of this system is

$$E_p = 2\pi^2 m' (r - r_e)^2 \tilde{\nu}^2 \tag{1.10}$$

where r_e is the equilibrium distance. As it is shown in Fig 1.4, the potential energy of a classical harmonic oscillator has a simple parabolic behaviour.

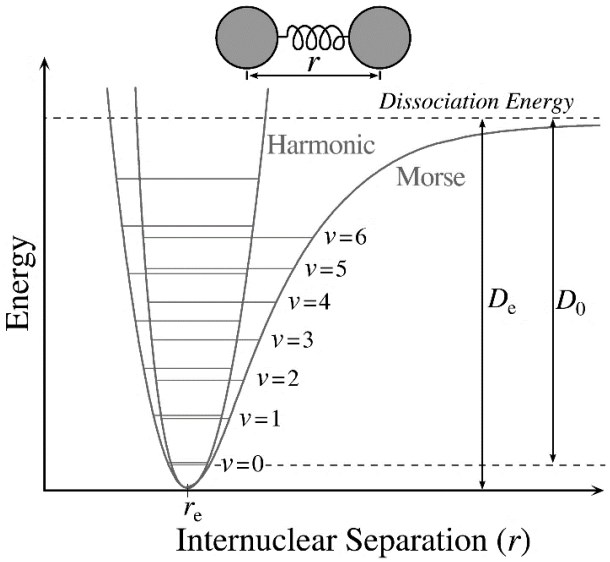

Fig 1.4 Potential energy of a harmonic and an anharmonic (Morse) two-masses vibrator (D_e is the binding energy for rigid molecule, hence the dissociation energy, while D_0 the true dissociation energy for non-rigid molecule due to the zero point energy of the lowest vibrational level).

By the resolution of the one-dimensional time-independent Schrödinger equation, the eigenvalues defining the allowed vibrational energy levels can be found:

$$E_\nu = \left(\nu + \frac{1}{2}\right) h\tilde{\nu} = \left(\nu + \frac{1}{2}\right) \frac{h}{2\pi}\sqrt{\frac{k_e}{m'}} \quad , \qquad \nu = 0, 1, \ldots \tag{1.11}$$

where ν is the *vibrational quantum number*.

Therefore, the conditions to observe a vibrational spectrum for a diatomic molecule are:

1. the change in the dipole moment of the molecule under vibration, which is not possible for a homonuclear diatomic molecule;
2. the quantum condition $h\tilde{\nu} = E_{\nu'} - E_{\nu''}$ has to be satisfied, where ν' is any level (except ν_0) and ν'' is the lower level;
3. the selection rule according to which only transitions among adjacent ν-levels are allowed is met: $\Delta\nu = \pm 1$.

As a result, the difference between the two adjacent energy levels is equal to

$$\Delta E_\nu = \frac{h}{2\pi}\sqrt{\frac{k_e}{m'}}\left[\left(\nu' + \frac{1}{2}\right) - \left(\nu'' + \frac{1}{2}\right)\right] = h\tilde{\nu} = hc\,\nu_{vib} \qquad (1.12)$$

where ν_{vib} is the wavenumber of the transition (the absorption by a molecule cause the depletion of the EM radiation of wavenumber ν_{vib}, resulting in a absorption spectral line). However, the harmonic oscillator, hence the parabolic curve, well represents the potential energy of vibrating molecules for transition from $\nu = 0$ to $\nu = 1$, while for larger vibrational quantum number the repulsive forces make the curve steeper when the bond length is reduced and less steep when it is expanded. The result is an empirical function called *Morse potential* (Fig 1.4), which better represents the reality: the vibrational energy levels become increasingly dense with large quantum numbers and at certain value ν, the molecule no longer vibrates but dissociates, because at larger distances the restoring force tends to zero (while the parabolic behaviour predicts an infinite increase of the potential energy with the increase of the internuclear distance).

Electronic energy levels

In a diatomic molecule the energy relations among nuclei and electros is more complex than for a single atom. In fact, electrons are not assigned to individual bonds between atoms, but are considered to move under the influence of the nuclei within the molecule. In order to describe the molecule's electronic structure, the *Molecular Orbital* theory (MO) is used. This approach builds on the electron wave functions of quantum mechanics to describe chemical bonding. As a matter of fact, electrons may be considered either a particle or a wave: an electron in an atom may be described as occupying an atomic orbital, or by a wave function Ψ which is a solution of the Schrödinger equation. According

to this method, the electronic wave functions of the individual atoms constituting the molecules, called the atomic orbitals (AOs), are combined to obtain the wave function of the molecular orbitals.

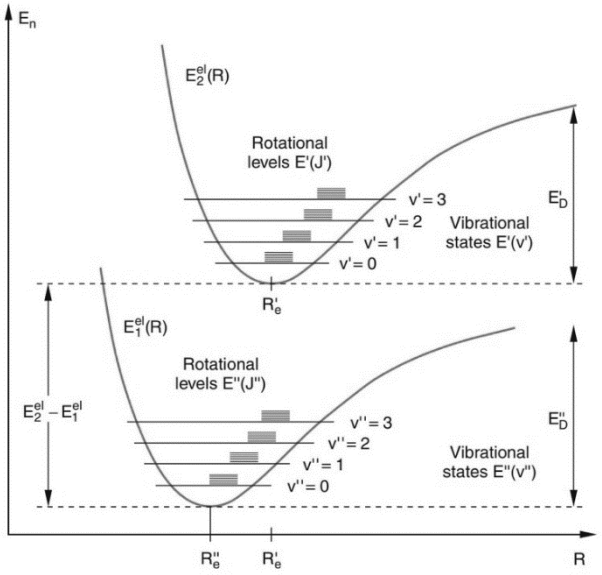

Fig 1.5 Rotational and vibrational levels in two different electronic states of a diatomic molecule.

The formation of molecular orbital occurs by the combination of atomic orbitals of proportional symmetry and comparable energy; therefore, the number of resulting molecular orbital is equal to the number of atomic orbitals, and while an atomic orbital is monocentric, a molecular orbital results to be polycentric. Consequently, molecular electronic spectra arise from the transition of an electron from a MO to another, where, since the diatomic molecule constantly undergoes vibrational motion, the potential energy of an electron in a particular MO is plotted relative to the internuclear separation in the molecule in a potential-energy diagram (Fig 1.5).

Roto-vibrational energy level

In real molecules the absolute separation of the different type of motions is rarely encountered. As it has already been mentioned, molecules without a permanent dipole moment can possess an oscillating dipole moment. A molecule in a given vibrational state can rotate, therefore each vibrational level is in reality divided into several rotational levels of energy equal to the sum of the vibrational and rotational energies. Being the difference among rotational energy levels of the order of 1-10 cm^{-1} , while the difference in the vibrational ones of the order of 1000 cm^{-1}, the difference of magnitude between the energy levels very often allows to separate the rotational levels belonging to one vibrational level to the ones belonging to another. Consequently, the more complex is the molecular

structure the higher is the number of the possible roto-vibrational transitions. For the simple case of absorption by a heteronuclear diatomic molecule with one degree of rotational freedom in the electronic ground state, the selection rules are $\Delta v = 1$ and $\Delta J = \pm 1$. Typically, at room temperature, only the ground vibrational state is populated $v'' = 0$, but several rotational states J may be populated. Therefore, the molecule can go to $v' = 1$, either to the next higher rotational level ($\Delta J = +1$), when the energy of the rotational transition is added to the energy of the vibrational transition, increasing the transition energy gap, or, conversely, to the next lower one ($\Delta J = -1$), when the transition energy gap is decreased. Then, the total energy given by the sum of rotational and vibrational energy can be written

$$E_v = Bhc\, J\,(J+1) + (v + \frac{1}{2})\,\frac{h}{2\pi}\sqrt{\frac{k_e}{m'}} \tag{1.13}$$

where the wavenumber of the corresponding absorption line is

$$v = \pm 2BJ' + \frac{1}{2\pi c}\sqrt{\frac{k_e}{m'}} \tag{1.14}$$

In a molecular roto-vibrational spectrum, the transition from one rotational level of the vibrational ground state to one rotational level in the vibrational excited state generates a spectral line and the assembly of the lines corresponding to a certain vibrational transition is called a *vibrational band*.

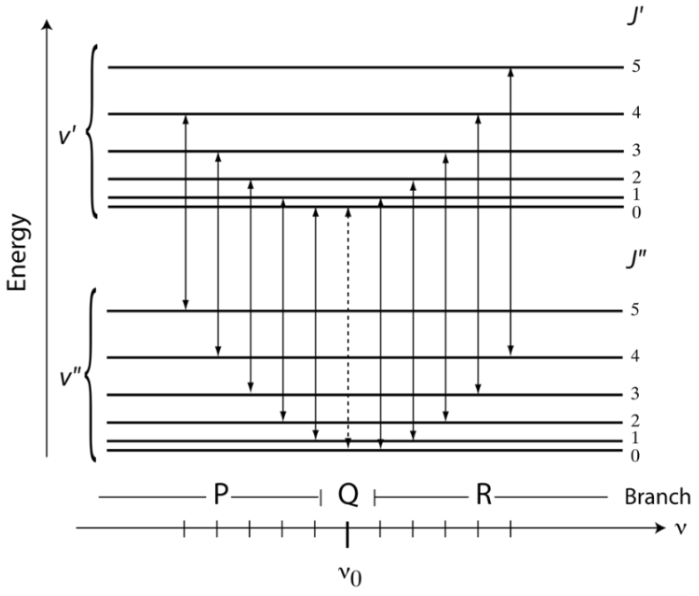

Fig 1.6 Relative positions in the spectrum of the roto-vibrational transitions for $\Delta v = \pm 1$ and $\Delta J = [-1, 0, +1]$.

As shown in Fig 1.6, the vibrational transitions belonging to the same vibrational band can be separated in the following branches

1. **P-branch** → The transitions with selection rule $\boldsymbol{\Delta J = -1}$ represented on the left of the central dotted vertical line. This group is the lower-energy, hence lower-frequency portion of the band.
2. **R-branch** → The transitions with selection rule $\boldsymbol{\Delta J = +1}$**,** represented on the right of the central dotted vertical lines**.** This group is the higher-energy, hence higher-frequency portion of the band.
3. **Q-branch** → It is the part of the infrared spectrum involving vibrational transitions with the same rotational quantum number in ground and excited states $(\boldsymbol{\Delta J = 0})$. The position of the Q-branch is then defined by the term ν_0.

The roto-vibrational spectra are also classified according to the direction of the dipole moment change vector:

- P-branch and R-branch are called *parallel branches* because the dipole moment oscillates parallel to the internuclear axis. For this vibrational mode, the transition $\Delta J = 0$ is forbidden, therefore no spectral line appears.
- Q-branch is called *perpendicular branch* because for perpendicular vibration the transition $\Delta J = 0$ is allowed.

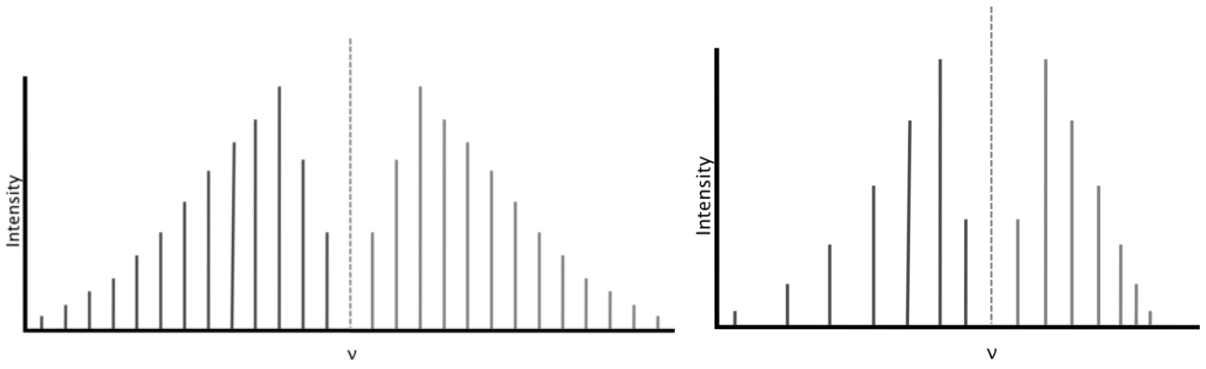

Fig 1.7 $(left)$ Ideal roto-vibrational spectrum and $(right)$ Real roto-vibrational spectrum.

Actually, the R-branch is not a perfect mirror of the P-branch, as it may appear from an ideal roto-vibrational spectrum $(\text{Fig } 1.7, \textit{left})$. For real molecules, due to the increased moment of inertia in higher vibrational levels and the consequent reduction of rotational energy, the distance between

rotational levels in the higher vibrational energy level v' is slightly smaller than in the v''; moreover, the frequency spacing between the spectral lines decreases with increasing frequency. Consequently, real roto-vibrational spectra show several asymmetric features (Fig 1.7, *right*).

Let now call $f_v = n_{X,v}/n_X$ the population fraction of the excited level v of a molecule X with respect to the number density of the molecule. At *thermal equilibrium*[1], f_v is given by the *Boltzmann factor,* i.e.

$$f_v = \frac{g_v e^{-(c_2 E_v/T)}}{Q_X(T)} \tag{1.15}$$

where g_v is the degeneracy factor of level v, c_2 is a constant and $Q_X(T)$ is the partition sum of molecule X at temperature T, given by

$$Q_X(T) = \sum_v g_v e^{-(c_2 E_v/T)} \tag{1.16}$$

1.2 Absorption spectra of gaseous molecules

As already seen, molecular spectra are much more complicated than those of atoms and three types of absorption (or emission) spectra can be observed, with different absorption features, as the ones represented in Fig 1.8, *left*:

1. *lines*: sharp lines of finite width.
2. *bands*: aggregation of lines.
3. *spectral continuum*: atmospheric absorption which do not exhibit a line-like structure and it varies smoothly with the wavelength.

While within liquids and solids the absorption and emission take place throughout a continuum spectrum of wavenumbers, due to the strong interaction between molecules, gases produce line spectra.

[1] The *thermodynamic equilibrium* is the state of a physical system in which the quantities that specify its properties remain unchanged and can be changed only at expenses of effects on other systems.

1.2.1 Spectral line shapes and absorption coefficient

An absorption line is defined by three main factors: the central position of the line, such as the central wavenumber ν_0, the strength (or intensity, S) of the line and the shape factor (or line profile, f). The condition for a strictly monochromatic absorption/emission to occur at ν and for the absorption line to appear like a Dirac δ-function, is that the energy involved for each gaseous molecule must be $\Delta E = hc\nu$. However, in the atmosphere three processes may cause the broadening of spectral lines:

1. *Natural broadening*
2. *Collision broadening*
3. *Doppler broadening*

which are individually explained below and are represented in Fig 1.8, r*ight*.

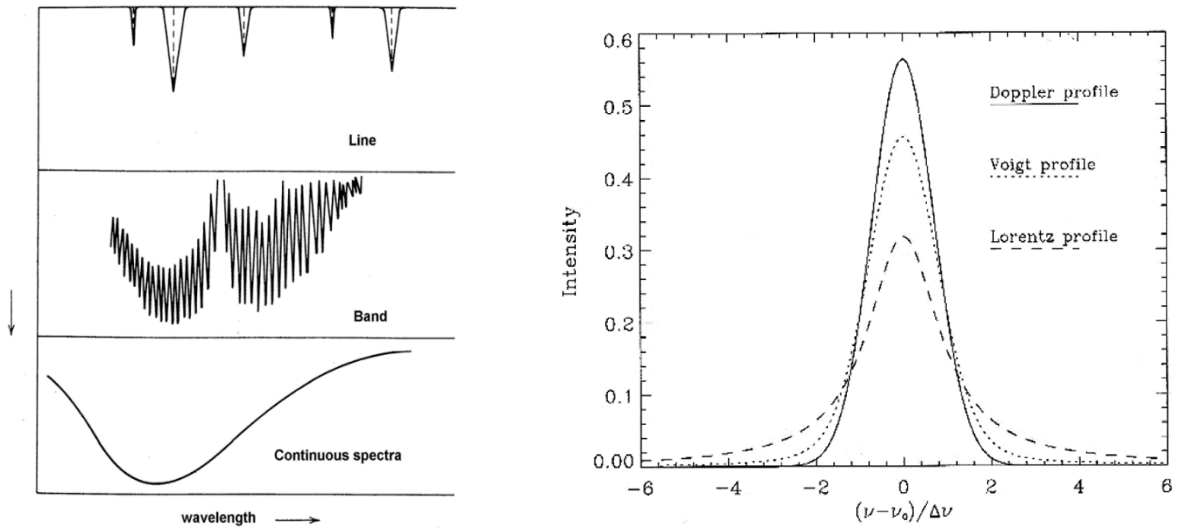

Fig 1.8 (*left*)Types of absorption/emission spectra: (*top*) lines, (*middle*) bands and (*bottom*) spectral continuum. (*right*) Comparison of normalized line broadening profiles, where ν is frequency and Δν is the Doppler width for the Doppler and Voight profiles and the Lorentz width for the Lorentz profile [Thomas (1999)].

1. *Natural broadening*

Every excited quantum state has finite duration, after which it spontaneously decays to the lower energy state. Due to their finite lifetime, energy levels are not infinitesimally narrow but have to be replaced by an energy distribution; therefore, the energy of a given state cannot be determined with infinitesimal precision. *Heisenberg's uncertainty principle* connects the uncertainty ΔE of the

energy E of any atomic system with its mean lifetime Δt. If ΔE and Δt are defined as the standard deviations of the respective distribution, the uncertainty principle demands

$$\Delta E \cdot \Delta t \approx \frac{h}{2\pi} \tag{1.17}$$

(h is the Planck constant). Consequently, a short lifetime will have a large energy uncertainty; hence,

$$\Delta \nu \approx \frac{\Delta E}{h} \approx \frac{1}{2\pi\, \Delta t} \tag{1.18}$$

it will result in a broadening of the spectral line. The *Michelson-Lorentz* theory predicts the shape of this broadened line, which correspond to a *Lorentzian line*:

$$k_N(\nu) = S f_N(\nu) = \frac{S}{\pi} \frac{\alpha_N}{(\nu - \nu_0)^2 + \alpha_N^2} \tag{1.19}$$

where $S = \int_{-\infty}^{+\infty} k_N(\nu)\, d\nu$ is the line strength and α_N the line half width, which corresponds to the distance from the centre of the line at half maximum power. The value of α_N is independent of wavelength and it is of the order of 10^{-5}nm.

2. *Collision broadening*

This broadening results from the variation of the molecular potentials, and consequently of the energy levels, caused by inelastic and elastic collisions between a molecule and the surrounding ones occurring during emission/absorption processes. When the partial pressure of the absorbing gas constitutes only a small fraction of the total gas pressure, the Michelson-Lorentz theory used before can be exploited; therefore, this *pressure broadening* follows a Lorentz line shape:

$$k_C(\nu) = S f_C(\nu - \nu_0) = \frac{S}{\pi} \frac{\alpha_C}{(\nu - \nu_0)^2 + \alpha_C^2} \tag{1.20}$$

where α_C , which is several order of magnitude greater than α_N, is inversely proportional to the mean free path, hence varies with pressure and temperature. Moreover, collisions between the same kind of particles produce a different broadening, called *self-broadening*, than the collisions with other molecules (i.e. occurring when we deal with a gas mixture), called the *foreign-broadening* that is evaluated as the average effect of the collisions between the separate gases.

3. *Doppler broadening*

Because in gas phase the molecules possess a Maxwell velocity distribution related to the temperature of the gas itself, in absence of collisions spectral lines exhibit a finite width. In fact, the components of the velocity along the direction of observation produce a Doppler effect, which shifts the apparent frequency of the emitted or absorbed radiance. Defining the probability to have a relative velocity u between the absorber and the observer (using the Maxwell law) $p(u) = \sqrt{\frac{m}{2\pi kT}}\ exp\left(-\frac{mu^2}{2kT}\right)$ and the Doppler shift for $u/c << 1$, $\nu - \nu_0 = \frac{\nu_0 u}{c}$, the Doppler line shape results

$$k_D(\nu) = Sf_D(\nu - \nu_0) = \frac{S}{\sqrt{\pi}\alpha_D}\ exp\left[-\frac{(\nu - \nu_0)^2}{{\alpha_D}^2}\right] \tag{1.21}$$

where the Doppler line half width is defined

$$\alpha_D = \frac{\nu_0}{c\sqrt{2kT/M_A}} \tag{1.22}$$

M_A is the molar mass.

1.2.2 Voigt profile

Because collisions are proportional to pressure, the collisional broadening dominates in those region of the atmosphere where the pressure is large, and therefore the broadening due to pressure is larger than the one due to temperature (e.g. Earth's troposphere); instead, the Doppler broadening is dominant where the molecules mean free path is large and the temperature broadening dominates (e.g. Earth's upper stratosphere). However, there are region where neither of the two processes dominates, thus the final line shapes can be represented by a convolution of the two: the collision broadened shape is shifted by the Doppler effect and averaged over the Maxwell distribution. The resulting profile is called *Voigt profile* (Fig 1.8, *right*) and it is defined as

$$f_V(\nu - \nu_0) = \int_{-\infty}^{+\infty} f_C(\nu' - \nu_0)\, f_C(\nu - \nu')\, d\nu' = \frac{\alpha_C}{\pi^{3/2}\alpha_D}\int_{-\infty}^{+\infty} \frac{1}{(\nu' - \nu_0)^2 + \alpha_C^2} exp\left[-\frac{(\nu - \nu')^2}{\alpha_D^2}\right] \tag{1.23}$$

which is a normalized function.

1.3 Atmospheric Radiation

1.3.1 Electromagnetic radiation

The electromagnetic radiation is an electric and magnetic disturbance traveling through space at the speed of light. The EM radiation has a dual nature, showing both wave and particulate properties. Electromagnetic waves can be classified in the electromagnetic spectrum (Fig 1.9) according to their wavelengths (λ) or frequency ($\tilde{\nu}$), which are connected to each other by the relation:

$$\lambda = \frac{c}{\tilde{\nu}} \tag{1.24}$$

where c is the speed of light in vacuum.

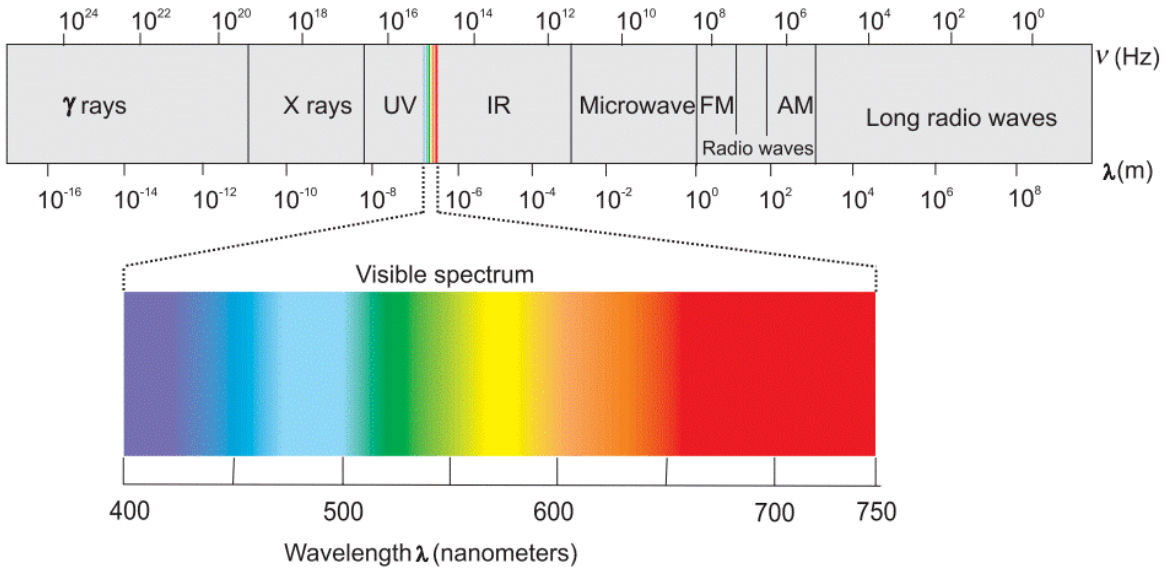

Fig 1.9 Electromagnetic spectrum.

The EM radiation can be classified (in increasing order of wavelength) as:

1. *Gamma radiation*

   A γ-ray is a penetrating form of electromagnetic radiation arising from the radioactive decay of atomic nuclei. It consists of the shortest wavelength electromagnetic waves ($\leq 3 \cdot 10^{-13}$m) that corresponds to the highest photon energy ($\geq$100 keV).

2. *X-radiation*

   An X-ray is a penetrating form of high-energy electromagnetic radiation. Generally, X-rays have a wavelength ranging from 10 pm to 10 nm and energies in the range 124 eV to 124 keV.

3. *Ultraviolet radiation*

   UV radiation constitutes about 10% of the total electromagnetic radiation output from the Sun and consists in an electromagnetic radiation whose wavelength ranges from 10 nm to 400 nm. Together with X-rays and γ-rays, short wavelength UVs are called *ionizing radiations*, because they can cause chemical reactions to take place or many substances to glow.

4. *Visible light*

   Visible light represents the region of the EM spectrum the human eye is most sensitive to. Typically, electromagnetic radiation with wavelengths between 380-760 nm, typically absorbed and emitted by electrons in molecules and atoms is perceived as visible light.

5. *Infrared radiation*

   Infrared is that part of the electromagnetic spectrum characterized by wavelengths extending from the nominal red edge of the visible spectrum at 750 nm to 1 mm. Any object with a temperature emits infrared radiation (IR), also known as *thermal radiation*. The wavelength at which a body radiates most intensely depends on its temperature; therefore, the infrared range is often subdivided into three regions, which are used for observation of different temperature ranges, and hence different environments in space.

   - *Near-Infrared* (NIR) [2500 -750 nm] → The physical processes that are relevant for this range are similar to those for visible light. Also, the highest frequencies in this region can be detected directly by many types of solid-state image sensors for infrared photography.
   - *Mid-Infrared* (MIR) [10 -2.5 μm] → The mid-infrared spectral region contains strong characteristic vibrational transitions of many important molecules, as well as two atmospheric transmission windows of 3-5 μm and 8-13 μm.
   - *Far-Infrared* (FIR) [1mm -10 μm] → Radiation within this range are typically absorbed by rotational modes in gas-phase molecules, by molecular motions in liquids, and by phonons in solids. Due to the strong absorption by water within this range, Earth's atmosphere appears opaque to FIR radiations; however, few wavelength ranges ("windows") allow their partial transmission and can be used for astronomy.

6. *Microwave radiation*

   MW radiation is a form of electromagnetic radiation with wavelengths ranging from about 1 m to 1 mm. Different from light and infrared radiations which are mostly absorbed by the surface, microwaves can penetrate into materials. Moreover, at the low end of this band the atmosphere is mainly transparent.

7. *Radio waves*

   Radio waves have the longest wavelengths in the electromagnetic spectrum, exhibiting frequency between 30 hertz (Hz) and 300 gigahertz (GHz). Radio waves are widely used to transmit information across distances in radio communication system (mobile phone, satellites, etc.). In fact, Earth's atmosphere is mainly transparent to radio waves, except for layers of charged particles in the ionosphere which can reflect certain frequencies.

Conventionally, to describe the radiation emitted from the sun the wavelength in micrometers (μm) is used. In the case of infrared radiation, it is conventional to use the wavenumber ν (cm^{-1})

$$\nu = \frac{1}{\lambda} = \frac{\tilde{\nu}}{c} \tag{1.25}$$

Finally, in the microwave region the frequency in gigahertz (GHz) is used.

Electromagnetic radiation can also be described as a stream of massless particles, called photons, having an energy

$$\varepsilon_{photon} = h\tilde{\nu} = h\,\frac{c}{\lambda} = hc\nu \tag{1.26}$$

where *h* is the Plank's constant.

1.3.2 Radiation Intensity and Flux

When radiative energy leaves a medium (e.g. a plane surface) end enters another, the resultant energy flux shows different strengths in different directions. Similarly, the EM radiation passing through any point inside any medium tends to be variable with the direction. Therefore, in order to quantify the intensity of the radiation in a certain direction it is necessary to introduce the concept of *solid angle,*

which is denoted with Ω and it is expressed in a dimensionless unit called *steradian* (sr). A solid angle is defined as the ratio between the area σ of a spherical surface intercepted at the core and the square of the radius, r

$$\Omega = \frac{\sigma}{r^2} \tag{1.27}$$

Therefore, it can be said that "the area of a surface on a sphere of unit radius is equivalent in magnitude to the solid angle it subtends", resulting both equal to 4π. A more relevant case to radiation emitted/received by a surface is that of the hemisphere, corresponding to a solid angle of 2π.

Let now consider a sphere with its central point in O and imagine a line starting from point O and intersecting a differential surface $d\sigma$ at distance r from the centre of the sphere. The resulting differential solid angle in polar coordinates $(\text{Fig } 1.10)$ is

$$d\Omega = \frac{d\sigma}{r^2} = sin\theta \; d\theta \; d\phi \tag{1.28}$$

where θ and ϕ are respectively the *zenith angle,* which is angle between the zenith $(\text{the point in the celestial sphere directly located on the observer's ascending vertical})$ and the direction observed, and the *azimuth angle*, namely the angle of the object around the horizon, usually measured from true north and increasing eastward.

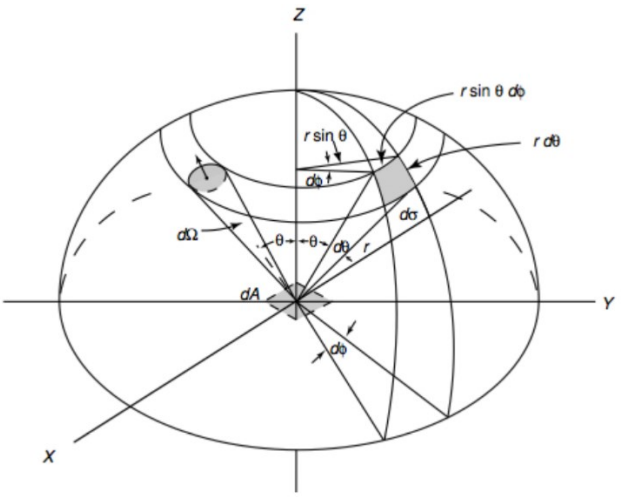

Fig 1.10 Differential solid angle in polar coordinates.

Once defined the solid angle, two concepts can be introduced: the *radiation intensity* $(\text{or } Radiance)$ and the *radiation flux* $(\text{or } Irradiance)$.

1. The *monochromatic Radiance,* L_λ → It is a directional quantity defined as the radiant energy (dE_λ) emitted, received, or transmitted by a surface (dA) per unit time (dt) per unit solid angle $(d\Omega)$ per unit area normal to the pencil of ray and per unit of wavelength $(d\lambda)$ (or frequency, $d\tilde{\nu}$), i.e.

$$L_\lambda = \frac{dE_\lambda}{dt\ d\Omega\ dA\ cos\theta\ d\lambda} \tag{1.29}$$

The SI unit for the radiance is $[W\ m^{-2}\ sr^{-1}\ \mu m^{-1}]$.

2. The *monochromatic Irradiance,* F_λ → It is defined as the integral over the entire hemisphere of the normal component of the radiance, i.e.

$$F_\lambda = \int_{2\pi} L_\lambda\ cos\theta\ d\Omega = \int_0^{2\pi} \int_0^{\pi/2} L_\lambda\ cos\theta\ sin\theta\ \ d\theta\ d\phi \tag{1.30}$$

where this relation in case of an isotropic radiation (the intensity of the radiation is independent of the direction) results

$$F_\lambda = \pi L_\lambda \tag{1.31}$$

The SI unit for the monochromatic Irradiance is then $[W\ m^{-2}\ \mu m^{-1}]$.

3. The *total Irradiance,* F → It is the flux density (energy per area per time) for all the wavelengths, obtained by integrating the monochromatic irradiance over the entire electromagnetic spectrum, i.e.

$$F = \int_0^\infty F_\lambda\ d\lambda \tag{1.32}$$

whit SI unit $[W\ m^{-2}]$. Similarly, the *total Radiance L,* can be obtained with unit $[W\ m^{-2}\ sr^{-1}]$.

1.3.3 Black body radiation

According to the third law of thermodynamics, all the matter at a temperature above the absolute zero emits energy in form of EM radiation, in all the directions and over a wide range of wavelengths. The studies of the radiation are based on an ideal body, the *black body,* which is a perfect emitter and absorber: it shows the maximum possible emission at all wavelengths and absorbs all the incident

radiation. The *black body radiance* can be expressed as a function of λ, $\tilde{\nu}$ or ν, in unit of energy/area/time/sr/wavelength, frequency, or wavenumber, using the *Plank's law* represented by these three relations

$$B_\lambda(T) = \frac{2hc^2}{\lambda^5}\frac{1}{e^{hc/\lambda k_b T} - 1}$$

$$B_{\tilde{\nu}}(T) = \frac{2h}{c^2}\frac{\tilde{\nu}^3}{e^{h\tilde{\nu}/k_b T} - 1}$$

$$B_\nu(T) = 2hc^2\frac{\nu^3}{e^{hc\nu/k_b T} - 1} \tag{1.33}$$

where k_b is the Boltzmann constant and T the absolute temperature of the body. The resulting distribution of black body radiance as a function of the wavelength is shown in Fig 1.11. The black body curve also exhibits an interesting behaviour: the maximum of intensity shifts to shorter wavelengths as the temperature increases, following the well know *Wien's law*

$$\lambda_{max} = \frac{2898}{T}(\mu m) \tag{1.34}$$

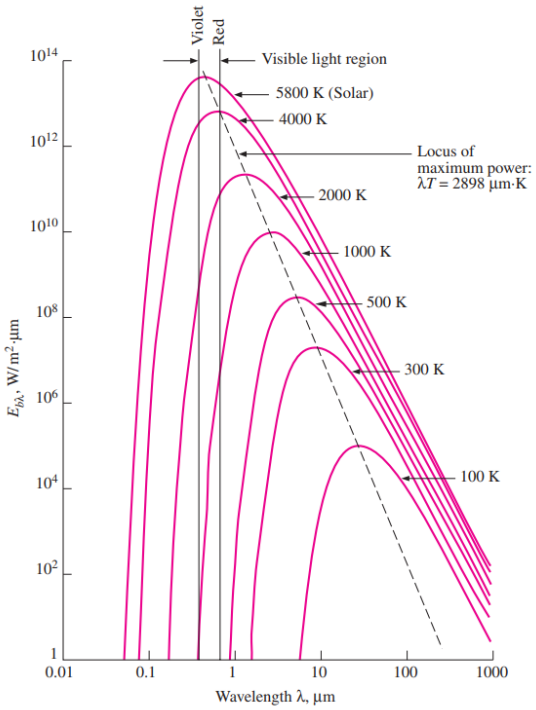

Fig 1.11 Spectral intensity distribution of Plank's back body radiation as a function of wavelength for different temperatures. The maximum of the intensity shifts to shorter wavelengths as the temperature of the black body increases.

Another important law is the *Stefan-Boltzmann law*, which can be obtained from the Plank's law, by firstly deriving the *spectral irradiance of a black body* exiting a plane surface

$$F_\lambda(T) = \int_{2\pi} B_\lambda(T) cos\theta d\Omega = \pi B_\lambda(T) \tag{1.35}$$

then, integrating it over the entire spectrum

$$F_\lambda(T) = \int_0^\infty \pi B_\lambda(T) d\lambda = \sigma T^4 \tag{1.36}$$

where σ is the Stefan-Boltzmann constant.

1.3.4 Absorption, reflection, transmission coefficients and emissivity

As already mentioned before, the temperatures of all objects are higher than the absolute zero, therefore they all are able to emit radiation. The definition of emissivity exploits the idea of the black body. As a matter of fact, the *emissivity* (ε) of a surface represents the ratio of the radiation emitted by the surface at a particular temperature to that emitted by a black body at the same temperature, and assumes values between 0 and 1. Therefore, the emissivity can be seen as a measure of how closely a surface approximate a black body, whose emissivity is equal to the unit. The emissivity varies not only with the surface's temperature, but also with the wavelength and the direction of the emitted radiation, hence it can be expressed as a *spectral directional emissivity* and defined as the ratio of the intensity of the radiation emitted by the surface at a specific wavelength in a certain direction to the intensity of radiation emitted by a black body at the same temperature and wavelength.

$$\varepsilon_\lambda(\theta, \phi, T) = \frac{L_\lambda(\theta, \phi, T)}{B_\lambda(\lambda, T)} \tag{1.37}$$

A more generic definition is that of *total hemispherical emissivity,* representing the ratio of the total radiation energy emitted by the surface to that of a black body of the same surface area at the same temperature, i.e.

$$\varepsilon(T) = \frac{L(T)}{B(T)} \tag{1.38}$$

Because bodies emit constantly, they are also bombarded by radiations coming from all the direction and at different wavelengths. When a radiation with a particular wavelength impacts a surface, part of it can be absorbed, part reflected, and part transmitted by the medium. In particular, the fraction of irradiation absorbed is called *absorptivity*, α_λ, the fraction reflected by the surface is called *reflectivity*, ρ_λ, and the fraction transmitted is the *transmissivity*, τ_λ, that are given by the ratio of the radiation energy incident on the surface with the portion of irradiation absorbed, reflected and transmitted, respectively. All these quantities have a value between 0 and 1, therefore the conservation of energy implies

$$\alpha_\lambda + \rho_\lambda + \tau_\lambda = 1 \tag{1.39}$$

where,

- black body, α_λ=1, ρ_λ=0, τ_λ=0
- perfect window, τ_λ=1, α_λ=1, ρ_λ=0
- opaque surface, τ_λ=0, $\alpha_\lambda + \rho_\lambda = 1$

It has to be noted that the absorptivity of a material is almost independent from the surface temperature: while the energy absorbed by a body depends on the incident electromagnetic radiation and on the absorptivity of the medium, the energy emitted depends on both emissivity and temperature.

1.3.5 Kirchhoff's law

The relation between the emission and the absorption of a real surface is described by the *Kirchhoff's law*. In order to introduce this law, let consider an object in a cavity whose interior walls radiate as a black body. Suppose, then, that the object and the walls are in radiative equilibrium, i.e. for the second law of thermodynamics they are at the same temperature. When a radiation arrives to the object at a certain wavelength and from a particular direction, the body absorbs a fraction α_λ of the incident radiation. Therefore, to conserve the radiative equilibrium the body must return the same monochromatic intensity at each wavelength and along each path. Remembering that the object and the walls of the cavity are at the same temperature, it follows that at all wavelength its emissivity must be equal to its absorptivity. This result is at the base of the Kirchhoff law, which states that a medium

in thermodynamic equilibrium with its environment can absorb radiation of a certain wavelength and at the same time emit radiation of that wavelength. Consequently, the emissivity of the medium at that wavelength, ε_λ, is equal to its absorptivity at the same wavelength, α_λ:

$$\varepsilon_\lambda = \alpha_\lambda \tag{1.40}$$

As underlined before, this relation requires the condition of thermodynamic equilibrium, which represents an ideal case, quite far from the real state of planetary atmospheres. However, in a localized volume, the atmosphere can be considered approximately isotropic and with a uniform temperature, where energy transitions are governed by molecular collisions. In this condition, called *local thermodynamic equilibrium* or *LTE,* the intrinsic properties of the atmosphere do vary in space and time, but much more slowly than the phenomenon under study; therefore, for any point one can assume the thermodynamic equilibrium conditions to be valid in some neighbourhood of that point. Consequently, the Planck function (which is derived under thermodynamic equilibrium conditions) can be used to represent the spectral radiance emitted by a given atmospheric layer and the Kirchhoff law can be applied.

1.2 Radiative Transfer theory

In order to introduce the equation of radiative transfer, let study *extinction* and *emission* processes. During an absorption process the radiative energy is turned into internal or kinetic energy, emission transforms internal or kinetic energy into radiative energy, whereas scattering involves the transfer of radiative to internal to radiative energy; therefore, the intensity of the radiation decreases when an extinction occurs and increases during emission. Let's consider extinction due to absorption of a beam passing through a thin atmospheric layer, *ds,* along a specific path. For each particle that the beam encounters, its monochromatic intensity is decreased by the increment

$$dL_\lambda = -L_\lambda \, k_{a\lambda} \, \rho_a \, ds \tag{1.41}$$

where ρ_a represents the mass density, while $k_{a\lambda}$ is defined as the *mass absorption cross section* $[m^2/kg]$, which depends on the pressure, the temperature and on the spectral features of the absorber (from now on the notation underlying the spectral dependence of k_a and L will be omitted for simplicity). This formula is referred to as the *Beer-Bouguer-Lambert's law.*

1.4.1 Radiative Transfer equation: Schwarzschild's equation

In order to determine the fraction of incident beam (or pencil of radiation) attenuated due to absorption, the previous equation may be integrated between 0 and *d,* thus

$$L(d) = L(0)e^{-\int_0^d k_a \rho_a ds} \tag{1.42}$$

This formula introduces the definition of path's *transmissivity*

$$Tr = e^{-\int_0^d k_a \rho_a ds} \tag{1.43}$$

where the exponential is a dimensionless number, called *optical depth* and denoted by τ, giving an estimate of how opaque a medium is to radiation passing through it. Assuming, then, to measure the attenuation from the top of the atmosphere (TOA, z=∞) downward in the nadir direction, the relation becomes

$$L = L_0\, e^{-\tau} \tag{1.44}$$

where L_0 represents the radiance at z=0. Based on the energy conservation discussed in section [1.3.4], in a non-scattering atmosphere the relation between absorption and transmission in an atmospheric layer of thickness Δz is given by

$$\alpha(\Delta z) = 1 - Tr \tag{1.45}$$

and assuming the atmospheric slab to be very thin, the transmissivity results $Tr \cong 1 - k_a\, \rho_a\, \Delta z$, hence $\alpha = \tau$. From here, suppose that the atmosphere is in LTE conditions, thus the Kirchhoff's law can be used to determine the radiation emitted per unit area by the atmospheric slab, i.e.

$$\varepsilon B(T) = k_a \rho_a \Delta z B(T) \tag{1.46}$$

The radiative transfer equation is then obtained by combining the absorption and emission processes, leading to the *Schwarzschild's equation* in a differential form:

$$dL = -L\, k_a \rho_a dz + B_a k_a \rho_a dz \tag{1.47}$$

Considering $d\tau(z) = -k_a\, \rho_a dz$, the RT equation can also be written as

$$\frac{dL}{d\tau} = L - B \tag{1.48}$$

which may be solved to give both the upward $\left(\text{or upwelling, } L^{\uparrow}\right)$ and downward $\left(\text{or downwelling, } L^{\downarrow}\right)$ intensities.

1.4.2 Schwarzschild's equation general solution

The equation RT equation found in the previous section can be solved by defining the monochromatic optical depth of a medium between two points s and s_1 $\left(\text{Fig 1.12a}\right)$ as

$$\tau(s_1, s) = \int_s^{s_1} k\rho ds' \tag{1.49}$$

Therefore, the differential form of the RT equation becomes

$$-\frac{dL(s)}{d\tau(s_1, s)} = -L(s) + B[T(s)] \tag{1.50}$$

By multiplying this result for $e^{-\tau(s_1,s)} \cdot d\tau(s_1, s)$ and by integrating the thickness from 0 to s_1, the general solution of the Schwarzschild's equation results

$$L(s_1) = L(0)\, e^{-\tau(s_1,0)} + \int_0^{s_1} B[T(s)]\; e^{-\tau(s_1,s)} k\rho ds \tag{1.51}$$

where the first term in the right-hand side of the equation represents the attenuation of the radiation intensity due to absorption by the medium, while the second term is associated to the medium's emission along the path from 0 to s_1.

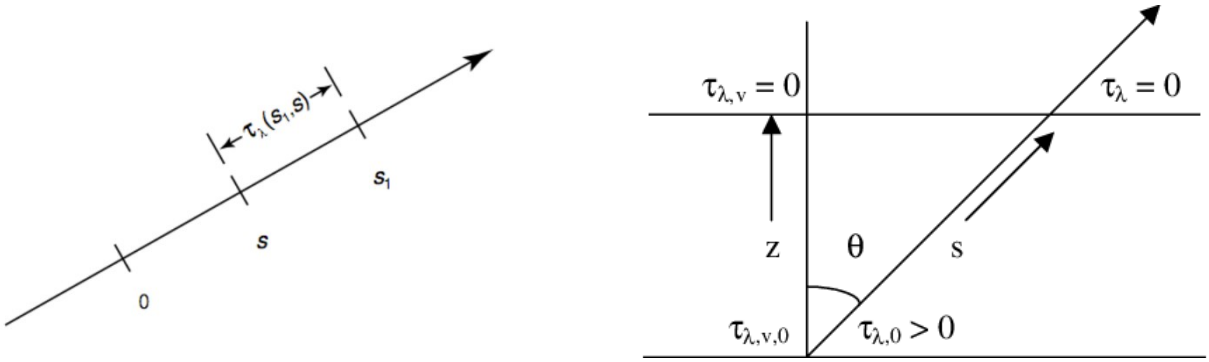

a **b**

Fig 1.12 (a) Schematic representation of the optical thickness of a medium between two point s and s_1. **(b)** Optical depth along a ray path in a plane parallel atmosphere [Sánchez-Bajo et al, 2002].

1.4.3 Plane-parallel approximation

To facilitates many radiative transfer calculations and deal with a complex atmospheric vertical structure, a *plane-parallel model,* as the one shown in Fig 1.12b, can be used. This approximation consists in a set of atmospheric layers characterized by homogeneous properties; therefore, temperature and densities of the various component is assumed to vary with the high (or pressure) only. Traditionally, the vertical coordinate z is used to measure linear distances:

$$z = s \cdot cos\theta = s \cdot \mu \quad \rightarrow \quad ds = \frac{dz}{cos\theta} = \frac{dz}{\mu} \tag{1.52}$$

where θ is the zenith angle. With this approximation the flux density, passing through a certain atmospheric level either up- $(\uparrow, \mu > 0)$ or downward $(\downarrow, \mu < 0)$, is given by

$$F^{\uparrow\downarrow}(\tau) = \int_{2\pi} L^{\uparrow\downarrow}(\tau, cos\theta)\, cos\theta\, d\Omega = 2\pi \int_0^1 L^{\uparrow\downarrow}(\tau, \mu)\, \mu d\mu \tag{1.53}$$

The *flux transmissivity* of a layer can be approximated to the intensity transmissivity of parallel beam radiation passing through it with an *average* (or *effective*) *zenith angle* of $\theta = 53°$

$$Tr^f = 2\int_0^1 e^{-\tau/\mu}\,\mu d\mu \cong e^{-\tau/\bar{\mu}} \tag{1.54}$$

where $1/\bar{\mu} \equiv sec\ 53° = 1.66$, is the *diffusivity factor.* Consequently,

$$F^{\uparrow\downarrow}(\tau) = \pi L^{\uparrow\downarrow}(\tau, \bar{\mu}) \tag{1.55}$$

Conventionally, the optical depth τ is measured downward from the top of the atmosphere ($\tau_{top} = 0$ and it increases for z decreasing) along the vertical optical path dz and it is defined as a measure of the light path in unit of the mean free path of photons ($l = 1/k\rho$). In fact, when

- $\tau = 1$ the intensity of the beam falls by $1/e$ over one mean free path
- $\tau \ll 1$ the medium is said to be transparent or *optically thin*
- $\tau \gg 1$ the medium is said to be opaque or *optically thick*

1.5 The Einstein coefficients

Kirchhoff's law, described in section 1.3.5, implies a relationship between emission and absorption at a microscopic level. This relation was first discovered by Einstein, who studied the properties of the single radiative transitions that couple matter with radiation. Let consider an ensemble of molecule X and the simple case of two discrete energy levels (Fig 1.13): the first of energy E, with a statistical weight g_1 and the other of energy $E + h\nu_0$ and a statistical weight g_2. As already seen in section 1.1.1, the radiative transition between this two levels are governed by three processes, which are here resumed to introduce the Einstein coefficients.

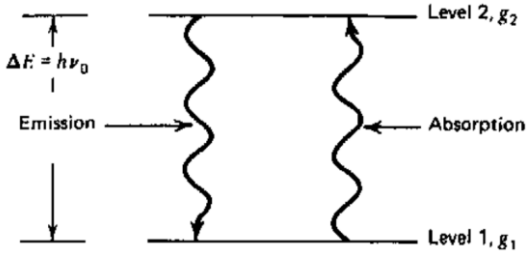

Fig 1.13 Emission and absorption from a two levels atom.

1. *Spontaneous emission*

   This transition occurs when the system is in level 2 and drops to level 1 emitting a photon, and it occurs even in absence of a radiation field. In this case the Einstein A-coefficient, $\boldsymbol{A_{21}}$, is defined as ***the transition probability per unit time for spontaneous emission*** $[s^{-1}]$.

2. *Absorption*

   This occurs when the system makes a transition 1→2 by absorbing a photon of energy $h\nu_0$. Since there is no self-interaction of the radiation field, the probability per unit time of this process is proportional to the density of photons (or the mean intensity) at frequency $\tilde{\nu}_0$, namely where the line profile function $\phi(\tilde{\nu})$ peaks. Therefore, **the transition probability per unit time of absorption** is defined as $\boldsymbol{B_{12}} \cdot \bar{\boldsymbol{J}}$, where $\bar{J}$ $[\mathrm{erg\,cm^{-2}\,s^{-1}\,cm}]$is the local mean radiance at the transition energy $h\nu_0$, while B_{12} $[\mathrm{cm^3 erg^{-1} cm^{-2}}]$ is the Einstein B-coefficient.

3. *Stimulated emission*

   Simulated emission is proportional to $\bar{J}$ and causes the emission of a photon. Therefore, ***the transition probability per unit time for simulated emission*** is defined as $\boldsymbol{B_{21}} \cdot \bar{\boldsymbol{J}}$, where B_{12} $[\mathrm{cm^3 erg^{-1} cm^{-2}}]$ is another Einstein B-coefficient.

The relation between these three coefficients can be obtained using a statistical approach first proposed by Einstein. Let consider an ensemble of molecules at equilibrium at temperature T with radiation. In thermodynamic equilibrium (TE) the number of transitions per unit time per unit volume out of state 1 is equal to the number of transition per unit time per unit volume into state 1. Therefore, defining n_1 and n_2 as the number densities of atoms in level 1 and 2, respectively, this reduces to

$$n_1 B_{12} \bar{J} = n_2 A_{21} + n_2 B_{21} \bar{J} \tag{1.56}$$

where in TE the Boltzmann expression [see section 1.1.2, formula (1.15)] for the levels' population ratios is

$$\frac{n_1}{n_2} = \frac{g_1 e^{(-E/k_b T)}}{g_2 e^{[-(E+h\nu_0)/k_b T]}} = \frac{g_1}{g_2} e^{(h\nu_0/k_b T)} \tag{1.57}$$

Therefore, combining (1.56) with (1.57), and solving for $\bar{J}$

$$\bar{J} = \frac{A_{21}/B_{21}}{(n_1/n_2)(B_{12}/B_{21}) - 1} = \frac{A_{21}/B_{21}}{(g_1 B_{12}/g_2 B_{21}) e^{(h\nu_0/k_b T)} - 1} \tag{1.58}$$

and expressing the mean radiance with the Plank function at temperature T, the *Einstein relations* result:

$$\begin{gathered} g_1 B_{12} = g_2 B_{21} \\ A_{21} = \frac{2h\nu^3}{c^2} B_{21} \end{gathered} \tag{1.59}$$

These relations reflect the radiative properties A_{21}, B_{12} and B_{21} of a single molecule and, different from the Kirchhoff's law, do not refer to the temperature T; therefore, even though they have been obtained in an equilibrium configuration, must hold whether or not the atoms are in thermodynamic equilibrium and can be considered an extension of the Kirchhoff's law to include the nonthermal emission when the matter is not at TE.

1.6 Remote Sensing

Remote sensing is based on the interpretation of the radiometric measurements of the EM radiation in specific spectral intervals, which are sensitive to some physical property of the medium. Therefore, Remote Sensing can be defined as the science to obtain information on a target (object, area, or phenomenon) from distance, by sensor mounted on platforms (e.g. satellites) that use the entire electromagnetic spectrum. Remote sensing instruments can be classified into two categories: active or passive. An active sensor generates its own signal, which is successively measured when reflected, refracted, or scattered by a planetary surface or its atmosphere. A passive sensor is designed to receive, and measure either the natural emissions produced by constituents of the surface or atmosphere of a planet or the radiation emitted by an external source (typically the Sun or a star) and absorbed by the atmosphere.

1.6.1 Brightness Temperature

Many objects do not emit like black body; however, any measured spectral radiance can be represented as the radiation that a blackbody at a given temperature will emit. Moreover, applying the inverse of the Plank function to the measured radiation, a descriptive measure of the radiation in terms of temperature can be obtain:

$$T_b = \frac{hf}{k_b ln\left(1 - \frac{2hf^3}{c^2 L_f}\right)} \tag{1.60}$$

This formula represents the *Brightness Temperature* T_b (for a radiance at a given frequency) and it is defined as the temperature of a black body that radiates the same surface brightness at a given frequency. This temperature can be either independent of, or highly dependent on the radiation's wavelength, depending on the nature of the source and any subsequent absorption.

2. Retrieval Methods

2.1 Introduction to the Inversion Problem

In atmospheric physics, to infer parameters of the atmosphere from remote sensing measurements a *retrieval code* is used. The code is usually made of two modules:

1. The *forward model* (FM), which is the module that simulates the observed atmospheric radiation, assuming to know its thermodynamic state and the concentration of different molecular species, by applying the theory of radiative transfer already described in the dedicated chapter.

2. The *retrieval model* (RM) (or *inverse model*), which is the module used in planetary atmosphere's studies to derive from radiance measurements the concentration of a particular molecule or the temperature profile.

In order to explain these two modules, let consider a physical system such a planetary atmosphere, whose parameters (temperature, pressure, volume mixing ratio (VMR), etc.) are represented by a state vector $\boldsymbol{x}$. Suppose then that the direct measurement of $\boldsymbol{x}$ is not possible. The only measures available are the radiance measurements $\boldsymbol{y}$ (column vector), which are related to the state vector by the formula

$$\boldsymbol{y} = \boldsymbol{f}(\boldsymbol{x}) + \boldsymbol{\epsilon} \tag{2.1}$$

where ϵ is the measurement error and the function $\boldsymbol{f}$, that associates the state of the atmosphere $\boldsymbol{x}$ to the measures $\boldsymbol{y}$, is the so called *forward model.* The process of determining $\boldsymbol{x}$ starting from the knowledge of $\mathbf{y}$ is called *inverse problem*. If the systematic error of the experimental apparatus can be considered negligible (which is real when the mean of ϵ is zero, $E[\epsilon] = 0$), the forward model has no bias, hence $E[\boldsymbol{f}(\boldsymbol{x})] = E[\boldsymbol{y}]$, and the measurement error is characterized by the variance-covariance matrix $\boldsymbol{S}_y$:

$$\boldsymbol{S}_y = E[\epsilon\epsilon^t] \tag{2.2}$$

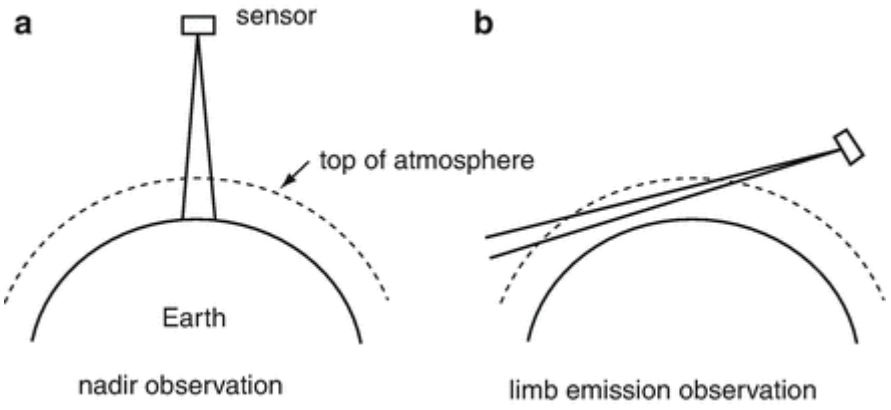

Fig 2.1 (a) Nadir observation geometry. **(b)** Limb observation geometry.

Satellite passive atmospheric measurements may be obtained using two different techniques: *nadir* and *limb sounding* (Fig 2.1):

- *Nadir-sounding* → The instrument looks perpendicularly to the tangent of the orbit at the satellite point. It is a one-dimensional (vertical) problem: the instrument Line Of Sight (LOS) encounters the planetary surface. This geometry is characterized by a high horizontal resolution, but a low vertical resolution (a single spectrum carries information on the full vertical distribution of the atmosphere).
- *Limb-sounding* → The instrument looks slightly off the tangent of the orbit at the satellite point, and the LOS never encounters the planetary surface. It is a two-dimensional problem. The altitude of the point of the line of sight closer to the surface is called *tangent altitude,* and the ray-paths crosses a significant horizontal distance through the atmosphere. Compared to the nadir-sounding, this technique improves the vertical resolution, whereas the horizontal resolution is worst.

When using spectral measurements, each spectral point is an element of the vector $\boldsymbol{y}$ and sometimes a set of spectra, acquired at slightly different positions in the atmosphere, is used to get as much information as possible. Consequently, the length of $\boldsymbol{y}$ vector is given by

$$n_y = n_{spet} \cdot n_{wl} \tag{2.3}$$

where, n_{spet} is the number of spectra in the set and n_{wl} is the number of spectral points in each spectrum.

Suppose now to have some a-priori information $\boldsymbol{x_a}$ on the state vector $\boldsymbol{x}$, where the variance-covariance matrix $\boldsymbol{S_a}$ represents the correspondent error. One approach that can be used to invert the measured spectra and obtain the target parameters is the Bayesian approach, which minimize the chi-square test function through an iterative procedure and allows to get the better estimate possible of the state of the system $\boldsymbol{x}$.

2.2 Bayes' Theorem and Inversion Problem solution

In statistics, *Bayes' Theorem* is a mathematical formula used to determine the conditional probability of events: it describes the probability of an event, based on prior knowledge of conditions that might be related to that event. The formal expression of the theorem is

$$P(A|B) = \frac{P(B|A)\,P(A)}{P(B)} \tag{2.4}$$

where $\mathrm{P}(\mathrm{A})$ and $\mathrm{P}(\mathrm{B})$ are the probabilities of the event A and B respectively, while $\mathrm{P}(\mathrm{A}|\mathrm{B})$ is the probability of the event A occurring, given event B has occurred and $\mathrm{P}(\mathrm{A}|\mathrm{B})$ is the probability of event B, given event A has occurred. Therefore, the inversion problem consists in determining the conditional probability of the state vector $\boldsymbol{x}$, given the measurement $\boldsymbol{y}$, by using the Bayes' theorem

$$P(\boldsymbol{x}|\boldsymbol{y}) = \frac{P(\boldsymbol{y}|\boldsymbol{x})\,P(\boldsymbol{x})}{P(\boldsymbol{y})} \tag{2.5}$$

where $\mathrm{P}(\boldsymbol{x})$ is the probability distribution of the state, $\mathrm{P}(\boldsymbol{y})$ that of the measurement and $P(\boldsymbol{y}|\boldsymbol{x})$ the other conditional probability, which can be defined as

$$P(\boldsymbol{y}|\boldsymbol{x}) = \frac{1}{(2\pi)^{n/2}|\boldsymbol{S}_a|} \cdot e^{-\frac{(\boldsymbol{y}-\boldsymbol{f}(\boldsymbol{x}))^t\, \boldsymbol{S}_y^{-1}\, (\boldsymbol{y}-\boldsymbol{f}(\boldsymbol{x}))}{2}} \tag{2.6}$$

Since it has been assumed to have an a-priori estimate of the state vector $\boldsymbol{x_a}$ and because $\boldsymbol{x_a}$ and $\boldsymbol{y}$ are completely independent, the conditional probability to get the two measures simultaneously is

$$P(\boldsymbol{y}|\boldsymbol{x_a}) = \frac{1}{(2\pi)^{n/2}|\boldsymbol{S}_a|} \cdot e^{-\frac{(\boldsymbol{x_a}-\boldsymbol{x})^t \boldsymbol{S}_a^{-1}(\boldsymbol{x_a}-\boldsymbol{x})}{2}} \cdot \frac{1}{(2\pi)^{m/2}|\boldsymbol{S}_y|} \cdot e^{-\frac{(\boldsymbol{y}-\boldsymbol{f}(\boldsymbol{x}))^t \boldsymbol{S}_y^{-1}(\boldsymbol{y}-\boldsymbol{f}(\boldsymbol{x}))}{2}} \tag{2.7}$$

where $\boldsymbol{x}$ is the real state of the system, that is unknown and has dimension n, while $\mathbf{f}(\mathrm{x})=\mathrm{E}[\mathbf{y}]$ is the expected value for measurements $\boldsymbol{y}$, which has dimension m. This equation can be also written

$$P(\boldsymbol{y}|\boldsymbol{x_a}) = \frac{1}{(2\pi)^{\frac{n+m}{2}}|\boldsymbol{S}_a||\boldsymbol{S}_y|} e^{-\frac{1}{2}[(\boldsymbol{x_a}-\boldsymbol{x})^t \boldsymbol{S}_a^{-1} (\boldsymbol{x_a}-\boldsymbol{x})+(\boldsymbol{y}-\boldsymbol{f}(\boldsymbol{x}))^t \boldsymbol{S}_y^{-1} (\boldsymbol{y}-\boldsymbol{f}(\boldsymbol{x}))]} \tag{2.8}$$

$P(\boldsymbol{y}|\boldsymbol{x_a})$ is a function of $\boldsymbol{x}$ and according to the principle of maximum likelihood, the better estimate of $\boldsymbol{x}$ is the one that maximizes $P(\boldsymbol{y}|\boldsymbol{x_a})$.

2.3 Maximum likelihood method

The maximum likelihood method is the procedure of estimating the values of one or more parameters for a given statistic by maximizing a likelihood function. According to this principle, once defined the conditional probability $P(\boldsymbol{y}|\boldsymbol{x_a})$, the value of $\boldsymbol{x}$ for which $P(\boldsymbol{y}|\boldsymbol{x_a})$ is maximum is the best estimate of the state vector and it is considered solution of the inverse problem. In order to maximize the conditional probability, the *likelihood function* χ^2 has to be minimized, where

$$\chi^2 = (\boldsymbol{x_a} - \boldsymbol{x})^t \boldsymbol{S}_a^{-1} (\boldsymbol{x_a} - \boldsymbol{x}) + (\boldsymbol{y} - \boldsymbol{f}(\boldsymbol{x}))^t \boldsymbol{S}_y^{-1} (\boldsymbol{y} - \boldsymbol{f}(\boldsymbol{x})) \tag{2.9}$$

which can be also written explicitly as

$$\chi^2 = \sum_{i,j=1}^{m} (\boldsymbol{y} - \boldsymbol{f}(\boldsymbol{x}))_i (\boldsymbol{S}_y^{-1})_{i,j} (\boldsymbol{y} - \boldsymbol{f}(\boldsymbol{x}))_j + \sum_{l,h=1}^{n} (\boldsymbol{x_a} - \boldsymbol{x})_l (\boldsymbol{S}_a^{-1})_{l,h} (\boldsymbol{x_a} - \boldsymbol{x})_h \tag{2.10}$$

The vector which minimizes this function can be derived by setting at zero the gradient of the likelihood function χ^2, i.e.

$$\boldsymbol{g}(\boldsymbol{x}) = \frac{\partial \chi^2}{\partial \boldsymbol{x}} = \nabla_x \chi^2 = -2\boldsymbol{K}^t \boldsymbol{S}_y^{-1} (\boldsymbol{y} - \boldsymbol{f}(\boldsymbol{x})) - 2\boldsymbol{S}_a^{-1} (\boldsymbol{x}_a - \boldsymbol{x}) = 0 \tag{2.11}$$

where $K_{i,j} \equiv \frac{\partial f_i}{\partial x_j}$ is the Jacobian matrix of the function $\boldsymbol{f}$ with respect to each of the parameters. Usually, this equation does not have an analytic solution, however an approximate numerical solution can be found by applying an iterative procedure, whose success depends on the degree of non-linearity of the function $\boldsymbol{f}$. A method commonly used to find numerical solutions of the equation $\nabla\chi^2 = 0$ is the *Gauss-Newton method*, which is discussed in the successive section.

2.4 Gauss-Newton method and Levenberg-Marquardt method

The *Gauss-Newton method* is used to solve non-linear least squares problem and consists in a modification of the *Newton's method* for finding the minimum of a function. Let consider the simple case of a one-dimensional scalar function $g(x)$. The zero of this function in an interval $x \in (a, b)$ can be found by applying the Newton's method; according to Fig 2.2, one can derive

$$x_i - x_{i+1} = g(x_{i-1})\, tan(\frac{\pi}{2} - \alpha) = \frac{g(x_{i-1})}{g'(x_{i-1})} \tag{2.12}$$

Therefore,

$$x_{i+1} = x_i - g'(x_{i-1})^{-1} \cdot\ g(x_{i-1}) \tag{2.13}$$

This is the Newton's iterative procedure, which allows to determine the zero point of $g(x)$ by calculating the tangent at x_i first and, successively, by following that tangent till it intersects the x axis in x_{i-1}.

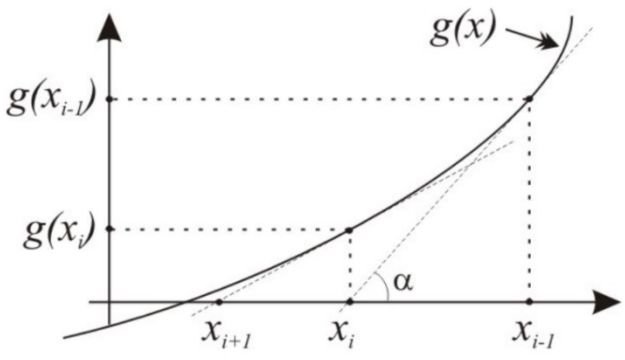

Fig 2.2 Derivation of Newton's method.

As it can be noticed, this method works for functions showing a certain degree of regularity and having only one zero in the interval $x \in (a, b)$. This expression can be also generalized to an n-dimensional case, where $\boldsymbol{g}(\boldsymbol{x})$: $\mathcal{R}^n \rightarrow \mathcal{R}^n$ is a vectorial function depending on $\boldsymbol{x}$. Then, the Newton's method can be rewritten as

$$\boldsymbol{x}_{i+1} = \boldsymbol{x}_i - [\nabla_x \boldsymbol{g}(\boldsymbol{x}_i)]^{-1} \cdot \boldsymbol{g}(\boldsymbol{x}_i) = \boldsymbol{x}_i - J^{-1} \cdot \boldsymbol{g}(\boldsymbol{x}_i) \tag{2.14}$$

where $\boldsymbol{J}$ is the Jacobian matrix of the function $\boldsymbol{g}$, which, assuming the $\boldsymbol{K}$, the Jacobian matrix of $\boldsymbol{f}$ (introduced in the equation 2.11), independent from $\boldsymbol{x}$ (*Gauss hypothesis*) is equal to

$$\boldsymbol{J} = \nabla_x \boldsymbol{g}(\boldsymbol{x}_i) = = 2\boldsymbol{K}^t \boldsymbol{S}_y^{-1} \boldsymbol{K} - 2[\nabla_x \boldsymbol{K}^t] \boldsymbol{S}_y^{-1} (\boldsymbol{y} - \boldsymbol{f}(\boldsymbol{x})) + 2\, \boldsymbol{S}_a^{-1} (\boldsymbol{x}_a - \boldsymbol{x}) \tag{2.15}$$

By substituting this expression in the previous one, the iterative solution results

$$\boldsymbol{x}_{i+1} = \boldsymbol{x}_i - \left(\boldsymbol{K_i}^t \boldsymbol{S}_y^{-1} \boldsymbol{K_i} + \boldsymbol{S}_a^{-1}\right) \cdot \left[\boldsymbol{K_i}^t \boldsymbol{S}_y^{-1} (\boldsymbol{y} - \boldsymbol{f}(\boldsymbol{x_i})) - \boldsymbol{S}_a^{-1} (\boldsymbol{x}_i - \boldsymbol{x}_a)\right] \tag{2.16}$$

where $\boldsymbol{K_i}$ is the Jacobian of the function $\boldsymbol{f}$ calculated at $\boldsymbol{x} = \boldsymbol{x}_i$. Therefore, to minimize the χ^2 of a certain inverse problem, this formula has to be iterated until a *convergence criterion* is satisfied and the procedure stops: e.g. when the variation of χ^2 in two consecutive iteration is lower than a certain threshold or the difference $\boldsymbol{x}_i - \boldsymbol{x}_{i-1}$ is less than a predetermined fraction of the error on $\boldsymbol{x}_i$. Finally, the error on the retrieved parameters due to noise in the measurement $\mathbf{y}$ and the a-priori estimate of the state vector $\boldsymbol{x}_a$ is expressed in the form of the variance-covariance matrix:

$$\boldsymbol{S}_x = \left(\boldsymbol{K}_{\boldsymbol{f-1}}^t \boldsymbol{S}_y^{-1} \boldsymbol{K}_{\boldsymbol{f-1}} + \boldsymbol{S}_a^{-1}\right) \tag{2.17}$$

In case of strongly non-linear problems, in which the step may be too large and, hence, project the state vector $\boldsymbol{x}_{i-1}$ out of the forward model linearity region, the Gauss-Newton method may fail to converge. Therefore, an optimization of this method is the Levenberg-Marquardt method (or *damped least squares method*), which consists in the reduction of the single steps to guarantee that the χ^2 function is still decreasing. This goal can be reached by adding a new term to equation 2.16:

$$\boldsymbol{x}_{i+1} = \boldsymbol{x}_i - \left(\boldsymbol{K_i}^t \boldsymbol{S}_y^{-1} \boldsymbol{K_i} + \boldsymbol{S}_a^{-1} + \lambda_{LM} D_i\right)^{-1} \cdot \left[\boldsymbol{K_i}^t \boldsymbol{S}_y^{-1} (\boldsymbol{y} - \boldsymbol{f}(\boldsymbol{x_i})) - \boldsymbol{S}_a^{-1} (\boldsymbol{x}_i - \boldsymbol{x}_a)\right] \tag{2.18}$$

where D_i is a diagonal matrix, which is usually taken equal to the diagonal elements of $\boldsymbol{K_i}^t \boldsymbol{S_y^{-1}} \boldsymbol{K_i}$, while λ_{LM} is a positive scalar parameter, called *dumping parameter*, which has to be tuned at each iteration so that the χ^2 decreases monotonically. Usually the retrieval is started from a λ_{LM} value and at each G-N iteration its value is decreased if the χ^2 decreases or increased if the χ^2 increases.

3. Jupiter

3.1 Missions to Jupiter

The first observations of Jupiter were made by Galileo Galilei in the 1610 using a telescope, but it was only with the opening to Space Exploration, thanks to the advent of spacecrafts, orbiters and probes, that a closer approach to the planet was made possible. Starting from the '70s several missions have been realized, making the knowledge about Jupiter grow fast.

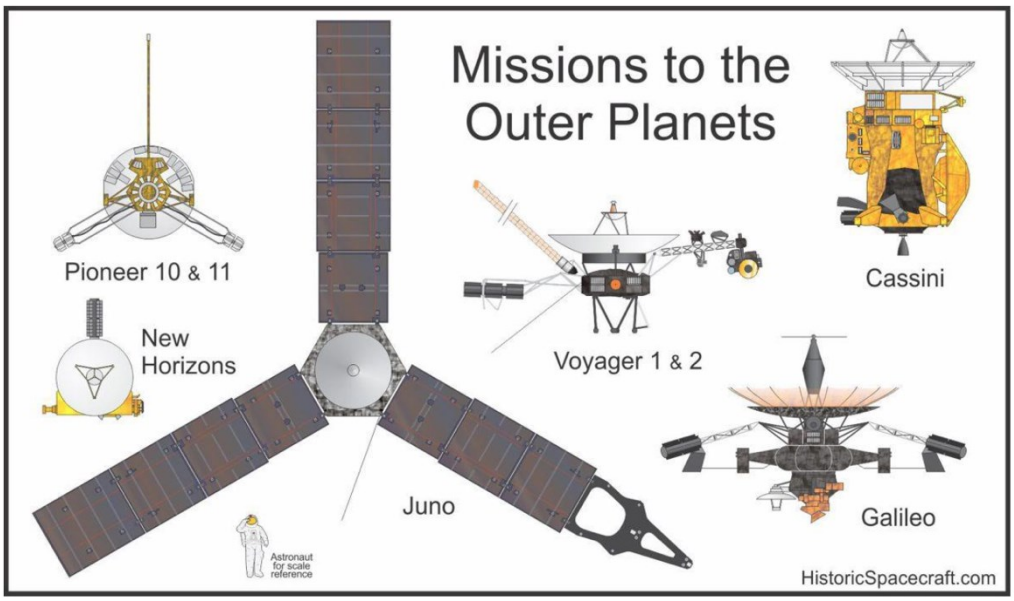

Fig 3.1 Mission to outer planets. [Max Camenzin, Jupiter im Visier, 2016]

[1972-73]: Pioneer 10 and Pioneer 11 (NASA)

The *Pioneer* 10 was launched on March 2, 1972 and it was the first spacecraft to travel through the asteroid belt and fly by Jupiter, when it made its closest encounter to the planet on December 3, 1973. This spacecraft not only obtained the first close-up images of the gas giant and its moons, but also made the first direct observations of Jupiter, measuring its magnetic field and radiation environment, and studying its atmosphere and interior. Following its twin probe, *Pioneer* 11 was launched on 5 April, 1973 and during its flyby of Jupiter, on December 2, 1974, obtained striking images of the Great Red Spot and observed for the first time the polar regions.

[1977]: Voyager 1 and Voyager 2 (NASA)

Voyager 1 and *Voyager* 2 are a pair of spacecrafts continuing on their journey since their launches in 1977. The twin spacecrafts were launched with the purpose to explore the planets of the outer solar system and the interplanetary environment, where each spacecraft had as main objectives to investigate the planets' atmosphere (dynamics, circulation, structure…) as well as to provide mass, size, shape and other geological information about the planets, their satellites and rings, and to determine the planetary magnetic field structures.

[1989]: **Galileo Orbiter and Galileo Probe** (NASA)

The *Galileo mission* consisted of two spacecrafts, an orbiter and an atmospheric probe with the purpose to investigate the Jovian atmosphere, the Galilean satellites and the Jovian magnetosphere. The *Galileo Orbiter* was launched on October 18, 1989 on space shuttle Atlantis and was the first spacecraft to be placed into orbit around the giant planet and to deploy an entry probe into an outer planet's atmosphere. The *Galileo Probe* was released from the orbiter on July 13, 1995, with an arrival on December 7, 1995. The probe measured the atmospheric elements, discovering that their relative abundances where different than on the Sun, indicating the evolution of Jupiter since it formed.

[1990]: Ulysses (NASA/ESA)

Ulysses (1990) was a joint venture of NASA and ESA, whose primary mission, formerly the *International Solar Polar Mission* (ISPM), was to investigate the properties of the solar wind and the interplanetary magnetic field as a function of solar latitude, as well as to study energetic particles composition and acceleration. Secondary objective of the mission included interplanetary and planetary physics investigation during the initial Earth-Jupiter phase and the study of the Jovian magnetosphere. As a matter of fact, to study the Sun at all latitudes the probe needed to change its orbital inclination, which requires a large change in heliocentric velocity; to achieve the desired orbit, in February 1992 the spacecraft used a Jupiter swingby to transfer to a heliocentric orbit with high heliocentric inclination. As a consequence, the probe made three fast latitude scans of the Sun in 1994/1995, 2000/2001, and 2007/2009.

[1997]: Cassini (NASA/ESA)

The *Cassini Orbiter*'s mission (1997) consists of delivering a probe to Titan, and then remaining in orbit around Saturn for further studies. Due to the propulsion systems available at that time, the Cassini could not be launched directly to Saturn, therefore it took a roundabout route to reach the

planet: the spacecraft made two flyby of Venus (April 1998 and June 1999), one of the Earth (August 1999), and one of Jupiter (December 2000). At Jupiter, numerous observations were made and some of the highest-resolution images ever taken of the planet were obtained.

[2006]: New Horizons (NASA)

The *New Horizons Probe* (2006), en route to Pluto, flew by Jupiter for a gravity assist, making its closes approach in February 2007. During this encounter *New Horizon*'s instrument made refined measurements of Jupiter's moons; moreover, several studies about Jupiter's Little Red Spot and magnetosphere were made.

[2011]: Juno (NASA)

The *Juno mission* was the second of three NASA missions chosen for the *New Frontiers program* and the first solar-powered mission to Jupiter. The spacecraft was launched on August 5, 2011, and after a 5 years cruise successfully entered the orbit of Jupiter on July 4, 2016. The purpose of the mission is to improve the knowledge about the solar system's beginnings, by revealing the origin and evolution of Jupiter which guards all the secrets to the processes and conditions behind the formation of our solar system and can provide important information for a better understanding of the other planetary systems being discovered. The spacecraft carries several science instruments, with the primary objectives to collect data to investigate

- **Origin**: understand the formation and origin of Jupiter's atmosphere and the potential migration of planets by measuring Jupiter's global abundance of oxygen (water) and nitrogen (ammonia), in order to determine which planet formation theory is correct or if a new one has to be postulated.
- **Atmosphere**: map the variation of composition, temperature, cloud opacity and atmospheric dynamics in the Jovian deep atmosphere, to depths greater than 100 bar at all latitudes.
- **Interior**: determine the deep structure of the planet, by mapping Jupiter's magnetic and gravity fields.
- **Magnetosphere**: study the Jupiter's magnetosphere near the planet's poles, especially the auroras, providing new information about how Jupiter's enormous magnetic force field affects its atmosphere.

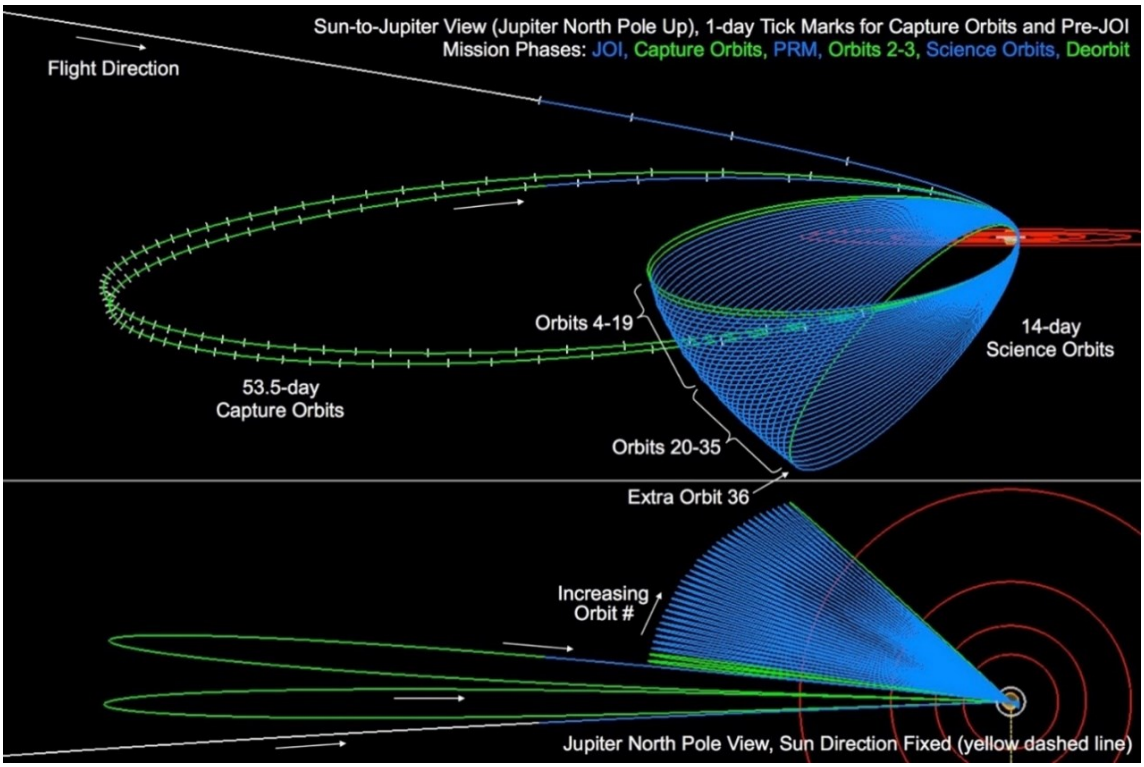

Fig 3.2 The original plan for NASA's Juno spacecraft. [NASA/ *JPL*]

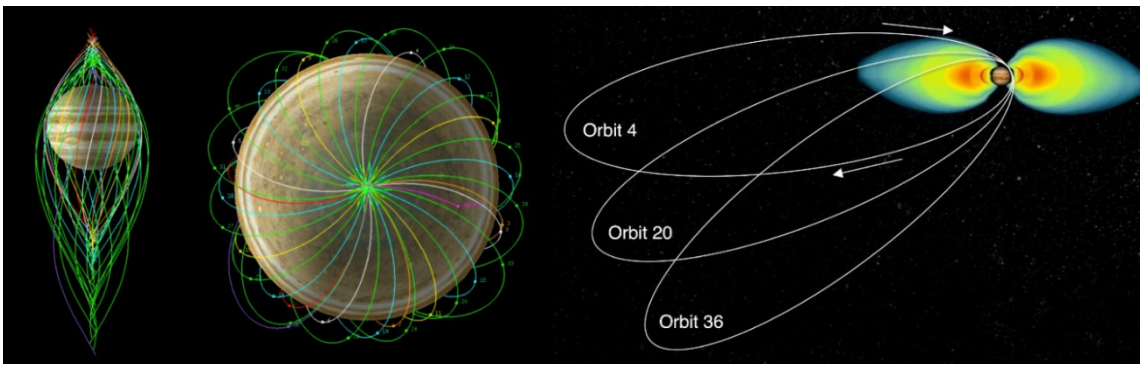

Fig 3.3 Juno's orbital grid. [NASA/JPL/Caltech]

Since its arrival at Jupiter, the Juno spacecraft has been providing completely new insights due to its unique polar orbit and the opportunity to observe for the first time the polar regions in detail. In facy, Juno traverses the planet in a north-south direction while avoiding exposure to the planet's harmful radiation, which are mostly concentrated in a belt that loops around its equator and potentially destructive for the *electronics*. With respect to the original plan, Juno's mission has been extended because of concerns about the spacecraft's main engine, which was originally designed to move the spacecraft from an initial orbit with a period of 53 days to a 14-day orbit, called for Juno to complete the 32 planned science orbits before the spacecraft was to be intentionally crashed in Jupiter's thick atmosphere in February 2018. That is why NASA decided to keep Juno in the 53-day orbit and approved an update to Juno's science operations until July 2021 to enable Juno to achieve all its

primary science objectives. Juno's closest approach to the planet varies from orbit to orbit, but stays within 3500-8000 km above the cloud tops: during each highly elliptical orbit, after an orbital period of about 53 days, the spacecraft spends few hours close to the planet and during these close flybys it collects the best possible data. In fact, the three hours before and after the closest approach are the most important for Juno's science instruments; while, for the rest of the orbit navigation steering and data transmission are the main tasks. Moreover, the low perijove altitude allows precise magnetic and gravitational measurements and observations from the six-channel microwave radiometer: the spacecraft rotates twice per minute about a spin axis almost normal to the orbital plane and the remote sensing instruments look outward in the spinning, giving the opportunity to all the instruments to look both toward Jupiter and toward the radiation belts, rings and deep space. In the future, the oblateness of the planet will cause geometrical changes of the orbit, causing the southward precession of the line of apsides, and the rotation of the orbital plane toward the nightside of Jupiter as the planet and spacecraft orbit the Sun; this will enable the study of the planet from different angles and the investigation of other magnetospheric regions.

The Fig 3.4 shows what has been discovered about Jupiter so far, even if it is not clear yet if the planet has a dense or diluted core and still much work has to be done.

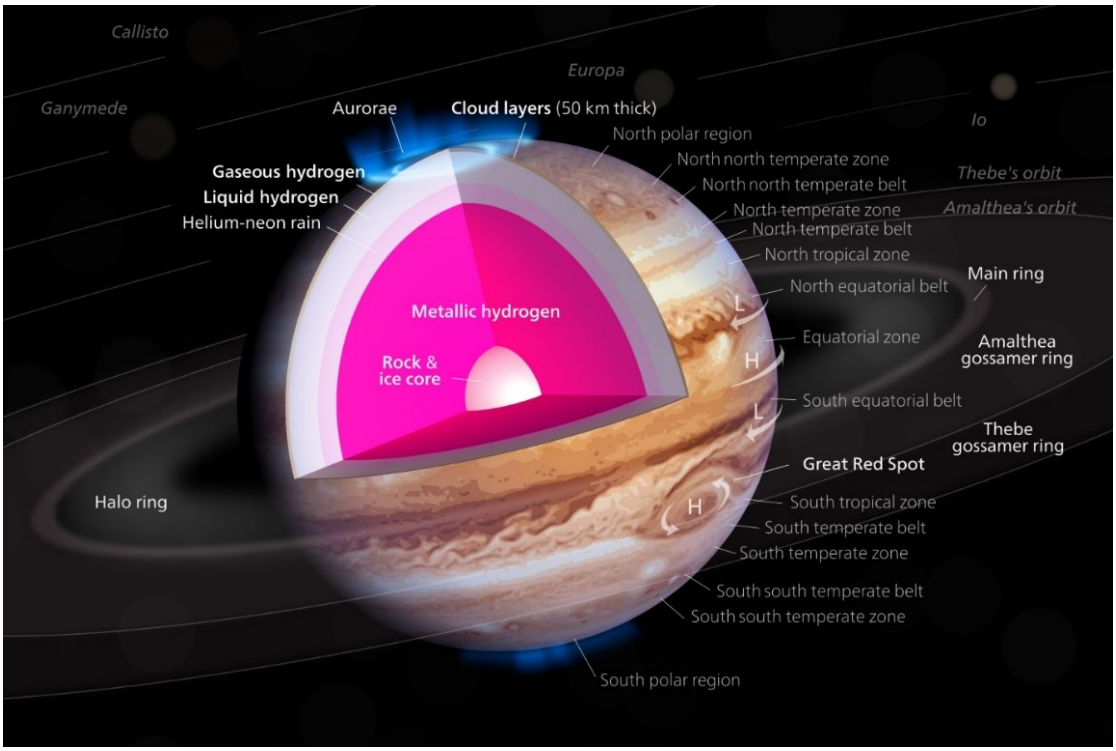

Fig 3.4 Jupiter's diagram: cross section of the interior, surface features, rings, and inner moons.

3.2 Introduction to Jupiter

Jupiter is one of the brighter object visible in the sky, therefore it has been known since ancient times. It is the fifth planet from the Sun (5.2 AU) and the largest in the Solar System (Fig 3.4): it is a gas giant, with a radius (69,911 km) almost 11 times the Earth' size and a mass more than twice that of all the other planets combined (317 times the mass of the Earth). Due to its rapid rotation the planet has assumed the shape of an oblate spheroid, with a probably rocky core of heavier elements, but a not well-defined solid surface. The outer atmosphere features a series of latitudinal bands and swirls due to ammonia and water clouds floating in an atmosphere, mainly composed of hydrogen and helium (Fig 3.4). Also, the planet possesses a powerful magnetosphere, and it is surrounded by 79 moons, including the four Galilean moons, and by a system of rings. The principal bulk and orbital parameters of Jupiter are reported in Tab 3.1 and Tab 3.2.

Jupiter's bulk parameters	
Mass	$1{,}898.19 \cdot 10^{24}\ kg$
Volume	$143{,}128 \cdot 10^{10}\ km^3$
Equatorial radius (1 bar level)	$71{,}492\ km$
Polar radius	$66{,}854\ km$
Volumetric mean radius	$69{,}911\ km$
Ellipticity	0.06487
Mean density	$1{,}326\ kg\, m^{-3}$
Gravity (eq., 1 bar)	$24.79\ m\, s^{-2}$
Acceleration (eq., 1 bar)	$23.12\ m\, s^{-2}$
Escape velocity	$59.5\ km\, s^{-1}$
GM	$126.687 \cdot 10^{6}\ km^3 s^{-2}$
Bond albedo	0.343
Geometric albedo	0.538
Solar irradiance	$50.26\ W\, m^{-2}$
Black-body temperature	109.9
Moment of inertia	0.254
J_2	$14{,}736 \cdot 10^{6}$
Number of natural satellites	79
Planetary ring system	Yes

Tab 3.1 Jupiter's bulk parameters. [https://nssdc.gsfc.nasa.gov]

Jupiter's orbital parameters	
Semimajor axis	$778.57 \cdot 10^6\ km$
Sideral orbit period	4,332.589 *days*
Tropical orbit period	4,330.595 *days*
Perihelion	$740.52 \cdot 10^6\ km$
Aphelion	$816.62 \cdot 10^6\ km$
Synodic period	398.88 *days*
Mean orbit velocity	$13..06\ \ km\ s^{-1}$
Max. orbital velocity	$13.72\ \ km\ s^{-1}$
Min. orbital velocity	$12.44\ \ km\ s^{-1}$
Orbit inclination	1.304 *deg*
Orbit eccentricity	0.0489
Sideral rotation period	9.9250* *hrs*
Length of the day	9.9259 *hrs*
Obliquity to orbit	3.13 *deg*
Inclination of equator	3.13 *deg*

Tab 3.2 Jupiter's orbital parameters (* System III (1965.0) coordinates). [https://nssdc.gsfc.nasa.gov]

3.2.1 Jupiter's formation and migration

The Solar System formed about 4.6 billion years ago from a gravitational collapse of a region, called pre-solar nebula, within a large molecular cloud composed by dust and gases. After the collapse, the nebula started to spin faster for the conservation of the angular momentum, and most of the mass migrated toward its center. This contraction caused the nebula to flatten into a protoplanetary disk with a protostar at the center and a diameter of 200 AU, from which the planets formed. Jupiter captured most of the mass left over by the formation of the Sun, ending up with a composition similar to that of the star. However, the mechanisms that brought to Jupiter's formation are still unsure. Since the '70s two hypothesis have been discussed:

1. ***The core accretion theory*** → This hypothesis explains the giant gas formation as the consequence of the formation of planetary embryos composed of rock- and ice-forming elements that act as gravitational seeds for nebula gas capture/condensation. However, it cannot explain massive planets' formation far from the Sun: according to this mechanism, the time-scale requested for the formation of Neptune and Uranus is estimated around 10 million

years, while the dust and gas in the protoplanetary disk probably only lasted few millions of years.

2. ***The gravitational disk instability*** → This theory asserts that the outer planets were formed in a similar way the Sun was formed, i.e. by the sudden gravitational collapse of a large part of the protoplanetary nebula, leading from a smooth and regular disk to a collection of self-gravitating clumps orbiting around the Sun which, eventually, evolved into planets.

Moreover, according to the *gran tack hypothesis* Jupiter underwent a two-phase migration after its formation, migrating inward to 1.5 AU and then outward to its current orbit, at 5.2 AU.

- **Type II migration** → Jupiter formed about 3.5 AU, near the ice line[2]. Then it was captured by flow of gas still swirling around the Sun and slowly spiralled inward with the gas disk and settled at a distance of 1.5 AU (about Mars position nowadays).
- **Type I migration** → Shortly after its formation, Saturn overwent the same mechanism of inward migration. The planet started to migrate toward the Sun and when arrived close to Jupiter the gas in between the two planets was expelled, causing the halt of the inward spiral and reversing the direction of their travel, until Jupiter found its rest at 5.2 AU and Saturn at 7 AU.

According to the gran tack model, Jupiter's journey strongly influenced the Solar System. Astronomers believe that Jupiter's gravity field strongly perturbed the objects encountered during it slow migration process, taking to the formation of loose collection of objects unable to form other planets, the so-called asteroid belt, and limiting the accretion of Mars.

3.2.1 Jupiter's orbit and rotation

Jupiter is the only planet of the Solar System having its barycentre with the Sun located outside the volume of the Sun. With an average distance of 778 million km (about 5.2 AU) from the star, the planet completes an orbit every 11.86 years. Jupiter's orbit is elliptical, with an eccentricity value of

[2] The *frost line* (or *ice line*) is the distance from the protostar in the solar nebula where the temperature are low enough for volatile compound such as water, ammonia, methane, carbon dioxide, and carbon monoxide to condense into solid ice grains.

0.048 which determines the variation of the gas giant's distance from the Sun by 75 million km between its nearest approach (perihelion) and furthest one (aphelion). Moreover, its equator is tilted with respect to its orbital path by only 3°; as a consequence, Jupiter spins almost upright and do not experience extreme seasonal changes as other planets. Due to its high-speed rotation, which is the fastest of all the planets in the Solar System, Jupiter completes one rotation on its axis every 9.9 hours. The rapid rotation causes the planet's equator to bulge out: while the equatorial radius is of about 71,500 km, the polar radius is 66,800 km. Therefore, instead of being a perfect sphere, Jupiter shows an oblate shape. However, because Jupiter is not a solid body its upper atmosphere experiences differential rotation. In fact, the rotation takes different amount of time depending on the position on the planet: the rotation at the poles is about 5 minutes longer than at the equator.

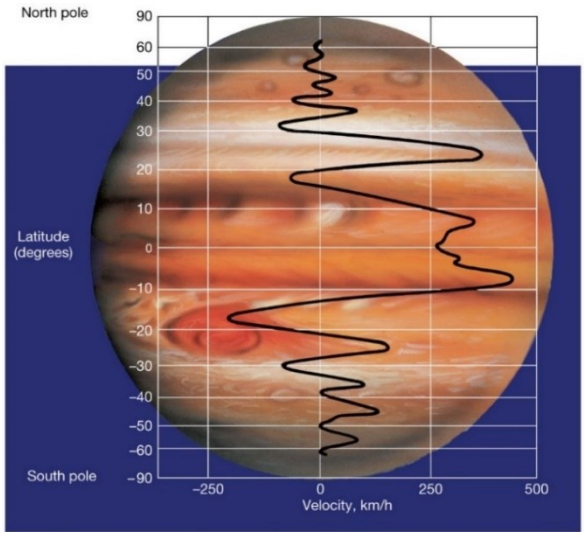

Fig 3.5 Jupiter's asymmetric zonal velocity field. [Pearson Education, 2011]

The interval of time of 9.9 hrs necessary to Jupiter to complete a rotation about its axis is an average for the entire planet. Usually, scientists use three different system to calculate Jupiter's rotation (Fig 3.5):

1. *System I* → For latitudes within 10° S and 10° N the rotation is **9hrs 50min 30.0s.**
2. *System II* → For latitudes > 10° S and 10° N the rotation is **9hrs 55min 40.6s.**
3. System III → This system measures the rotation speed of Jupiter's magnetosphere, **9hrs 55min 29.71 s**, which is usually considered the official one.

where the first two rotation rates are determined by measuring how long it takes to a specific storm to come back into view and the third system is usually considered the official one (Fig 3.5).

3.3 Jupiter's atmosphere

3.3.1 Composition of Jupiter's atmosphere

The study of the composition of Jupiter's atmosphere started in the 19th century when Rutherford (1862) observed the near infrared spectrum of the planet. Its interpretation remained uncertain until Wild in the 1932 showed that the spectral lines could be associate to methane and ammonia. The presence of these hydrogen-rich compounds, together with the low density of the planet, lead the scientific community to infer that Jupiter has a similar composition to that of the Sun. In support of this theory, the large mass of Jupiter and low temperature of the protosolar nebula's region in which the planed formed suggested that Jupiter had retain a large amount of even the lightest element, primarily hydrogen. With the Voyager missions it started to become clear that Jupiter and the Sun do not have the same abundances of elements. Great advances arrived with the Galileo mission, in which the orbiter started systematic observations of the Jovian atmosphere and of the surface of the Galilean moons, while the probe descending through the atmosphere made the first direct measurements of the composition. The Galileo probe carried two instrument: a quadrupole mass spectrometer and a helium abundance detector, which allowed to determine the global mean value for the volume mixing ratio of the most abundant species in the atmosphere of Jupiter, as reported in Tab 3.3 [Steinruek (2017)]. The composition of Jupiter's atmosphere results similar to that of the planet as a whole, whose main constituents are *hydrogen* (90%) and *helium* (9%). The most abundant minor species is *methane* and it is expected to be well-mixed throughout the atmosphere: CH_4 cannot condensate at any point in the atmosphere because of the not cold enough Jovian temperatures; therefore, methane is chemically stable at pressure above 1mbar, while at lower pressure is subjected to photochemical dissociation. Instead ammonia and water can condensate within the troposphere, and ammonia can combine with hydrogen sulfide (H_2S) to produce *ammonium hydrosulfide* $((NH_4)SH)$. Moreover, in the upper atmosphere small amounts of hydrocarbons such as *ethane*, *acetylene*, and *diacetylene* can be found, which are generated through the interaction of methane molecules with the solar UV radiation and the charged particles coming from the magnetosphere. Also, in the upper atmosphere *carbon monoxide*, *carbon dioxide* and *water* are present, probably generated from comets impact, as e.g. Shoemaker-Levy 9. In fact, water cannot come from the troposphere, because the cold tropopause prevents it to ascend to the stratosphere.

Species	Volume Mixing Ratio
Hydrogen, H_2	0.86
Helium, He	0.136
Methane, CH_4	0.0018
Ammonia, NH_3	0.0007
Water, H_2O	>0.0005

Tab 3.3 Values of the global mean values for the volume mixing ratios of the most abundant gases in the Jovian atmosphere as reported by Taylor et al. (2004)

3.3.2 Jupiter's temperatures and vertical structure

Jupiter's atmosphere can be separated in four layers (Fig 3.6): troposphere, stratosphere, thermosphere, and exosphere. Differently from Earth, Jupiter does not have the mesosphere.

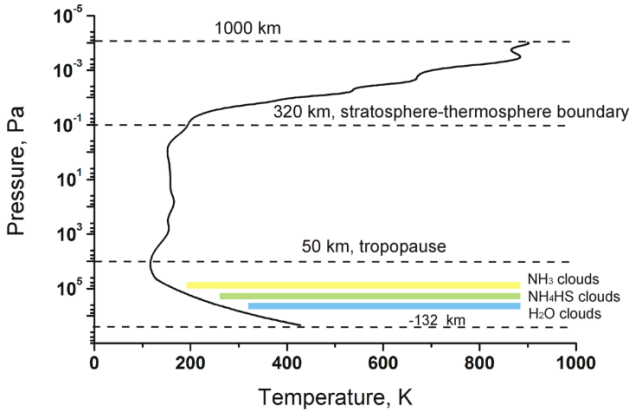

Fig 3.6 Vertical temperature profile of Jupiter. [Seiff et al., 1998]

1. *Troposphere* → Because of the temperatures and pressures well above those of hydrogen and helium critical points Jupiter lacks a real solid surface. Therefore, there is not a defined boundary between gas and liquid phases and the *troposphere*, which is the lowest atmospheric layer, smoothly transitions in the fluid interior of the planet. For this reason, the pressure level of 10 bars (90 km below 1 bar and a temperature around 340 K) is considered as the base of the troposphere, while the 1 bar pressure level as the surface of Jupiter, hence the zero point for altitude. In the troposphere the temperature decreases ascending in altitude and reaches its minimum value around 0.1 bar (50 km) and 110 K, where the tropopause separates the troposphere from the stratosphere. Moreover, this layer is characterized by a complicated clouds structure, where the upper clouds (0.6-0.9 bar) are made of *ammonia ice* (NH_3), have a yellow color and are at about 150 K; the middle clouds (1–2 bar) are denser and consist of *ammonium hydrosulfide* ($(NH_4)SH$)

or *ammonium sulfide* $\left[(NH_4)_2S\right)$ have an orange color and are at about 200 K; the lower clouds $(3 - 7$ bar$)$ are *water* clouds (H_2O), which form the densest clouds layer and strongly influence the atmospheric dynamics of the planet, because of the higher condensation heat and higher abundance of water; while methane clouds cannot exist because the temperatures are too high for it to condensate. Above these main cloud decks, various processes such as photochemistry can occur and create hydrocarbon *haze* particles forming various tropospheric $(200\text{-}500$ mbar$)$ haze layers; in fact, even if ammonia can be found in condensed phase in the troposphere, its vapour pressure at the cloud tops is sufficient for NH_3 photochemistry to be important.

2. *Stratosphere* → In the stratosphere the temperature rises to a value of 200 K at the stratopause, where at 1 μbar $(320$ km$)$ pressure level the transition to the thermosphere occurs. Here, methane is the most abundant equilibrium constituent, with an abundance ratio relative to molecular hydrogen of 10^{-4}, while for other light hydrocarbons it is around 10^{-6}. Therefore, methane photolysis dominates the stratospheric photochemistry: the near-infrared methane bands have a similar role to that of the ozone on Earth and the condensation of photochemical products created through methane decomposition by solar UV radiation generates stratospheric hazes, that can scatter incident radiation out of the atmosphere or absorb photons.

3. *Thermosphere* → In the thermosphere the temperature increasing with the altitude can reach a value of 1000 K at around 1 nbar pressure level $(1000$ km$)$. Here lie layers of increased electron and ion density that form the ionosphere, and phenomena such as X-ray emissions and polar aurorae find an explanation. Differently from what expected by the models, the temperatures in the thermosphere are much higher than 400 K, ranging around 800-1000 K; however, the reason for these hot temperatures is not clear yet: they may result of high-energy solar radiation $(UV$ or X-ray$)$ absorption, by the heating due to the precipitation of charged particles from Jupiter's magnetosphere which create bright auroral ovals, or by dissipation of upward-propagating gravity wave. Thermosphere and exosphere emit X-rays, observed for the first time in 1983, by the Einstein observatory. Moreover, Jupiter's thermosphere was the first place outside Earth where the trihydrogen cation H_3^+, which emits at wavelengths 3-5 μm and acts as the main cooling mechanism of the thermosphere, was found.

All the four giant planets have a rather uniform emission power, with latitudinal variations from the poles to the equator of only few kelvins. However, Jupiter's shows hot spots $(1\%$ of the planetary

surface) which give a major contribute to the emitted flux at 5 μm, due to their absence of water vapour and the brightness temperature of 260 K.

3.4 Jupiter's magnetospheres

3.4.1 Planetary magnetospheres

The term magnetosphere was coined by Gold (1959) to indicate the region above the ionosphere in which the magnetic field has dominant control over the motions of gas and fast charged particles; therefore, it is referred to a region of space influenced by the magnetic field of a planet. Thanks to the spacecraft era, important discoveries about the high degree to which the planetary magnetic fields organize ionized matter, as well as the large-scale plasma formations within the planets' magnetospheres, have been realized. Spacecrafts carrying magnetometers have been able to reach and characterize the magnetic fields of all the planets of the Solar System, showing strong magnetic fields for the four gas giants and weaker ones for the terrestrial planets. Moreover, the detection of long-distance propagating radio waves, X-rays, and gamma rays generated by the mechanisms operating within the plasmas have led to a series of new astrophysical problems. In particular, the nature of the interaction between the planetary object and the surrounding plasma depends on the properties of both the object and the plasma flow in which is embedded [Bagenal (2007)]. In fact, though planetary magnetospheres share general features as

- convective and coronational plasma flows,
- the radio waves emission by planetary plasmas,
- plasma tori of different origins,
- the capacity of accelerating ions and electrons from thermal energies to tens and hundreds of megavolt (MV),
- various basic plasmatic processes and instabilities: reconnection of magnetic field lines, Kelvin-Helmholtz instability, wave-particles interactions, etc.

what does really distinguish the planetary magnetospheres is wether are driven primarily by the solar wind or by the planet's rotation. As a matter of fact, the interaction between the *solar wind*, which is the expansion of the solar corona embedding all the solar system objects, with the planetary intrinsic

magnetic field and plasma generates a magnetosphere with an overall size depending on the dynamic pressure of the solar wind plasma and the strength of the magnetic field of the planet. More in detail, the speed of the solar wind is greater than that of the fastest wave mode propagating in the interplanetary plasma; in fact, the solar wind's velocity of about 400 $\mathrm{km\ s^{-1}}$ is called "super-Alfvénic", i.e. exceeds the characteristic signal velocity (Alfvén velocity[3]) in a completely ionized gas. Consequently, the interaction of the supersonic solar wind with the planetary magnetic field produces a *bow shock* upstream of the planet. Behind this shock front, in a region called *magnetosheath* lying between the bow shock and the *magnetopause,* the solar wind is decelerated and deflected around the magnetospheric obstacle. The location of the magnetopause depends on the balance between the dynamic pressure of the solar wind and the pressure of the dynamic planetary magnetic field: the magnetopause moves inward and outward with the solar wind pressure's increases and decreases, respectively. Moreover, regardless of the interaction details, in nearly all cases the magnetosphere shows the *magnetotail*: a narrow and elongated region that can extend in the direction away from the Sun, downstream the solar wind (Fig 3.7). However, for the case of Jupiter, as explained in the next section, plasmas within the magnetosphere play an important role in determining the overall size of its magnetosphere.

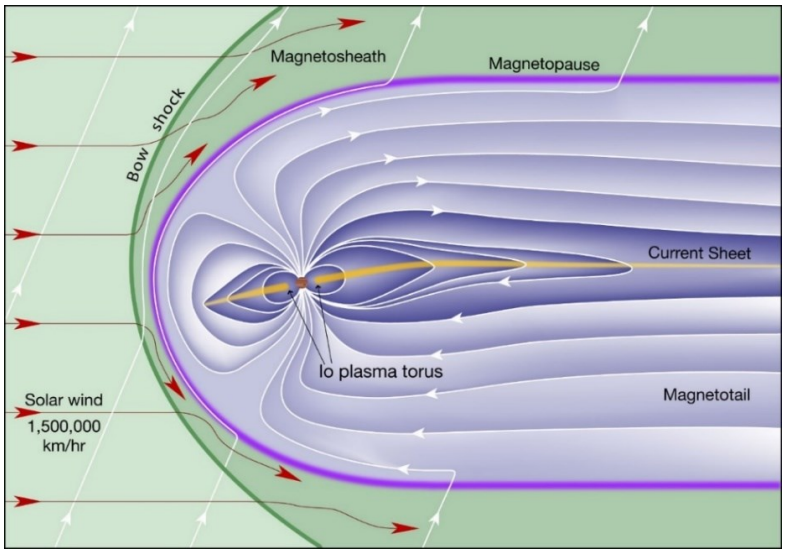

Fig 3.7 Graphic representation of Jupiter's magnetosphere. [from the New Solar System, (eds. Kelly Beatty et al.), CUP/Sky Publisher]

[3]Alfvén velocity is given by $\frac{B}{\sqrt{4\pi\rho}}$, where B is the strength of the magnetic field and ρ is the ion density in the magnetic field.

3.4.2 Planetary plasmas: sources and dynamics

A magnetospheric plasma is a gas composed by a mixture of positively and negatively charged particles that looks electrically neutral to the outside, which can have different sources:

1. the *solar wind plasma* may be convected from the solar corona to the planetary environment passing through the magnetopause. It is mainly composed of atomic hydrogen H^+ with a few percent He^+;
2. the *ionospheric plasma* may have flowed out of the planet's ionosphere, escaping the gravity of the planet. This plasma is generated in the upper atmosphere by ionizing agents as solar photons or energetic particles impact, acting on the atmospheric gas;
3. in giant planet systems, *orbital plasma* sources do also exist. They may be the result of the ionization of neutral material coming from the satellites or rings embedded in the magnetosphere.

To understand which of these sources have generated the plasma, its chemical composition has to be investigated. For example, in the case of Jupiter the presence of sulfur and oxygen ions is a clear indicator of the origin in Io's volcanic gases of the Jovian plasma: Io loses about $1\ \mathrm{t\,s^{-1}}$ of atmospheric material, in particular SO_2, that once ionized to sulfur and oxygen ions is captured by Jupiter's magnetic field; instead, O^+ ions in Earth's magnetosphere come from the ionosphere. However, understanding the source of protons is not a simple task, because it could be either ionospheric or from the solar wind. One method to determine the origins of the plasma (whose efficiency is limited by the magnitude of the energies at stake, resulting more reliable at higher energies) is to consider the abundance of helium ions: helium in the solar wind arriving from the Sun's hot corona is fully ionized as He^{++} ions, whereas ionospheric helium ions are usually singly ionized, He^+, being the ionospheric plasma much cooler; therefore, the abundance ratios He^{++}/H^+ and He^+/H^+ can be indicative of the relative importance of these sources. Also, the temperature of a plasma can be of help for understanding its origin, because the ions generated by the ionization of neutral gases have energies associated with the local plasma flow speed; hence ionospheric plasma has usually a temperature $< 0.1\ \mathrm{eV}$, while the material that has leaked in from the solar wind has energies of a few keV.

In general, a plasma is composed by an equal number of positive and negative elementary charges and to the outside it appears electrically neutral; however, in presence of electric and magnetic fields a plasma behaves quite differently from a neutral gas, developing and carrying electric currents which generate additional magnetic fields. The simplest way to describe the dynamics of a plasma consists in using the single-particle-motion or guiding-centre description, which determines the motion of a particle under the influence of external electric and magnetic fields, by treating it as the superposition of a relatively fast circular motion around a point (*guiding center*) and a relatively slow drift of this point. Considering a particle of charge q and mass m, moving with a velocity v in an electric field E and magnetic field B, this is subjected to the *Lorentz force* which causes the particle to accelerate

$$F = q\,(E + v \times B) = m\frac{dv}{dt} \tag{3.1}$$

For the case of a dipole magnetic field, from the resolution of this equation three types of typical motions of charged particles on different spatial and temporal scales result: gyration, bounce, and drift, associated with three motion parameters (*adiabatic parameters*) (Fig 3.8a). In particular, the magnetic moment M is associated with the gyration about the magnetic field lines, the longitudinal invariant J is associated with the bounce motion along the field lines, and the drift invariant Φ is associated with the drift motion around the planet. On the shortest time scale and in static and uniform magnetic field, this equation describes the motion of a particle around the magnetic field on a circular orbit, whose center is called the *guiding center*, with a sense of rotation depending on the sign of the charge (Fig 3.8).

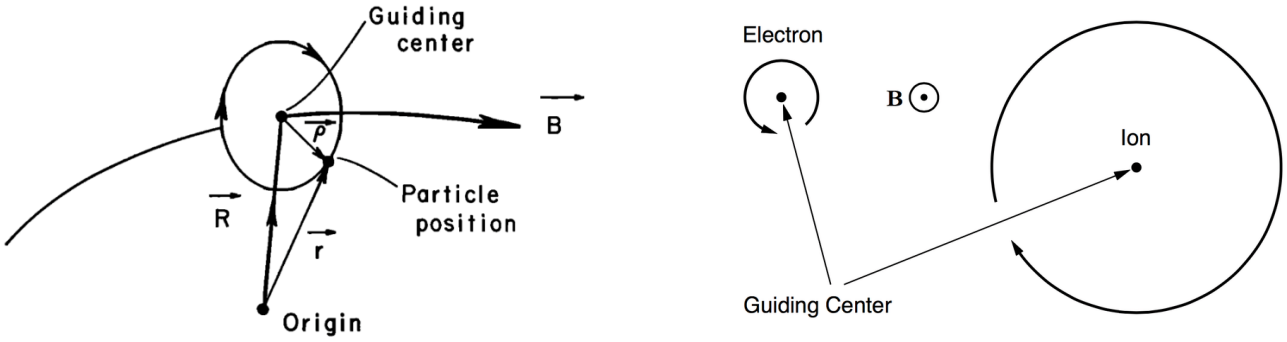

Fig 3.8 (*left*) Gyro motion of the charged particle around its guiding centre. (*right*) Motion of electrons and ions in a uniform magnetic field.

Moving along the magnetic field with a possible constant velocity parallel to the field, the particle describes an helictical trajectory (Fig 3.8, *left*). If the **E** or **B** field is non-static and/or non-homogeneous, drifts occur because the curvature of the particle gyration becomes alternately larger and smaller. As a matter of fact, as it approaches the poles of the planet, the particle experiences a stronger magnetic field which causes the increase of the gyromotion and the decrease of the particle motion along the field. The particle is then trapped and bounces between the polar regions (Fig 3.9a, *center*). On larger time scales ions and electrons experience drifts about the planet forming a belt of trapped particles (Fig 3.9a, *right*), as shown Fig 3.9b for the Earth's radiation belts. Instead, the processes of particles gain/loss act on much longer time scale, consisting in hours/years for the Earth, and months/years at Jupiter. Radial motions can occur due to scattering by small scale perturbations in the **B** field, and eventually the particles escape the magnetosphere through charge exchange with neutral particles, that produces fast neutral able to escape the system, or by hitting the atmosphere of moons or of the planet.

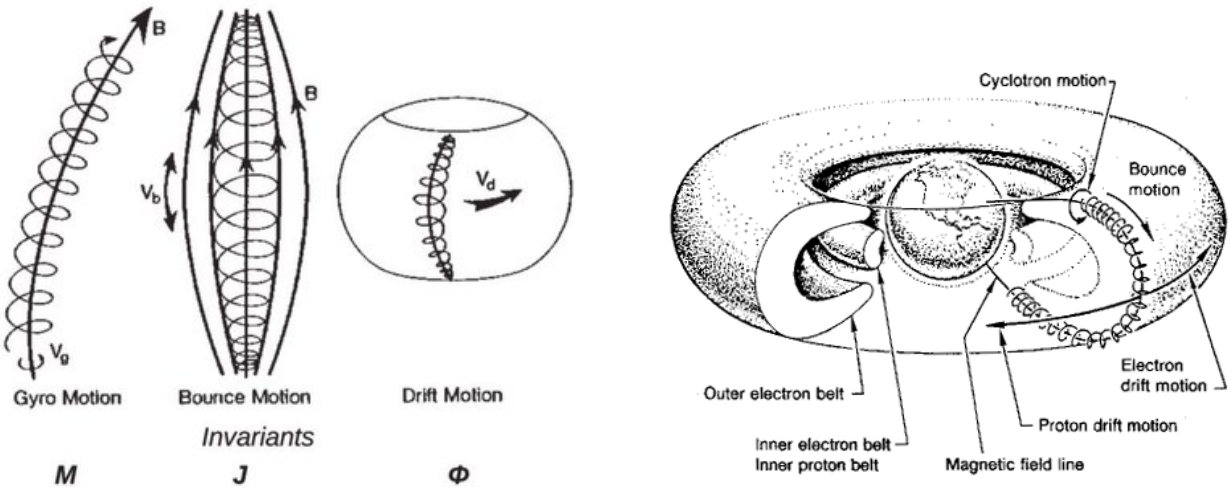

Fig 3.9 (a) Particle exhibit gyromotion around magnetic field lines (*left*), bounce motion along field lines between reflection points (*center*), and drift motion around the planet (*right*). **(b)** Schematic representation of the inner and outer radiation belts around the Earth.

Moving farther away from the planet, the intensity of the magnetic field decreases and can be modified from a simple dipole under the influence of electric currents flowing through the plasma. The magnetospheric configuration depends on the processes controlling the magnetospheric flows: the two largest sources of momentum in the planetary magnetospheres are the rotation of the planet and

the solar wind; therefore, the plasma flows can be predominantly in rotation with the planet or controlled by the interaction of the solar wind with the magnetosphere. The corotation with the planet is the simplest pattern of plasma flow in a planetary magnetosphere and one that plays a major role particularly in the magnetosphere of giant planets. However, if the planet possesses an insulating atmosphere, the rotation of the planet itself has no direct effect on the plasma flow in the magnetosphere: what does affect the plasma is the motion of the neutral upper atmosphere (the thermosphere) at altitudes of the ionosphere, where the neutral and the ionized components coexist and interact [Vogt (2012)].

3.4.3 Structure of Jupiter's magnetosphere

Due to its strong magnetic field, Jupiter is characterized by the largest and most powerful of any planetary magnetosphere, with a length scale 100 times that of the Earth: it extends from 50 to 100 R_J (Jovian radii) sunward and at least 6 AU anti-sunward. Jupiter is also the fastest rotating planet of the solar system: the Jovian magnetosphere shows a periodicity in the plasma density which is related to the 10 hrs period rotation spin, meaning that, different from the terrestrial magnetosphere where the dynamic behaviour is mainly controlled by the interaction between the planetary magnetic field and interplanetary medium, Jupiter's magnetosphere is dominated by the rotation. Ultimately, Jupiter has the most massive satellites system of any planets: the Galilean satellites Io, Europa, Ganymede and Callisto, whose orbits lie within Jupiter's magnetosphere, provide most of the plasma. Therefore, Jupiter's internal plasma source from the moon Io and the centrifugal forces resulting from its rapid rotation determine the main properties and processes throughout the entire Jovian magnetosphere, which can be divided into three regions:

1. *Inner magnetosphere* [$< 20\ R_J$] → The inner magnetosphere of Jupiter has a magnetic field largely dipolar and the bulk plasma flows in the corotational direction (azimuthal) with a speed at or near corotation. One of the main features of this portion of magnetosphere is the *Io plasma torus*, which is a ring of dense plasma generated by the incessant volcanism of this moon. Io supplies gasses (mainly SO_2) at a rate of about one ton per second, which are then ionized in sulfur and oxygen and become trapped in Jupiter's magnetic field. The consequent coupling to Jupiter causes the magnetospheric plasma to corotate with the planet and to be confined toward the equator due

to strong centrifugal forces. As a result, the densest plasma forms a torus around Jupiter, at the orbit of Io, extending from $\sim 5\ R_J$ to $\sim 10\ R_J$. A large portion of this material is quickly ejected trough charge exchange, while the rest stays in the torus for a period of 25-80 days, gradually expanding in the middle magnetosphere [Bagenal (2013)]. Moreover, high energy belts can be found inside of $5\ R_J$, resulting from the inward radial diffusion of plasma (due to dynamo fields generated by ionospheric winds) [Bolton et al. (2017)].

2. *Middle magnetosphere* $[20 - 60\ R_J] \rightarrow$ In the middle magnetosphere the plasma in the Io torus diffuses outward because of the centrifugal force resulting from the rotation of the planet, which produces a multispecies plasma sheet (current sheet, magnetodisk) extending from Io orbits ($\sim 5.9\ R_J$) to the boundary of the magnetosphere, where around 60 R_J the corotation of the plasma sheet breaks down: this cold plasma (10 eV) loads up the magnetic field lines beyond Io, where the conductivity of Jupiter's ionosphere cannot force this region of the magnetosphere to corotate rigidly with the planet. This current sheet is parallel to the magnetic equator (tilted of 10° with respect to the geographic equator) in between 10 R_J and 30 R_J, and parallel to the solar wind at > 60 R_J; while from 30 R_J to 60 R_J the current sheet is between the centrifugal and magnetic equators. In this region the dipolar form of the magnetic field is maintained, except in the neighbourhood of the equatorial plane, where the radial components of the current sheets stretch the field's lines outwards. According to the simplest current system proposed by Hill (1979) and the observations of Voyager spacecraft, as the ionogenic plasma moves radially outward from the Io torus, its angular velocity, which is close to rigid corotation with the planet in the source region, tends to decrease for the conservation of the angular momentum: in absence of torque, the azimuthal speed of the plasma falls with a radial distance as ρ^{-1}, while the angular velocity as ρ^{-2} [Cowley and Bunce (2001)]. As a consequence, the difference between the flux tube angular velocity and the planetary angular velocity results in a differential velocity between the neutral particles in the upper atmosphere corotating with the planet and the ionospheric charged particles which rotate with the flux tube; therefore, the collisions between these particles occurring in the ionosphere, in the Pedersen-conducing layer, cause the flux tube to overgo a frictional torque spinning them back up to corotation, while, simultaneously, an equal and opposite torque acts on the neutral reducing the angular velocity of the upper atmosphere. Hill's model

shows that depending on Pedersen conductivity and the outflow rate of the ionogenic plasma, the ionospheric torque can maintain a near-rigid corotation only within few tens of R_J, becoming ineffective at larger distance where the angular velocity decreases as ρ^{-2}. Consequently, the field lines in the equatorial magnetosphere are swept back azimuthally into a spiral shape, because of the frozen-in-flux condition of the magnetic field which is fixed to the outflowing plasma, and the flux tube lags corotation. In Fig 3.10 the current system is shown, that develops fuelled by a field-aligned current (*Birkeland current*) exiting the ionosphere, an outward radial corotation enforcement current in the equator, a returning field-aligned current into the ionosphere and that closes within the meridional Pedersen currents in the ionosphere. In particular, the *Pedersen current* is associate to the force $\mathbf{J} \times \mathbf{B}$ of the ions on the neutral, which is directed opposite to the planetary rotation and tends to de-spin the atmosphere.

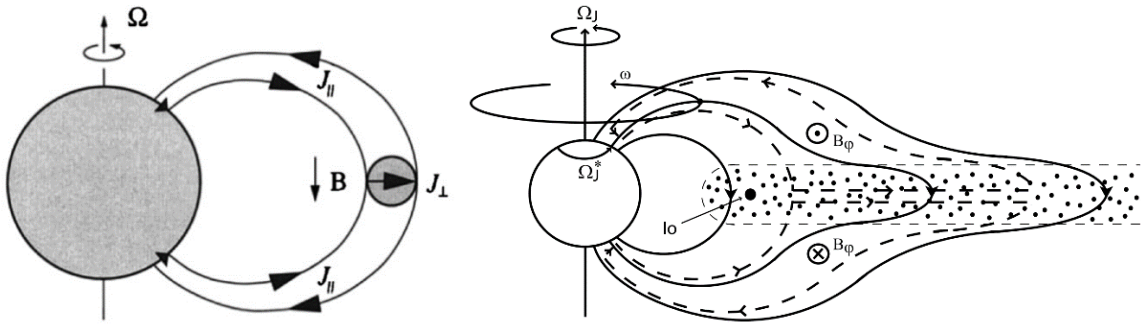

Fig 3.10 (*left*) Hill's original description of the current system due to mass loading in the magnetosphere [Su, 2008]. (*right*) Extension of the Hill's model to include an empirically derived, non-dipolar magnetic field, showing the meridian cross section through Jupiter's inner and middle magnetosphere. The arrowed solid lines indicate magnetic field lines, the arrowed dashed lines indicate the magnetosphere-ionosphere coupling current system, and the dotted region is the rotating disc of outflowing plasma. [Cowley and Bunce, 2001].

The outward current in the equatorial plasma sheet is related to a $\mathbf{J} \times \mathbf{B}$ force, however here directed in the sense of Jupiter's rotation and transferring angular momentum from Jupiter's ionosphere to the plasma, is able to speed up the plasma back to corotational speeds. The circuit is then closed by field-aligned currents, which in the inner part are directed outward, from the ionosphere to the magnetospheric plasma sheet, while in the outer part do reverse [Cowley and Bunce (2001)]. The upward field-aligned currents generated by these processes is considered at the base of the main auroral emissions of Jupiter: the radial currents accelerate electrons into the ionosphere via the action of large field-aligned potentials, generating the main aurora.

3. *Outer magnetosphere* $[> 60\ R_J]$ This region of Jupiter's magnetosphere consists of hot corotating plasma, with temperature around 20-30 keV and with a flow speed of $1000\ km\ s^{-1}$. The contribution of thermal pression by the plasma sheet, which inflate the magnetosphere, makes the Jovian magnetosphere much more compressible than the Earth's one. This is evident especially in the dayside of the outer magnetosphere, where the magnetopause can be found anywhere in between $40\ R_J$ and $100\ R_J$, depending on the solar wind dynamic pressure and under the influence of the solar wind the plasma sheet becomes parallel to its direction at distances larger than $60\ R_J$. Instead, the nightside outer magnetosphere shows a current system connecting the magnetodisk current to that of the magnetopause, causing a further stretching of the magnetotail beyond Saturn's orbit.

3.4.4 Jupiter's plasma sources and dynamics

As already pointed out, the main interplanetary plasma source is the moon Io, while a lower contribution to the Jovian magnetosphere comes from the solar wind, which is the principal external source and provides helium (tracer ion of the solar wind) and protons (protons may have different origins other than the solar wind, e.g. cosmic rays). Another significant source is Jupiter's ionosphere, which add to the magnetosphere energetic H^+, H_2^+ and H_3^+. These molecules are produced in the upper ionosphere by energetic particles precipitation and are accelerated by parallel electric fields and/or resonant and non-resonant particle-wave interactions [Hamilton et al. (1980)]. Additional, but less significant, sources of plasma are the three icy Galilean satellite Europa, Ganymede and Callisto, where Europa contributes to the Jovian magnetosphere with oxygen ions, and its neutral gas torus is an additional source of ENA (Energetic Neutral Atoms), as well as a sink of energetic protons.

In the previous section it has been highlighted the influence of Io plasma source and of the centrifugal force due to the 10 hours rotation period of Jupiter's on the structure of the planet's magnetosphere; however, they play an important role in the magnetospheric dynamics too. As a matter of fact, the Io mass and the energy, that eventually is released from the Jovian magnetosphere through processes like magnetotail reconnection and centrifugal forces relative to the solar wind, largely influence dynamics at Jupiter. To describe the expected flow pattern of the Jovian magnetosphere, Vasyliūnas (1983) has proposed a model of rotationally driven dynamics. According to this model, reconnection can occur when heavily mass-loaded flux tubes become stretched due to centrifugal acceleration of the rotating

particles, pinch off through spontaneous reconnection, and finally realise a plasmoid downtail. Therefore, the plasmoid can escape, contributing to the final evacuation of the internally produced plasma and allowing the return of the magnetic flux toward the planet. This process, referred to as *Vasyliūnas cycle*, is shown in Fig 3.10 and has been studied by inspecting possible 'local' signatures of the reconnection, as magnetic field reversals, plasma flow anisotropies, energetic particle bursts, and more global consequences on the magnetospheric activity [Louarn et al. (2015)].

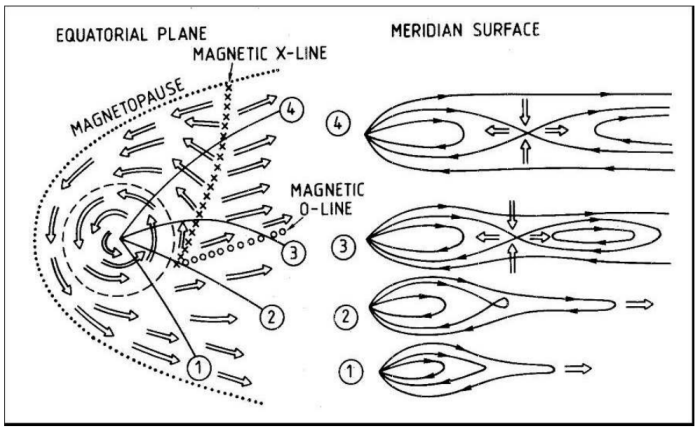

Fig 3.11 Scheme of the Vasyliūnas cycle. [Vasyliūnas (1983)]

3.5 Jupiter's aurorae

Thanks to ground- and space-based telescopes, several observations of Jupiter's auroral emissions at ultraviolet, infrared, and visible wavelengths have been realized through the years, revealing unique features and allowing to study global magnetospheric processes not yet observed by spacecrafts. Jupiter's auroral emissions can be classified in three main types: the satellite footprints, the main aurora, and the polar aurora, which are shown in Fig 3.12.

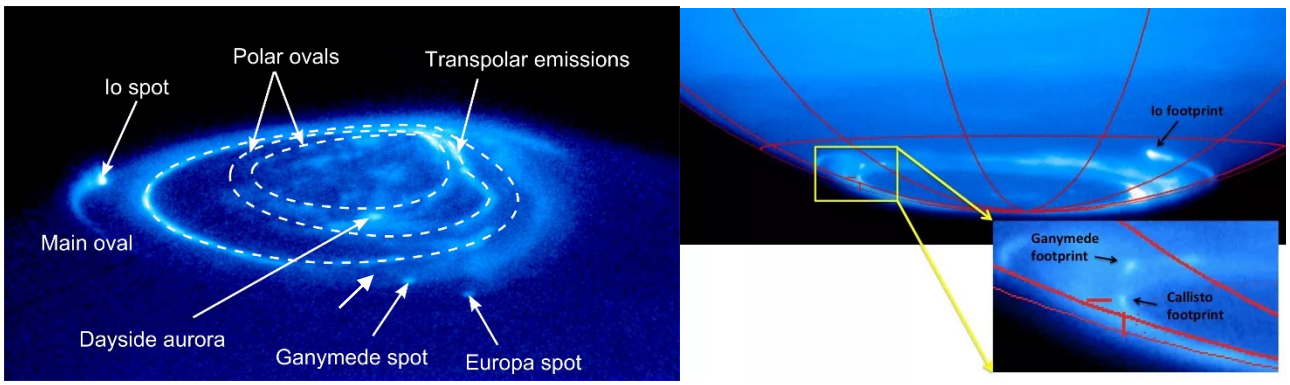

Fig 3.12 (*left*) Hubble Space telescope's image in the UV showing the main aurora features of Jupiter's aurora [Clarke et al., 2002]. (*right*) Hubble Space Telescope's image of Jupiter's south pole showing Callisto's elusive footprint. Signatures from Ganymede and Io are also visible [Bhattacharyya et al., JGR 2018].

3.5.1 Satellite footprints: Io footprint

The satellite footprints are the most equatorward components of the Jovian auroral emissions, where the ionospheric footprints of all the Galilean satellites have been observed. Io and its ionosphere act as an obstacle for the equatorial plasma source [Saur (2003)]: due to the electromagnetic interaction between Jupiter's magnetic field and the plasma surrounding Io, consisting in the propagation of Alfvén waves from Io toward Jupiter along the magnetic field line, intense auroral emissions are generated, as can be seen in the top panel of Fig 3.13. Consequently, Io leaves a magnetic footprint on Jupiter's upper atmosphere, which appears as a spot that stays connected to Io as Jupiter rotates. In fact, Io atmospheric gases are heated by inelastic collisions between the satellite's atmosphere and ions of the torus produce the acceleration of a large population of neutral molecules and atoms, exceeding Io's gravitational escape speed of 2.6 $\mathrm{km\,s^{-1}}$. The dominant neutrals generated by volcanoes on Io are sulphur and oxygen, most likely in the form of SO_2 [Su (2008)]. Io loses about 1-3 $\mathrm{t\,s^{-1}}$ of these neutrals both in molecular (SO_2, S_2 or SO) and atomic form (O, S), which create an extensive corona encircling most of the way around Jupiter. Approximately, 1/3-1/2 of this extended neutral cloud is subjected to ionization via photo-ionization, electron impact and charge exchange, adding fresh plasma consisting of heavy ions as S^+, S^{++}, O^{++} and O^+, the new *pick-up* ions, accelerated to the speed of the surrounding plasma 74 $\mathrm{km\,s^{-1}}$. Instead, the rest of the neutrals is lost due to charge exchanges between a neutral atom and a torus ion, adding gyro-energy to the ions and extracting momentum without adding more plasma to the system: once neutralized the particle is no longer confined by the magnetic field and flies of as an energetic neutral atom. Because Io orbits Jupiter with a velocity of 17 $\mathrm{km\,s^{-1}}$, the plasmas flow over the moon with a relative velocity of 57 $\mathrm{km\,s^{-1}}$ ahead of Io in its orbital motion [Su (2008)]; therefore, this flow of magnetized plasmas sweeps through the obstacle, Io, producing intense electrodynamic interactions [Kivelson et al. (2005)] and, consequently, auroral emissions. There are three types of auroral regions: the planetward current region (upward current region), the anti-planetward current region (downward current region) and the Alfvénic acceleration region. As can be seen by the top panel of Fig 3.13, the Io-induced aurora displays a bright spot on the left, which is believed to be at the base of the Io magnetic flux tube, and a trail of lower emission extending large distances eastward, referred to as the *wake aurora*. The electron acceleration that produces the bright spot is thought to be dominated by Alfvén waves, whereas the wake aurora results from quasi-static parallel fields [Ergun et al. (2009)].

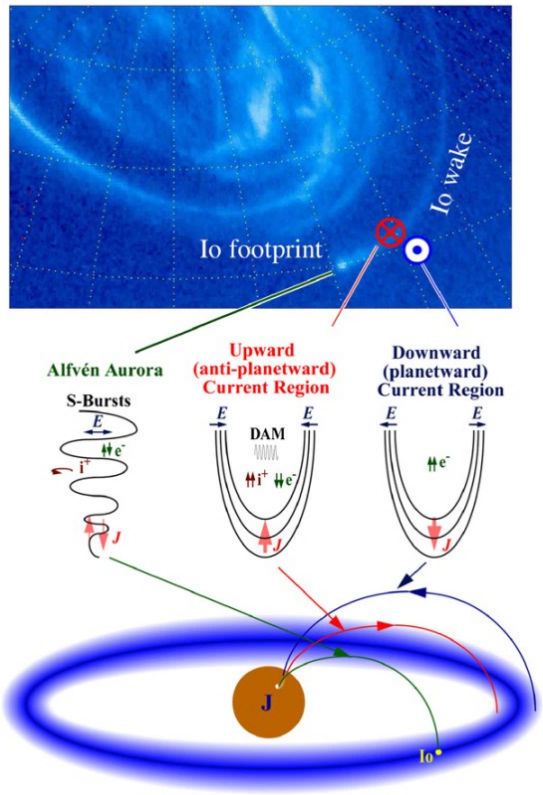

Fig 3.13 [*top*] Hubble Space Telescope image of the Jovian aurora showing the Io-induced aurora on the left, with the brightest emissions at the base of the Io flux tube and an emission trail extending downstream. [*bottom*] Three types of auroral regions. [Ergun et al., 2016]

Similar mechanisms occur in the other Galilean satellites and, according to the strength of the currents linking them to Jupiter, they may also leave footprints which consist in a main spot or multiple spots in a tail. Being each footprint magnetically connected to the correspondent satellite, the ionospheric footprints result quite a useful tool in constraining Jupiter's magnetic field models: because the satellites' orbital locations are known, hence the ionospheric location of the footprint can be linked to a radial position in the magnetosphere.

3.5.2 Main Aurora

Beside the moon footprints, Jupiter's intense aurora shows a fairly steady main auroral oval, with a patchy and more unstable aurora within it at higher latitude. This oval is quite narrow, corresponding to about 1°-3° of latitudinal band width and extending few hundreds of kilometres horizontally in Jupiter's atmosphere: it can be mapped along the magnetic field lines outside the orbit of Ganymede

at 15 R_J, but most likely to an equatorial distance of about 20-30 R_J, well inside the magnetosphere [Bagenal (2007); Clarke et al. (2002)]. The main oval exhibits a constant shape of fixed magnetic coordinates, reflecting the presence of persistent magnetospheric processes causing an almost permanent bombardment of electrons onto the Jovian atmosphere and causing the auroral emissions, which produce around 10^{14} W. Actually, the main emissions in the northern hemisphere appear bean shaped, while in the southern hemisphere the shape looks more like an oval. The physical processes behind the generation of the Jovian main aurora have already been largely discussed in section 3.4.3. Briefly resuming, the main auroral oval is considered connected to the ionosphere-magnetosphere coupling current system associated with the breakdown of the rigid corotation in the middle magnetosphere region (Fig 3.14); therefore, the main oval can be interpreted as the ionospheric footprint of the upward Birkeland current that enforces partial corotation of magnetospheric plasma moving outward from the Io plasma torus to the outer magnetosphere [Grodent et al. (2003)].

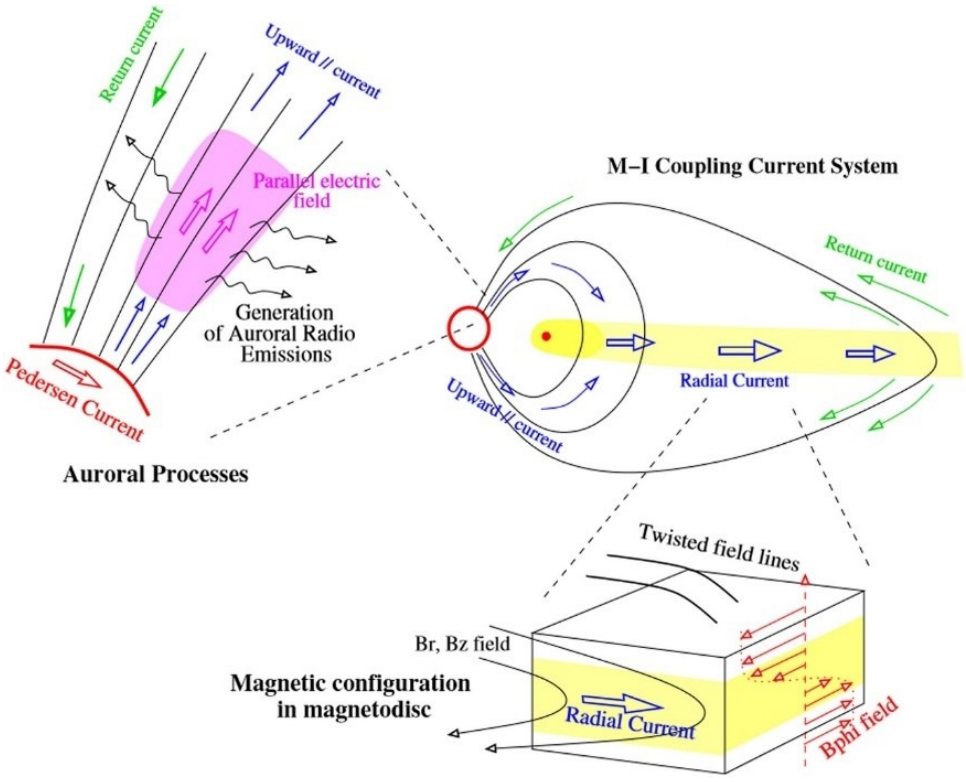

Fig 3.14 Schematic representation of the ionosphere-magnetosphere current system. [Louarn et al., 2016]

The concept of main oval can be quite misleading, leading to an erroneous idea of an approximately static and narrow polar ring of emissions generated by the same mechanisms all around Jupiter. In fact, recent studies based on far-ultraviolet observations of the Jovian aurorae have shown that several morphological variations occur in the main oval as a function of the local time (Jupiter's local time is shown in Fig 3.15): the dawn side portion forms a narrow arc, the post-noon portion consists of auroral patches, and the dusk portion appears to broaden and break from the main oval. For these reasons, it is preferred to refer to this emission as *main emission* (ME) instead of main oval emission [Grodent et al. (2007)].

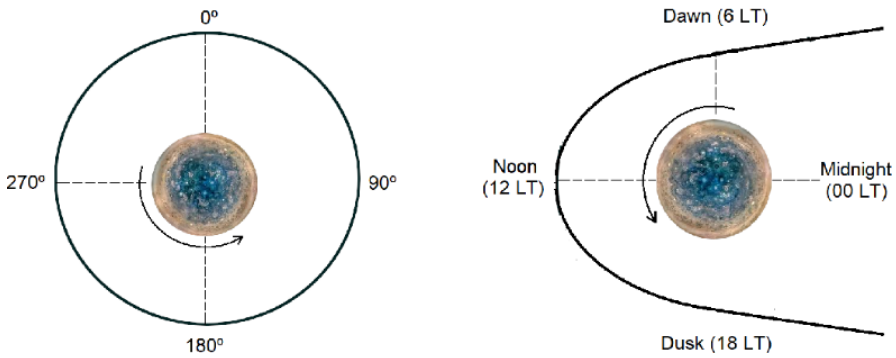

Fig 3.15 (*left*) Jupiter System III left-handed (XY plane). (*right*) Jupiter Local Time (equatorial plane). [from Cantos, I. P. (2019) *A new auroral structure on Jupiter: Jupiter's auroral bridge*]

Moreover, the main oval emission displays several characteristic features, which are associate to different sources regions. Some of the most important are:

- a discontinuity → a region where the brightness of the main oval decreases to a value less than 10% of the typical main oval brightness. Here the field-aligned current do reverse direction and flow downward into the ionosphere; therefore, because downward currents do not require acceleration of the magnetospheric electrons, the brightness of the main oval decreases and is thought to map the pre-noon local time region;
- quasi-parallel arcs on the dusk side, equatorward of the main oval;
- secondary arc poleward of the main oval appearing weaker and variable.

Nevertheless, the general shape of the ME stays approximately constant; it is, hence, possible to define a reference oval to locate the auroral emissions on the planet and use it to determine the stability of the main emission.

3.5.3 Polar Aurora

As mentioned before, a variable auroral emission can be observed poleward of the main oval, where three regions can be distinguished according to their brightness and dynamic behaviour: the active, the dark and the swirl region, of variable shapes and locations as Jupiter rotates.

1. *Active region*. The analysis of the Jovian auroral observations have revealed the presence in both the hemispheres of flares, bright spots, and arc-like features at the footprint and in the vicinity of the polar cusp regions, where the magnetosheath plasma have direct access to the ionosphere. These flares show a brightness of few hundred kR (Rayleigh[4]), thus comparable with that of the main oval typically 50-500 kR, which can be generated by the disturbance of the magnetosphere due to increasing solar wind dynamic pressure. Instead, *Grodent et al.* (2003), basing on flares' characteristic minutes-long time scale, interpreted these features as explosive magnetopause reconnection on the day side. Also, the arc-like structures are thought to be the signature of *Dungey cycle* dayside x-line, which is a process during where the field lines opened to the day side are pulled back by the solar wind, reconnect in the tail and finally convect back to the dayside (Fig 3.16).

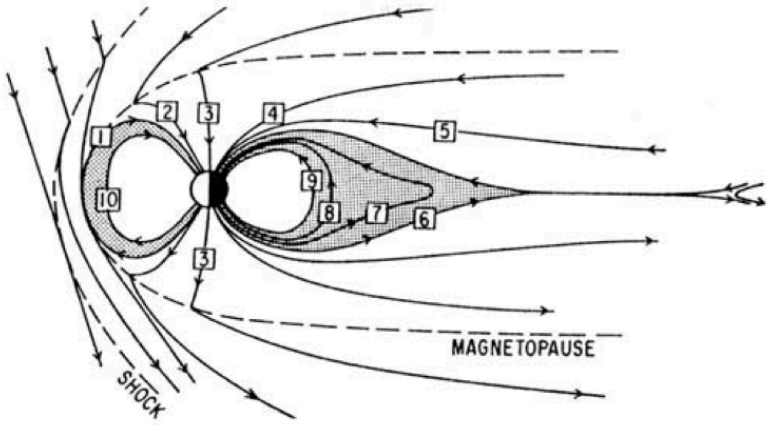

Fig 3.16 Dungey cycle's steps in a meridional plane. Step [1] shows the reconnection occurring on the day side between the earth's northward-oriented and the southward interplanetary magnetic field. In steps [2-4] the field lines which are opened on the day side are pulled tailward by the solar wind. In step [6] the field lines close again through tail reconnection and in [7-9] these lines convect back to the day side. [Axford, 1969]

[4] Rayleigh unit (R): it is a unit of photon flux used to measure faint light emitted in the sky such auroras. One rayleigh (1 R) is defined as a column emission rate of 10^{10} photons per m^2 per column per second.

This solar wind-induced convection pattern would carry flux over the poles, however there is no evidence yet; moreover, it is not known how much of the polar flux is open to the solar wind. A schematic representation of the active region in Jupiter's northern aurora is presented in Fig 3.17b.

2. *Dark region*. This region can be detected just above the main oval, in the down to pre-noon local time sector, appearing as a crescent-shaped region devoid of emission (0-10 kR), hence dark in the UV. Even if this region is fixed in local time, several observations have revealed a significative size variability during compressions of the magnetosphere by the solar wind as Jupiter rotates. According to *Grodent et al.* (2003), the rotational Dark Polar Region (r-DPR) is associated to the Vasyliūnas cycle return flow, whose position in the Jovian equatorial plane and in Jupiter's northern ionosphere is pointed out in Fig 3.17. More in detail, the solar wind pression acting on the magnetosphere's dayside cause the compression of the magnetosphere: the inward motion on the dawn side reduce the ionospheric loading resulting in a dark region in the dawn polar aurora; instead, on the dusk side the plasma expands outwards and strong currents try to keep it corotating, causing the active dusk polar aurora [Bagenal (2007)].

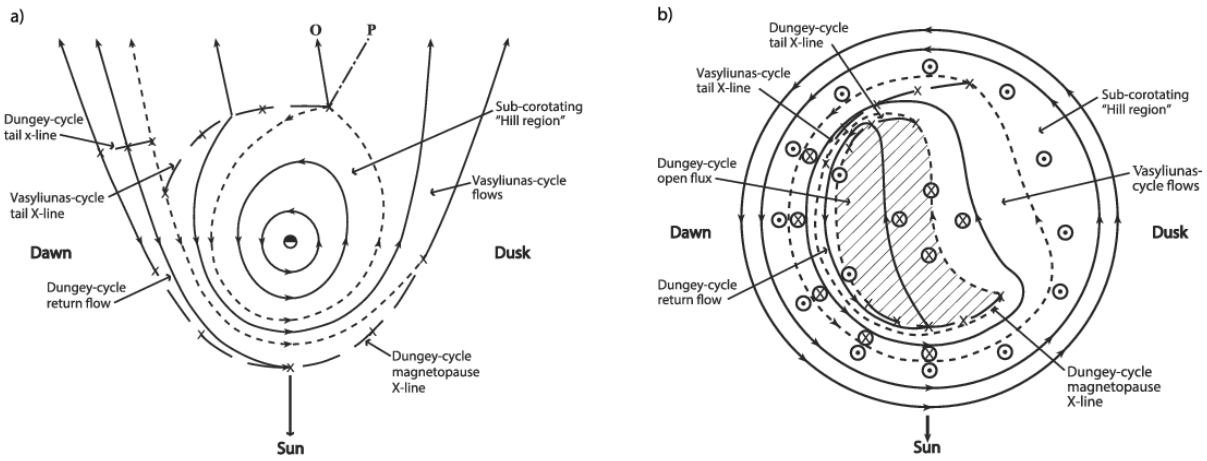

Fig 3.17 (a) Representation of the flows in the Jovian equatorial plane. Here, the solid lines show the closed plasma streamlines; instead, the dashed lines marked with a cross highlight the Dungey and Vasyliūnas cycles X-lines. **(b)** Polar view of the Jovian northern ionosphere, where the upward field-aligned currents are identified by the circles with a dot, while those with a cross denote regions of downward field-aligned currents. Here, the hatched area represents the open region based on the results from *Stellard at al.* (2003). [Johnson et al., 2017]

3. *Swirl region.* This region can be found slightly at the centre of the polar emissions, poleward of the dark and active regions. This area appears rather patchy and it is characterized by transient emission showing swirling motions and it is considered as mapping to open field lines.

Moreover, the polar auroral emissions show transitory spots equatorward the dark region, which are thought to be the signature of the flow associated to the reconnection process.

3.5.4 H_3^+ and its discovery on Jupiter

Tennyson and Miller (1994) defined H_3^+ as *the simplest polyatomic molecule, which has long been known to be an important constituent of hydrogen plasmas that are prevalent in many location of the Universe.* H_3^+ is in fact made of 3 protons (the 3 hydrogen atoms nuclei) and two electrons. Its first detection date back to 1912, when Thomson J. J. discovered a particle with a mass-to-charge ratio of 3, violating all the rules of chemical bonding. Initial studies failed in predicting the equilibrium structure of H_3^+, however they showed that the molecule's formation is favoured by the exothermic reaction

$$H_2 + H_2^+ \rightarrow H_3^+ + H \tag{3.2}$$

which is a rapid reaction, even at low temperature, that forms hot H_3^+ at nearly every collision. However, as already explained in the first chapter of this thesis, in order to detect a molecule in space it is necessary to know and understand its spectrum. Early attempts to observe H_3^+'s spectrum were unsuccessful, because the molecule does not have either rotational or electronic spectrum; moreover, the vibrational spectrum, which lies in the infrared region, is highly irregular and does not follow the usual regular patterns used to analyse the vibrational spectra.

The importance of the H_3^+ ion in the interstellar medium composition was highlighted with the discovery of the diversity and the complexity of the interstellar chemistry compared to that of the Earth. In fact, due to its nature, the typical gas phase three-body reactions occurring on Earth are quite unlikely in the interstellar medium (ISM). Also, in the ISM the energy available is not enough to overcome the reaction's energy barriers that on Earth can be exceeded by providing some initial energy. Therefore, scientists started to hypotise new ion molecule reactions and new and more

sophisticated models of the ISM, where the H_3^+ (produced by ionization of H_2 by cosmic ray) plays the important role of protonating agent

$$X + H_3^+ \rightarrow XH^+ + H_2 \tag{3.3}$$

where X is the stable species. H_3^+ spectrum was observed in the laboratory for the first time by Oka (1980) and, using his measurements as a reference, scientists tried to directly observe it in the interstellar medium. However, this was not an easy task: because the molecules tend to form in very cold regions of the ISM, H_3^+ cannot be seen in emission, while the problems with the absorption spectrum is that a radiation source is required; moreover, due to the low temperatures, the only possible transitions of H_3^+ fall in the spectral region of the water absorption in the Earth's atmosphere. Despite these difficulties, thanks to the improved instrumentation, in the '80s at Mauna Kea, Hawaii, the first ever astronomical detection of a H_3^+ spectrum was realized [(Oka (1980)]. However, this discovery was made after the Voyager missions, which detected hot regions near both the north and south poles of Jupiter, with temperatures much larger than 200 K (typical for most of the planets) and containing a number of hydrocarbates not observed elsewhere. This event led *Drossart et al*. to study the infrared emission spectrum of the molecular hydrogen in Jupiter's hot polar regions and in September 1988, using the Fourier transform infrared (FTIR) spectrometer on the Canada-France-Hawaii Telescope on Mauna Kea, beside the three molecular hydrogen transitions they were looking for, 33 other lines of unknown origin were observed. Later, Watson associated some of these lines to H_3^+ [Watson et al. (1980)] and further studies confirmed that the hot rotational temperatures obtained from the H_3^+ polar emissions, oscillating between 650 K and 1200 K, reflected the true temperature of the environment.

When looking at Jupiter in a certain range of wavelengths sensitive to H_3^+, namely in the 3-4 microns region, the planet appears dark, because most of the radiation emitted or scattered by Jupiter's lower atmosphere is totally absorbed by the Jovian atmosphere, especially by methane [Connery and Satoh (2000)]; therefore, the only bright features that can be observed near the poles are due to the H_3^+ emissions, which are visible only because they occur high in the atmosphere, well above the methane layer. The cause for these emissions in the polar regions has to be associated to the strong magnetic field of Jupiter, which, as already discussed in the previous sections, can strongly influence vast areas by accelerating charged particles, that then spiral down the magnetic field lines and ionize molecular

hydrogen by collisions leading to the formation of H_3^+. Because the different particles flow along different magnetic lines entering Jupiter's upper atmosphere at diverse locations, by studying the morphology of the H_3^+ aurora it is possible to distinguish between the two sources of charged particle: the solar wind, which is a steady stream of particles emitted by the Sun, or Jupiter's moon Io, which generates a ring of particles surrounding Jupiter.

Concluding, by monitoring the H_3^+ emissions detailed information about the Jovian auroral activity can be obtained.

4. Detection of H_3^+ and CH_4 on Jupiter by Juno/JIRAM

4.1 H_3^+ and CH_4 detection in Jupiter's auroral regions

4.1.1 H_3^+ emissions

As already said in the previous chapter, H_3^+ represents an important ion in the Jovian upper atmosphere, whose emissions at infrared wavelengths can be studied to determine the auroral processes and satellite interactions leading to the energy deposition in the upper atmosphere of Jupiter's polar regions. H_3^+ emissions are the consequence of chemical reactions occurring in the Jovian ionosphere. H_3^+ is formed through reactions with the H_2^+ ion. In particular, H_2^+ forms from photoionization and electron impact ionization processes, such as

$$\begin{aligned} H_2 + h\nu &\rightarrow H_2^+ + e \\ H_2 + e^* &\rightarrow H_2^+ + 2e \end{aligned} \tag{4.1}$$

where $h\nu$ is the solar extreme ultraviolet radiation associated with photoionization, that gives a lower contribution across the illuminated disc of the planet; while, the dominant process at polar latitudes consists of H_2 dissociation and ionization due to electron impact, where e^* represent electrons energetic enough to produce further ionization, hence, responsible for UV emissions. At higher altitudes, where H density exceeds that of H_2, H_2^+ is converted in H^+ trough charge exchange, and the reaction between H_2 and H^+ results in the production of the H_3^+ ion:

$$\begin{aligned} H_2^+ + H &\rightarrow H^+ + H_2 \\ H^+ + 2H_2 &\rightarrow H_3^+ + H_2 \end{aligned} \tag{4.2}$$

Instead, at lower altitudes H_2 exceeds H and H_3^+ can be, hence, produced thanks to the reaction of H_2^+ molecules with a neutral H_2, i.e.

$$H_2^+ + H_2 \rightarrow H_3^+ + H \tag{4.3}$$

The H_3^+ is then removed by dissociative recombination and converted in neutral hydrogen in the upper atmosphere, as

$$\begin{aligned} H_3^+ + e &\rightarrow H_2 + H \\ H_3^+ + e &\rightarrow H + H + H \end{aligned} \tag{4.4}$$

whereas in the lower atmosphere, below the homopause, the trihydrogen cation quickly reacts with methane and is converted in hydrocarbon ions:

$$H_3^+ + CH_4 \rightarrow CH_5^+ + H_2 \tag{4.5}$$

Throughout the years, both space and ground-based telescopes revealed the presence of H_3^+ emissions also in non-auroral regions, at mid-to-low latitudes, whose intensity are typically only a few percent of those in the auroral regions. These emissions may be a consequence of elevated temperature or H_3^+ densities' increase. As a matter of fact, even if H^+ is the principal ion in Jupiter's atmosphere, when H_2^+ is vibrationally excited due to energetic particles precipitation, thermospheric temperature do rise to elevated values and H_3^+ abundance in the Jovian ionosphere increases dramatically, up to 1000 times with an energy input of 10^{14} W. It is thought that H_3^+ molecules may be transported from the polar regions, where they are largely produced, to mid-to-equatorial latitudes or directly produced locally from precipitation of particles with energies of a few keV [Adriani et al. (2017); Migliorini et al. (2019)].

As already mentioned in section 3.5.4, the 3-4 μm is the most suitable spectral region for mapping the H_3^+ thermal emissions; therefore, by considering the atmosphere optically thin, the relative intensity of multiple H_3^+ emission lines can be used to determine H_3^+ densities. Moreover, because the surrounding atmosphere quickly thermalizes the trihydrogen ions after their formation, H_3^+ IR emission lines can be used to derive the atmospheric temperature [Stallard et al. (2002)].

4.3.2 CH_4 emissions

The last twenty years of Jupiter's Earth-based observations revealed the 3.3 μm CH_4 emissions in the internal part of the auroral main oval, in both the Jovian poles [Kim et al. (2015)]. The northern polar region has provided more information about the horizontal distribution and temperatures of the emitting molecules, thanks to its favourable orientation with respect to the Earth; however, some hydrocarbons emissions have been detected near the south pole too. Other measurements have been performed by space-based instruments, such as Cassini/Composite Infrared Spectrometer, which probed Jupiter atmosphere at wavelengths longer than 3 μm, and Galileo/Near-Infrared Mapping Spectrometer (NIMS), whose data set were used by *Altieri et al.* (2016) to map, along with H_3^+, the

3 μm CH_4 and C_2H_2 emissions on Jupiter's north pole. As a matter of fact, as already mentioned in the previous section, the 3 μm spectral range shows a strong methane absorption band, which masks the thermal emission from the lower atmosphere of the planet and enables the observation of H_3^+ emissions. Moreover, if the auroral activity heats the outer layer of Jupiter's atmosphere, the resulting excitation of the CH_4 molecules generates thermal emissions, which make methane's vibrational bands visible around 3.3 μm. Therefore, because the R (peaked 3.26 μm), Q (3.32 μm) and P (3.39 μm) branches of methane's ν_3 band lie in the spectral range considered for mapping the H_3^+ emissions, the contribution of CH_4 emissions has to be taken into account. That being said, a set of tools to derive auroral-emitting species composition, temperatures, and column densities has been developed and tested in the study of NIMS spectra in view of the data collected by the Jovian InfraRed Auroral Mapper instrument (JIRAM): an imager/spectrometer on board of Juno satellite, specifically designed to study the complex Jovian auroral morphology and the magnetospheric mechanisms leading to the aurorae's occurrence.

4.2 Juno and JIRAM

4.2.1 Juno spacecraft and subsystems

Juno is a solar powered spacecraft characterized by three massive solar panel wings and it is equipped with different subsystems:

i. ***Propulsion System***: for weight savings and redundancy, Juno uses a dual-mode propulsion subsystem, with a bi-propellant main propulsion system and a mono-propellant reaction control system thruster. The Leros-1b m is a 645 N bi-propellant thruster using hydrazine-nitrogen tetroxide, which is fixed to the spacecraft body firing, used for major manoeuvres and flushing burns; while the 12 reaction control system thruster are mounted on four rocket engine modules and used for translations and rotations around three axis, as well as trajectory corrections.

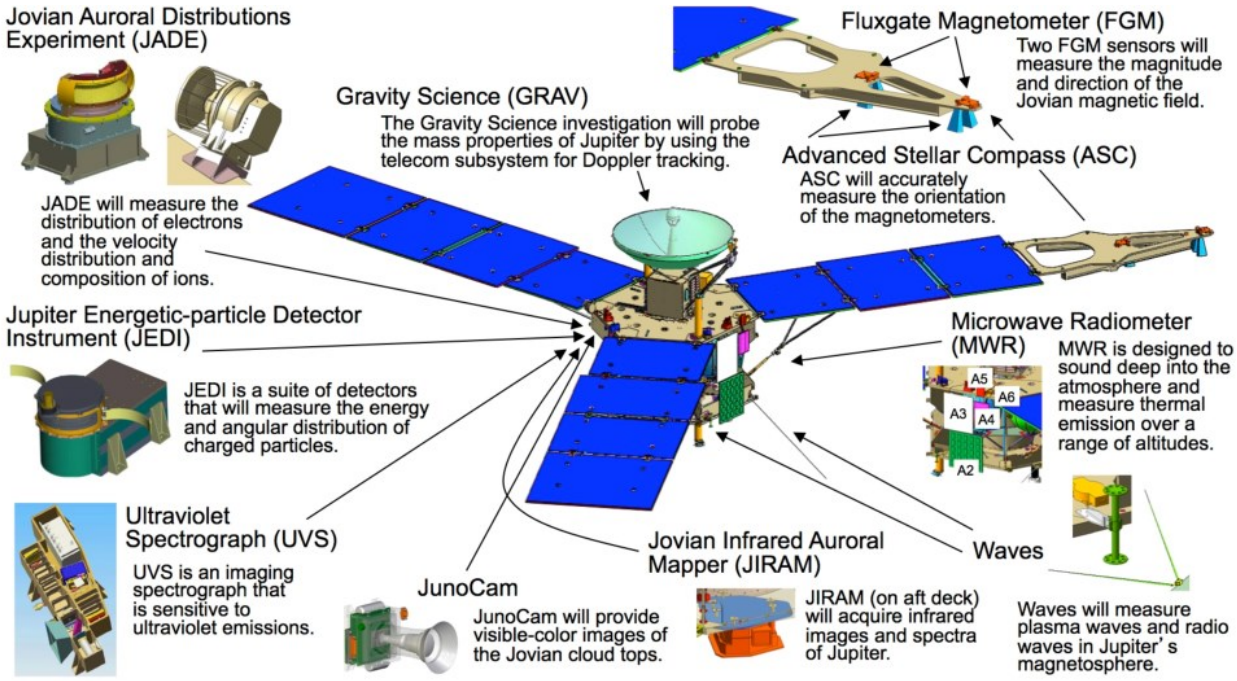

Fig 4.1 Juno's instruments. [NASA]

ii. ***Data System***: the data handling system include a RAD750 flight processor with 256 megabytes of flash memory and 128 megabytes of DRAM local memory, which provides 100 Mbps total instrument throughputs.

iii. ***Electronics Vault***: Juno carries a radiation-shielded electronics vault, in order to protect the spacecraft electronics in Jupiter's heavy radiation environment. The vault is made of a titanium metal of one-centimetre thickness, able to limit the radiation exposure of the data handling and distribution units of the power and of many other electronic assemblies, for a total weight of 180 kg.

iv. ***Power System***: the power generation is provided by three solar arrays 2.9 m wide and 8.9 m long, consisting of 11 individual solar panels and one MAG boom (Magnetometer boom). Due to its distance from the sun, Jupiter receive 25 times less sunlight than Earth; this is the reason the surface area of the solar panels has to be so large to generate enough power. Instead, when Juno is off-sun or in eclipse two 55amp-hour lithium-ion batteries provide power.

v. ***Thermal Control System***: in order to accommodate all mission thermal environments from Earth to Jupiter, where warming sun radiation is limited, the electronic vault and the propulsion module are insulated and maintained in a stable environment by heaters and louvers.

vi. ***Communication System***: this system work both as a science instrument and communication subsystem. A High Gain Antenna is mounted on the top the spacecraft core supports X-band communication with Earth, for command uplink and science data and engineering telemetry downlink. The subsystem also provides for dual-band (X- and Ka-band) Doppler tracking for gravity science at Jupiter.

The science payload carries ten instruments (Fig 4.1) to achieve the primary objectives of the mission [see section 3.1]:

i. **Microwave Radiometer (MWR) →** A microwave radiometer of multi-wavelength range which measure the abundance of water and ammonia in the deep layer of Jupiter's atmosphere, up to 200 bar.

ii. **Jovian Infrared Auroral Mapper (JIRAM)** → An image spectrometer with the objective to probe the upper layers of Jupiter's atmosphere at IR wavelengths (2-5 μm) to study its chemistry and dynamics (Fig 4.2, *left*).

iii. **Fluxgate Magnetometer (FGM)** → Used to map Jupiter's magnetic field and to determine the dynamics of Jupiter's interior and 3D structure of the polar magnetosphere and its auroral region.

iv. **Advances Stellar Compass (ASC) →** A star tracker camera that provides accurate information about the Juno spacecraft pointing for precise mapping.

v. **Gravity Science (GS)** → An experiment and instrument of Juno to monitor Jupiter's gravity by using the high-gain K-band and X-band, which returns a map of Jupiter's gravitational field, helpful to understand Jupiter's interior.

vi. **Jovian Auroral Distributions Experiments (JADE)** → An instrument that detects and measures ions and electrons in Jupiter's auroral region and magnetospheric plasmas, returning in situ data.

vii. **Jupiter Energetic-particle Detector Instrument (JEDI) →** Used to collect data on energy, spectra, mass species (H, He, O, S), and angular distributions, helpful in the study of energies and distribution of charged particles.

viii. **Radio and Plasma Wave Sensor (WAVES) →** Designed to detect radio spectra (50 Hz – 40 MHz) and plasma spectra (50 Hz – 20 kHz) in the auroral region to identify the auroral currents determining Jovian radio emissions and acceleration of the charged particles in the auroral region.

ix. **Ultraviolet Spectrograph /Ultraviolet Imaging Spectrometer (UVS) →** An imaging spectrometer that observe the UV range of light (70 nm – 200 nm) for remote observations of the aurora, detecting the emission gases (H) un the far-ultraviolet (Fig 4.2, *right*).

x. **JunoCam (JCM) →** A pushframe visible light camera that, being located on a spinning spacecraft, uses time-delayed integration to build up a signal (Fig 4.3).

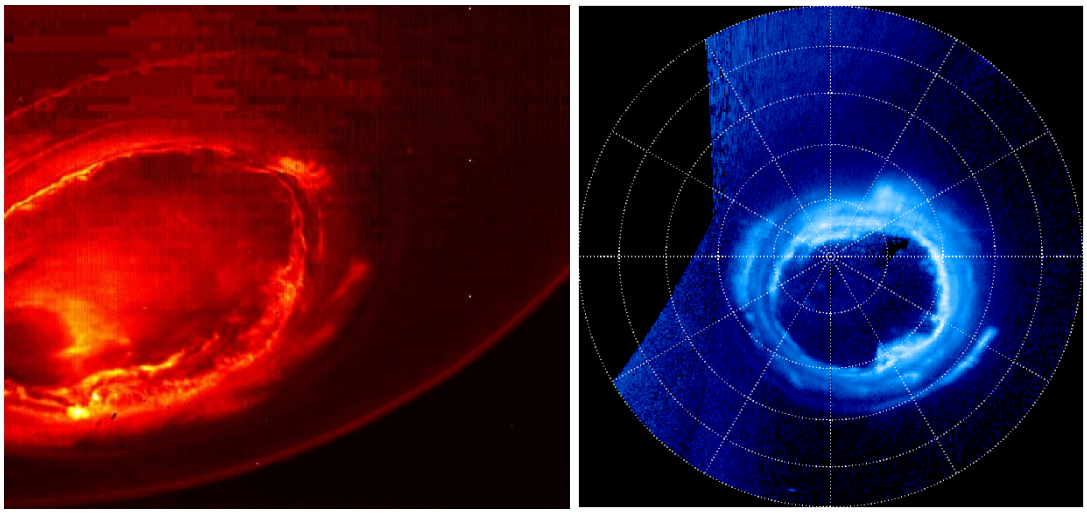

Fig 4.2 (*left*) Infrared image of Jupiter's southern aurora as seen by JIRAM in the spectral range 3.3-3.6 μm at a distance of 500,000 km from the planet on August 27, 2016, during Juno's first orbit. This view consist is a mosaic of three images taken just minutes apart from each other, about four hours after the perijove pass, while the spacecraft was moving away from Jupiter. (*right*) Ultraviolet image of the Jovian south aurora captured by the ultraviolet spectrograph. [NASA/JPL-Caltech/SwRI/ASI/INAF/JIRAM, A. Mura]

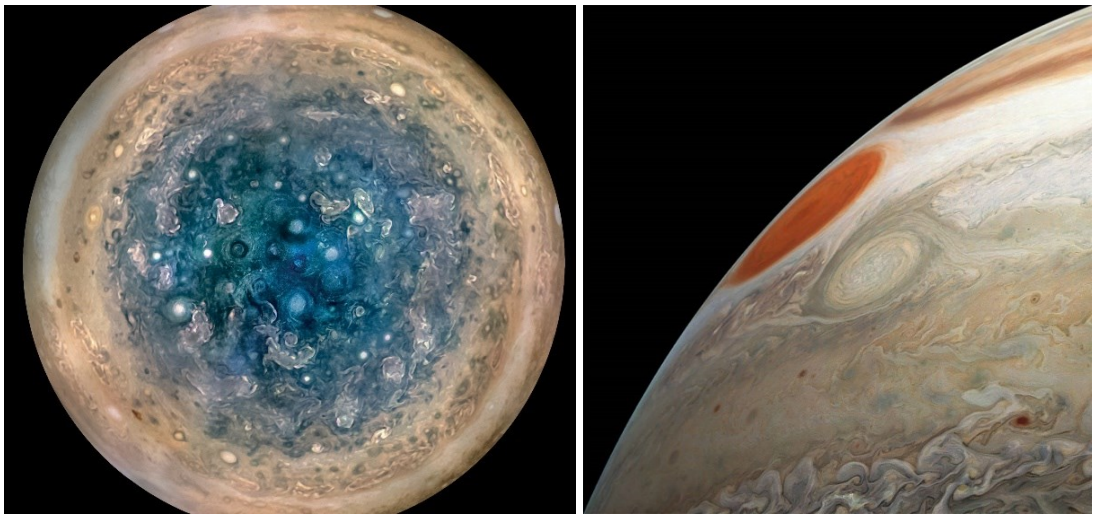

Fig 4.3 (*left*) View of Jupiter's south pole, as seen by NASA's Juno spacecraft from an altitude of 52,000 km obtained by combining multiple images taken with the JunoCam instrument on three separate orbits to show all areas in daylight, enhanced color, and stereographic projection. The oval features are cyclones 1,000 km in diameter. (*right*) Image of Jupiter's turbulent southern hemisphere captured by the JunoCam instrument on December 21, 2018, showing the notable Great Red Spot, as well as a massive storm Oval BA. [NASA/JPL-Caltech/SwRI/MSSS]

4.2.2 JIRAM Instrument

JIRAM (Jovian Infrared Auroral Mapper) is an infrared imager/spectrometer on board of Juno spacecraft, based on the heritage coming from three other space-borne imaging spectrometers that have observed Jupiter in the past: NIMS (Near Infrared Imaging Spectrometer) aboard the Galileo orbiter, VIMS (Visual and Infrared Mapping Spectrometer) aboard Cassini and PERSI/Ralph on board the New Horizon mission to Pluto. However, JIRAM has different constrains that make this instrument unique: distinct from the other outer solar system explorers, Juno is not a three-axis stabilized platform, but a spinning spacecraft with a spinning rate around 2rpm, namely 12 deg/s. To adapt the instrument to such a platform and allow the target scene to stay stable in the instrumental Field of View (FOV) for up to 1.1s, a de-spinning flat mirror, counter-compensating the spin motion, is positioned at the JIRAM telescope's entrance pupil. Also, the instrument is composed of optical and electronics components accurately selected and designed to survive the harsh Jovian environment.

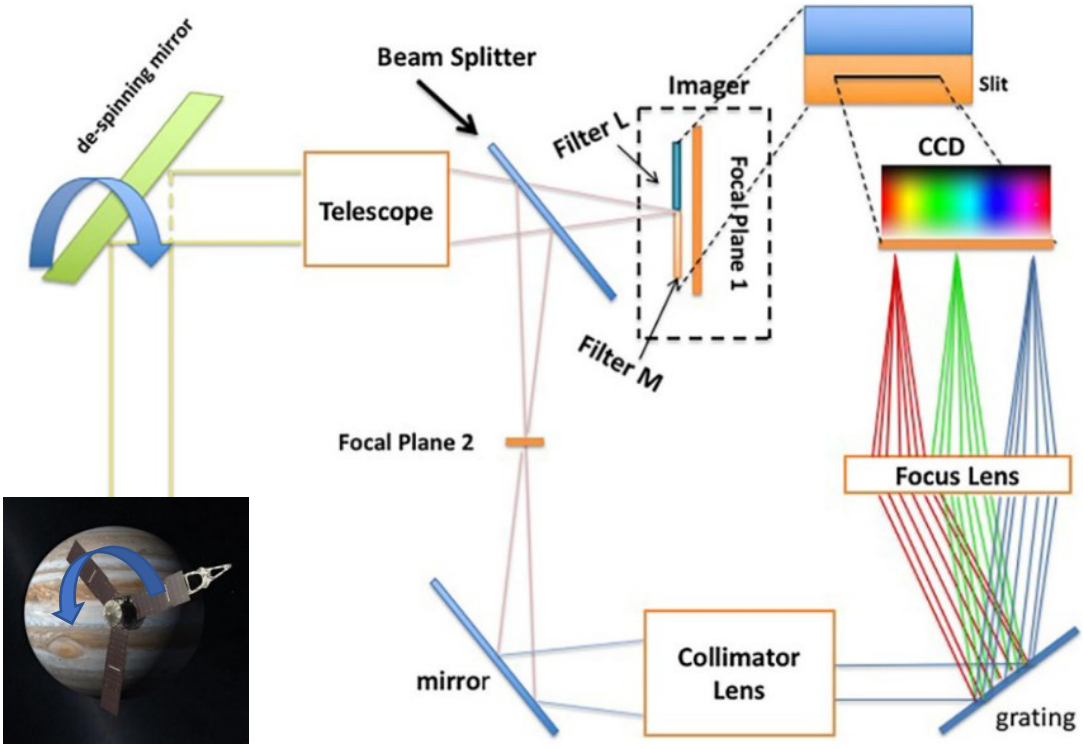

Fig 4.4 JIRAM instrument scheme. [Noschese et al., 2019]

The JIRAM instrument operates in a limited range of infrared wavelengths, 2-5 μm, using a dual-channel infrared imager and an imaging spectrometer sharing the same telescope, de-spinning mirror and the internal calibration unit. JIRAM's optical head is mounted on the aft deck of the vehicle, assuring that the instrument is in shade during all the phases of the mission in which its operation is

required. Moreover, the instrument is equipped with two radiators which passively cool it down to optimal operational temperatures, in order to reduce noise sources. The optical layout is based on a modified Schmidt telescope and thanks to a beam splitter, the optical beam is divided between the imager channel (30% of the light is focused in Focal Plane 1) and the spectrometer channel (70%, of the light is focused in Focal Plane 2) (Fig 4.4). Both the imager (IMG) and spectrometer (SPE) use the same HgCdTe detector type having a format of 270 x 438 pixels arrays and the data are recorded in a subset of these pixel: 256 x 336 pixels for the spectrometer and 256 x 432 pixels for the imager. The imager focal plane is itself divided into two equal areas defined by the superimposition of two different band-pass filter separated by an opaque region of about 10 pixels (Fig 4.5, *top panel*): filter L, centred at 3.455 μm and filter M centred at 4.780 μm. Both L and M channels have a FOV of 128 x 432 pixels (along and across track respectively) and an IFOV of 250 x 250 μm. The L-band (3.3-3.8 μm) is designed to obtain high resolution images of the H_3^+ emissions of the polar aurora, while the M-band is used to image the deeper atmosphere. To highlight the differences between the two filters, Fig 4.6 shows Jupiter's moon Io as seen by JIRAM both in the L and M bands.

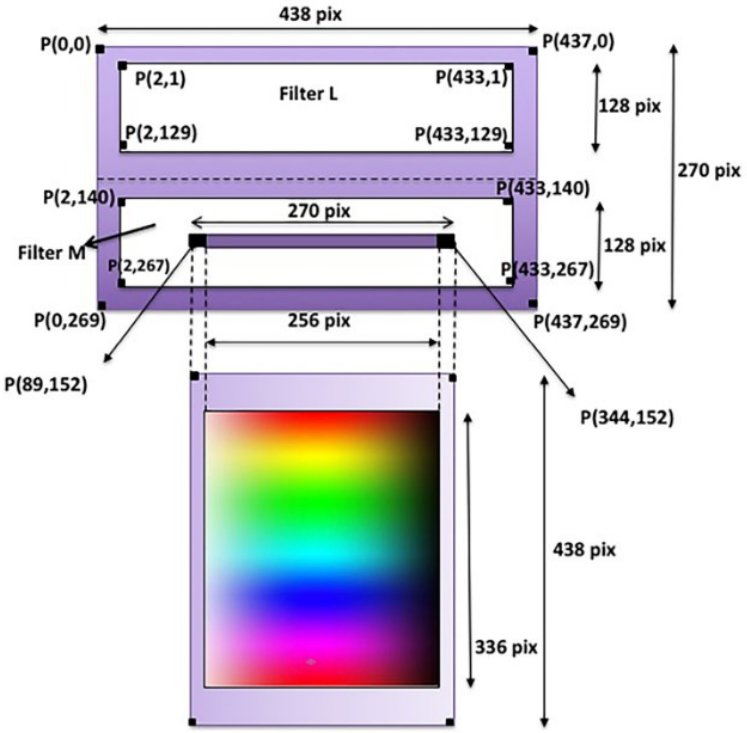

Fig 4.5 JIRAM's detectors layout.: (*top panel*) imager FOVs and (*bottom panel*) spectrometer channel detector. [Noschese at al., 2019]

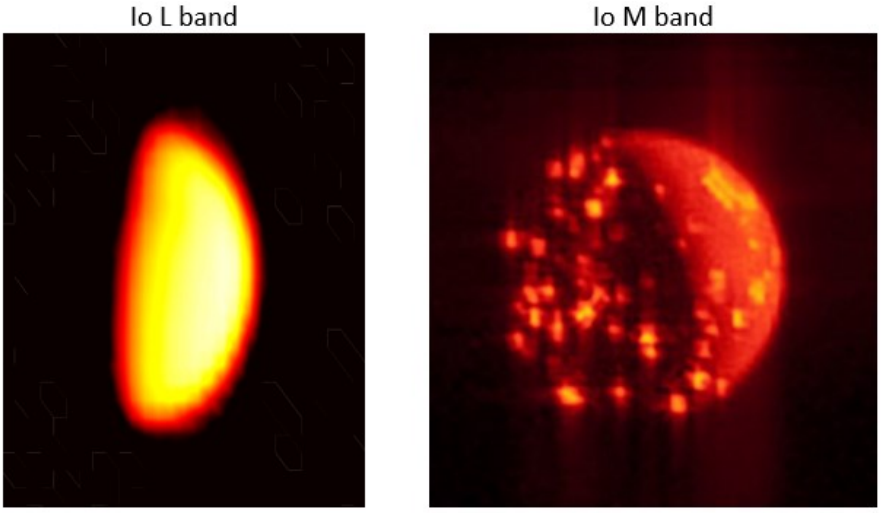

Fig 4.6 (*left*) Infrared image of Jupiter's moon Io derived from data collected by JIRAM in the L band. (*right*) Infrared image of Io's southern hemisphere derived from data collected by JIRAM in the M band, showing multiples volcanoes and hot spots (the brighter the color the higher the temperature recorded by JIRAM). [NASA/JPL-Caltech/SwRI/ASI/INAF]

Regarding the spectrometer, the optical beam is firstly deflected by a mirror and then collimated on a grating which separates it into different wavelengths, then focused by a lens on the Focal Plane 2 (Fig 4.5, *bottom panel*). This configuration maximizes the scientific return, enabling the co-located imaging spectroscopy in the 2-5 μm wavelength interval (8.99 nm/band resolution) in the M-filter channel FOV. In fact, as already mentioned in section 4.2.1, the JIRAM instrument has two main science objectives:

1. the study of the composition and dynamics of the Jovian atmosphere using the spectrometer and the imager M band: while the spectrometer identifies the chemical species and their abundance in Jupiter's atmosphere, the imager M-band provides a higher spatial resolution, allowing to study the atmospheric dynamics, e.g. polar cyclones (Fig 4.7), atmospheric waves, wind speeds, etc.

2. the study of Jupiter's aurorae using the spectrometer and the imager L band: the spectrometer allows to determine the concentrations and temperatures of the H_3^+ ions, as well as to identify the presence of methane, whereas the imager L enables the study of the morphology of the auroral emissions with an unprecedent spatial resolution.

Due to Juno's spinning motion, JIRAM's acquisition time frame cannot exceed 30 s, while the integration time for each spectrum on the slit is 1 s. Because the de-spinning mirror compensates for the spacecraft rotation, each slit of the spectrometer is combined to provide an hyperspectral 3D image, called *image cube,* where the X dimension of the cube corresponds to the cross-track direction (samples), the Y dimension is collected along track (lines), while the λ dimension is provided by the wavelength (bands), hence depends on the spectrometer spectral range.

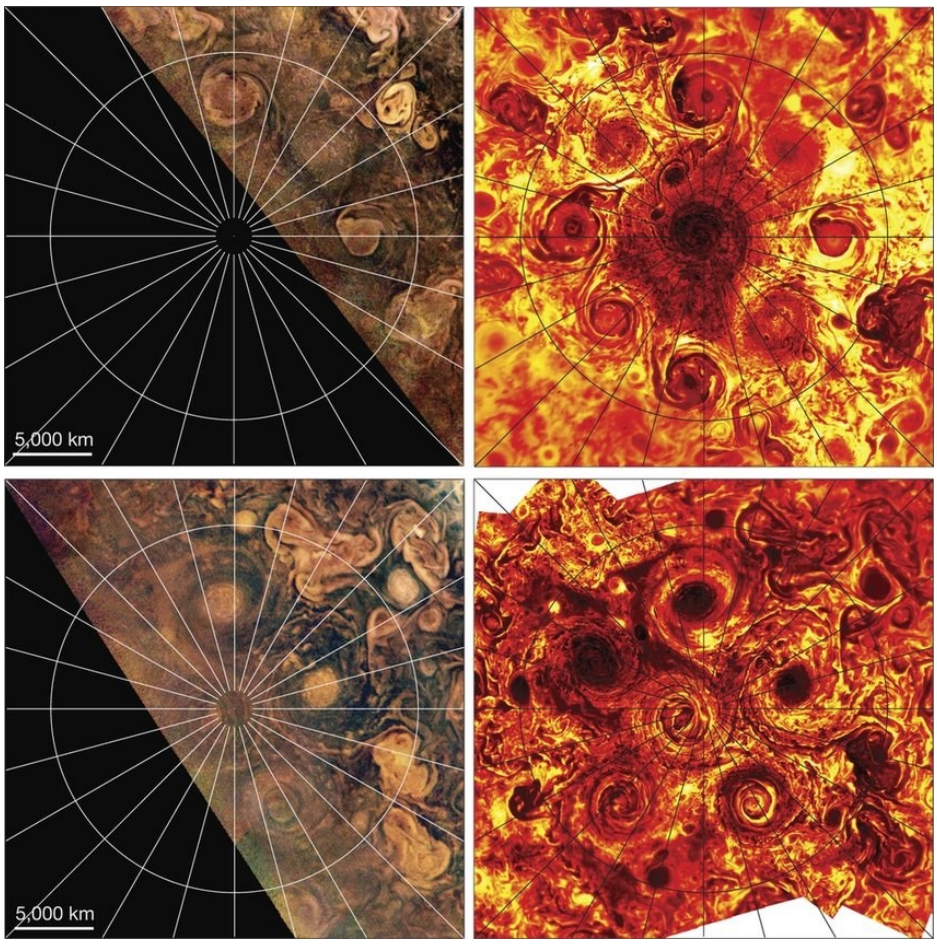

Fig 4.7 Projected (planetocentric) maps of the regions surrounding Jupiter's north pole (*top*) and south pole (*bottom*), from the JIRAM M-filter observations (right panels) and JunoCam coulor-composite images (*left panels*), showing cyclonic features clustered around each pole. By operating at thermal-infrared wavelengths, JIRAM observes these atmospheric structures regardless of solar illumination, while JunoCam's images are restricted to only the illuminated regions. [Adriani et al., 2018]

4.2.3 Planning strategy

Each Juno's orbit is composed by two planning sequence:

- *Perijove sequence* → starts one day before the perijove and terminates one day before the apojove. Typically, JIRAM observation windows start 18 hrs before the perijove and end 23 hrs after it, operating at distance lower than 20 R_J.
- *Apojove sequence* → starts from where left by the preceding perijove sequence and continues up until one day before the subsequent perijove.

At the time of Juno's arrival, in July 2016, its orbit was approximately aligned with down-dusk line and the perijove latitude was slightly north of the equator. However, with the evolution of the trajectory the perijove latitude has shifted northward, with the consequent increase of the orbit's tilt relative to the orbital plane; therefore, Juno makes quicker passes over the Jupiter's north pole. As a consequence, JIRAM guaranties a great coverage of the south pole, while it has less time to observe the north pole. In the polar regions the main goals for each orbit are:

1. to observe Jupiter's auroras and to obtain at least one global map of each auroral region, by merging several single L-band images into one (usually 50 images are used to create a mosaic). However, north aurora global imaging appears more difficult, because JIRAM devotes a longer period of observation of the southern polar region, where one or two global maps can be obtained, while it spends less time over the northern polar region;
2. to track and monitor the polar vortices and their evolution;
3. to image Jupiter's moon Io and study the evolution of its volcanoes;
4. to study the atmosphere using the M-band filter, where, again, the south polar region has a better coverage.

Instead, away from the polar regions JIRAM performs the global mapping of the atmosphere using both the M-band imager and the spectrometer. Moreover, from around orbit 15, due to Juno's orbit precession, in the phase of closest approach to the perijove JIRAM can perform limb observations, exploiting the fact the its FOV is partially or completely outside the planetary disk.

4.2.4 Science observations

During the first Juno's orbit (JM0001), JIRAM was turned on for the first time after the encounter with the Moon at the early stage of Juno travel to Jupiter, and observed Aldebaran (α Tauri) and the Hyades, which were used to perform the geometrical calibration of the instrument. JIRAM team used Aldebaran to evaluate the difference between the reconstructed geometry of the observations and the predicted one. Once the geometrical calibration was concluded, the instrument started to execute a series of science observations. JIRAM can perform multiple science observations simultaneously; however not all the scientific objectives do overlap and in certain case it is necessary to decide which goal has the precedence, in order to optimize the operational mode and the exposure time, as well as the trajectory characteristics. In particular, for each orbit the target areas to observe are identified and for each acquisition the tilt angle to ensure the best coverage possible of the targets is commanded. The tilt angle is defined as the angle between the nadir vector (from the spacecraft to centre of the planet) and the pointing vector (from the spacecraft to the target), where this angle is positive in the sense of Juno's rotations, and it is always on a plane perpendicular to Juno spin axis [Noschese et al. (2019)]. The possible settings are, then:

- 0° *tilt* → images acquired with nadir pointing.
- *Fixed tilt* → images acquired fixing the mirror at a certain angle with respect to nadir point.
- *Variable tilt* → this mode allows an extended coverage of the targets and it is the one used to scan the polar and auroras areas.

Another important aspect to consider is Jupiter's background radiation, which can create noise in the detector; however, within the temporal and the radiation constrains, JIRAM is able to make auroral and atmospheric measurements under nadir, off nadir and at limb.

4.3 JIRAM Data

4.3.1 JIRAM observation modes

JIRAM instrument can operate in two different modes: the science mode (SCI), that is the only mode in which the acquisition of science data is possible, and the calibration mode (CAL) mode, that allows to perform the calibration sequence. When JIRAM is in the SCI mode it does perform a science observation sequence, whose modalities are determined by the setting of a number of adjustable parameters. The principal tasks are:

i. The evaluation of nadir acquisition time from the spacecraft dynamics
ii. Instrument commanding
iii. Command of the de-spinning mirror motor
iv. Data pre-processing
v. Data compression
vi. Data packing
vii. Data transmission to the spacecraft

The SCI mode is composed of several sub-modes, including both the imager and the spectrometer acquisitions (Tab 4.1), which can be selected to combine the capability of the two detectors (the first for images and the second for spectra).

	Frame size (pixels)	Uncompressed data volume (Mbits)	Compression factor	Compressed data volume (Mbits)
Imaging modes				
I0, No Imager	–	–	–	–
I1, Full Imager	256 × 432	1.8	6	0.3
I2, M-Band	128 × 432	0.9	6	0.15
I3, L-Band	128 × 432	0.9	6	0.15
Spectral modes				
S0, No Spectrometer	–	–	–	–
S1, High Spatial/High Spectral	256 × 336	1.4	1.5	0.93
S2, Medium Spatial/High Spectral	64 × 336	0.35	1.5	0.23
S3, Low Spatial/High Spectral	16 × 336	0.09	1.5	0.06

Tab 4.1 Imager and spectrometer operational modes description. [Adriani et al., 2014]

4.3.2 JIRAM Data Format

JIRAM data are formatted according to the *NASA Planetary Data System (PDS) Data Standards Reference*, and two levels of processing are expected [Adriani et al. (2014)]:

1. **Level 1b → EDR** (Experiment Data Record): telemetry data are cleaned, merged and time ordered according to the instrument modes; therefore, these data are in a scientifically useful form, but still uncalibrated. Each EDR Data Product consists in three files: the Science Telemetry File (binary file containing the scientific telemetry of the instrument), a binary file containing the housekeeping telemetry of the product and a detached ASCII label file, describing the content of the data product.

2. **Level 2 → RDR** (Reduced Data Records): EDR are calibrated and corrected to yield data in scientific units. The RDR Data Product consists of a file containing a PDS binary TABLE-object for the spectrometer and a binary IMAGE-object for the imager, both having a detached label describing their structure, where the geometric references for the imager/spectrometer are referred to the centre of the pixel

4.4 Major findings from JIRAM measurements

Thanks to the unique orbital design of the NASA/Juno mission, the JIRAM instrument has provided unprecedented views of the Jovian polar regions, unlike any images that previous missions and Earth-bound telescopes have ever offered. This new insight into the aurorae and the atmospheric structure, composition, and dynamic of the planet has led to some important and surprising discoveries, such as the polar cyclones, the aurorae's morphology, and the footprints' spot structures and split tail.

1. *Polar cyclones*

   Since the arrival of Juno at Jupiter in July 2016, the M band imager has been providing stunning images of clusters of cyclonic storms, organized into regular pattern and located directly over each pole [Adriani et al. (2018)]. At the north pole, mosaic maps from the JIRAM M-filter observations have revealed the presence of a central cyclone surrounded by eight circumpolar cyclones with diameters ranging from 4000 km to 4600 km. Analogously, a cyclonic pattern characterized by a central cyclone has been observed over the south pole, here encompassed by five cyclones ranging

from 5600 km to 7000 km in diameter arranged like a pentagon (Fig 4.8, *left*). These storms have also appeared to rotate all in the same direction, with an average wind speed of 360 kph and so densely packed that their spiral arms touch each other. After several years of Juno flybys, it is now known that these cyclones are pretty persistent: adjacent storms remain distinct and do not merge for a long time. In fact, on the 22nd flyby of Juno, on November 3, 2019, a new cyclone has been discovered at the south pole, turning the apparently stable southern formation from a pentagon to a hexagon (Fig 4.8, *right*). Therefore, these results have brought to light some unique processes occurring on Jupiter, which were not known before the NASA/Juno mission and that had been never observed neither on the other gas giants or on Earth.

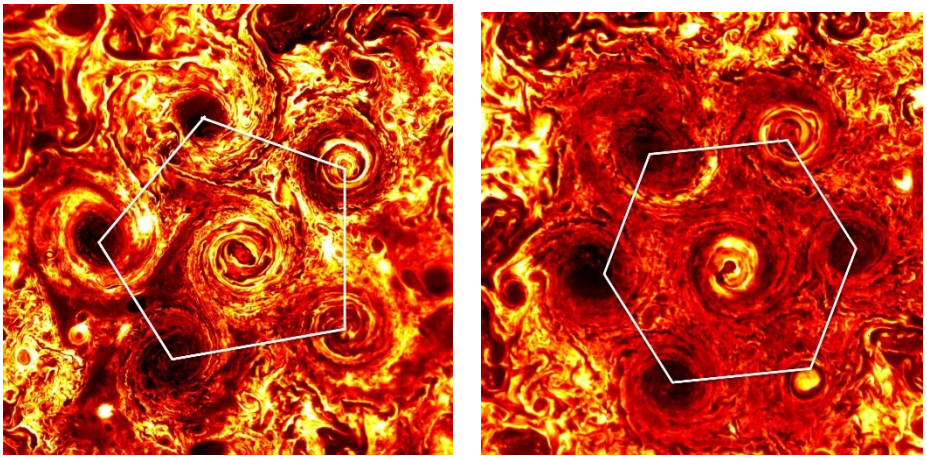

Fig 4.8 (*left*) Infrared image showing the six cyclones at Jupiter's south pole. This map has been generated from the JIRAM measurements of the heat radiated from the planet at an infrared wavelength of around 5μm, collected on February 2, 2017, during the 3rd science pass of Juno spacecraft. (*right*) Infrared image generated from data collected by the Juno/JIRAM imager on November 3, 2019. The mosaic map shows six cyclones arranged in a hexagonal pattern around a central cyclone at Jupiter's south pole. [NASA/JPL-Caltech/SwRI/ASI/INAF/JIRAM]

2. *Aurorae's morphology*

The unique vantage point of Juno, right above the poles, provides the complete views of the Jupiter's aurorae, including the night side emissions [Bonfond et al. (2017)]. The aurorae have been simultaneously observed both in the UV and in the IR by JIRAM and, on a global scale, the Jovian auroral morphology appears very similar in the two domains. Although the global structure of the infrared auroral emissions appears so similar to the ultraviolet, the different excitation processes between the two (one caused by chemical reactions, while the other direct) and the role played by methane create significative differences in the intensity distribution. Also, the infrared view offers an unpreceded spatial resolution, approximately ten times higher than the ultraviolet.

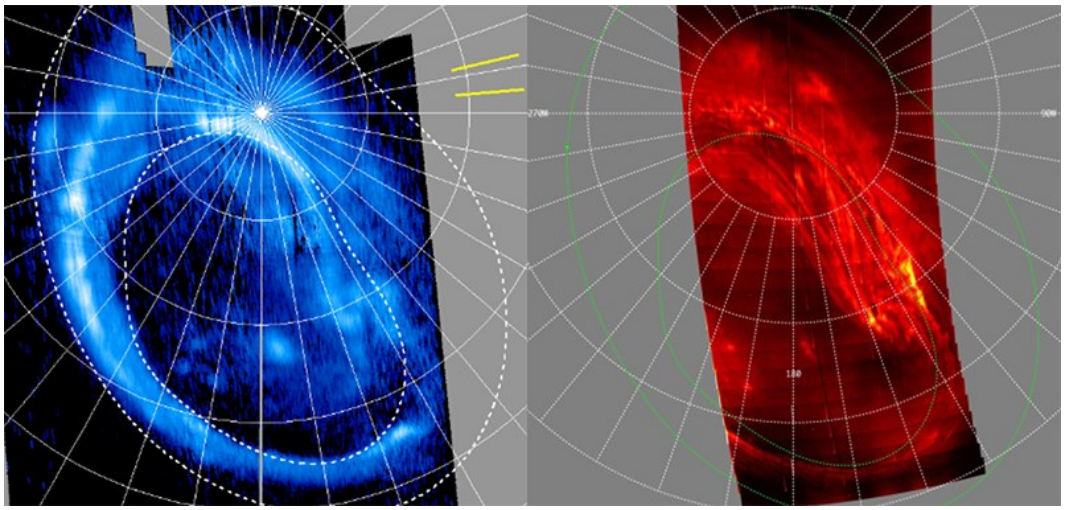

Fig 4.9 Images of the northern aurora observed by Juno in the ultraviolet (*left*) and infrared (red). [Gérard et al., 2017]

The morphology of Jupiter's aurorae is commonly divided into three main components:

- the main oval → Both the southern and northern main ovals, which can be observed in Fig 4.2 and Fig 4.9 respectively, show a narrow single arc in about one half of the oval and multiple arcs plus broad diffuse emissions in the other half [Mura et al. (2017)]. However, in the IR multiple structures of coherent pattern can be observed in both the hemispheres in the diffuse region.
- the polar emission → Inside the main oval infrared emission can be observed everywhere, which may partly be caused by insufficient background subtraction. Also, bright spots can be detected in the polar emissions, probably linked to plasma injections. [Gérard et al. (2017)].
- the outer emission → Both the hemispheres show intense outer emissions equatorward the main emission. Here, the footprints of Io, Europa and Ganymede can also be detected.

3. *Footprints' spot structures and split tail*

   JIRAM's infrared observations have revealed that the Io's footprint appears as regularly spaced array of emission features, which exhibit a swirling pattern similar to a von Kármán vortex street (Fig 4.10). Because of their small scale (100 km), these traits cannot be caused by multiple reflected Alfvén waves reflections, which instead explain the large-scale multiplicity already observed. Moreover, JIRAM measurements have shown that well downstream of the main auroral spots Io's trailing tail is split in two, showing a pair of closely space arcs [Mura et al. (2018)].

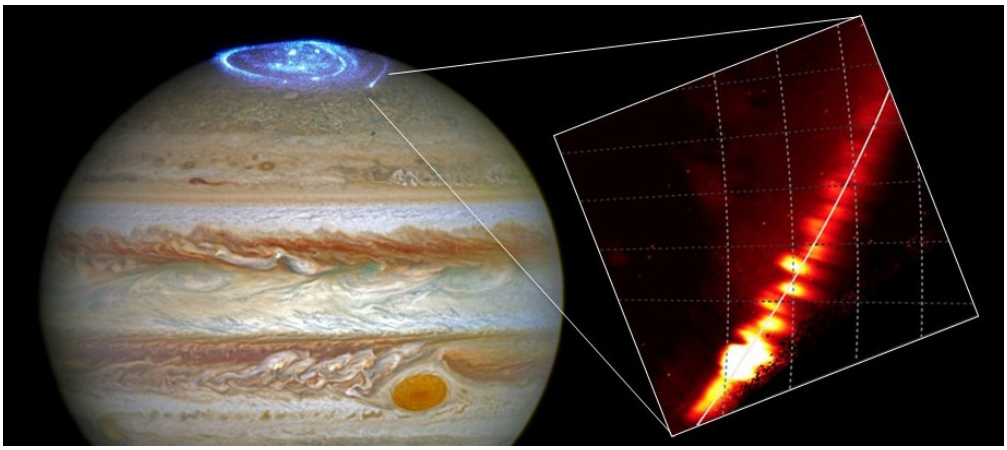

Fig 4.10 (*left*) Illustration of Jupiter's aurora and Io's footprint on the planet as seen by the Hubble Space Telescope. (*right*) The insert shows the footprint of Jupiter's moon Io as seen by the JIRAM camera on board the Juno probe. [NASA/HST/A. Mura/INAF-IAPS]

Analogously, Ganymede's footprint has a dual fine structure (Fig 4.11) and appears as a pair of emission features very close to each other (~100 km): the main component and the secondary one. Again, the tail extending from the main auroral spots eventually separate in two. The cause of this split is unsure; however, being Ganymede the only Jovian moon with its own magnetic field, this phenomenon might be caused by the interaction between Ganymede and Jupiter's magnetic field.

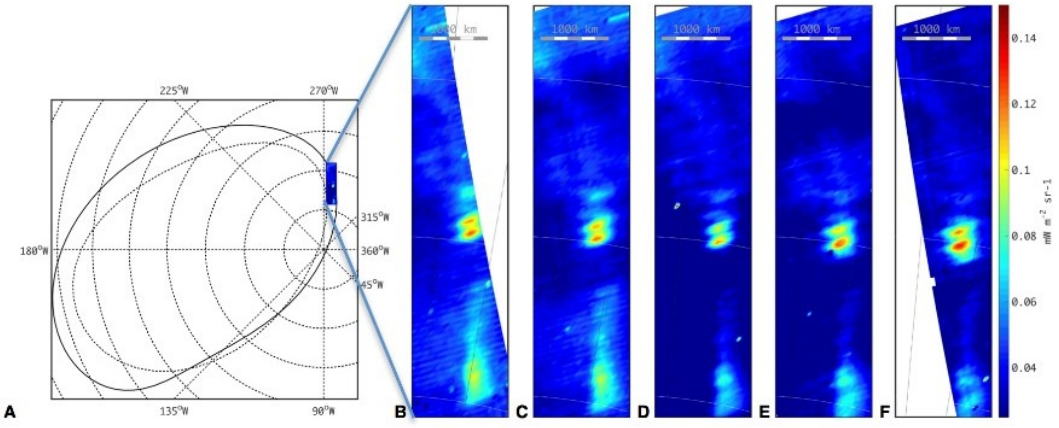

Fig 4.11 (*left*) Diagram showing the main oval (dotted line) and the Ganymede's footprint (solid line) predicted from the recent magnetic field model (*right*) Five consecutive images of Ganymede footprints. The insert shows the footprint of Jupiter's moon Io as seen by the JIRAM camera on board the Juno probe. [Mura et al. (2018)]

The discovery of such features suggests that the magnetohydrodynamic interaction between the planet and its moons is more complex than thought and, therefore, that the recent magnetic field model has to be revised.

5. Analysis of H_3^+ and CH_4 in Jupiter's auroral regions

This Chapter focuses on the data analysis that has been performed for the study of Jupiter's aurorae through the inversion of JIRAM measurements and on the discussion of the final results.
Starting from the selection of few Juno's orbits considered to be appropriate for the target of this thesis, several criteria have been used to retain only the most promising spectra among all those acquired by JIRAM during each of these orbits. All the selected measurements have been then analysed individually, using the retrieval method described by *Dinelli et al.* (2017) to retrieve from the observed spectra the effective temperature and the column density along the LOS of the instrument of the emitting species in Jupiter's auroral regions, as well as some instrumental parameters for also considering problems related to the spectral calibration. After a preliminary run of the retrieval code to determine the better a-priori estimate of the retrieval state vector, it has been decided to fix the temperature of methane at 600 K and the wavelength shift at a value computed through a second-order polynomial function that well reproduces the relation between the wavelength calibration and the position of the pixel on the slit where the measurement is done. Therefore, the free parameters of the retrieval have been reduced to the H_3^+ column density and effective temperature and the CH_4 concentration. Successively, the final run has been performed and several filters have been applied to retain only the most robust retrievals. With the purpose to identify patterns and regularities, these final results have been then represented as distribution maps, obtained by dividing the area of an orthographic map into bins and averaging all the retrievals and associated errors inside each bin. As a conclusion of this thesis, these maps have been compared with the images obtained from JIRAM observations using the L-band for each of the analysed orbits, to study the aurorae's morphology and identify variation over time of the auroral main oval.

5.1 Data selection

This thesis is an extension of the work done by *Dinelli et al.* (2017), *Aldriani et al.* (2017), and *Moriconi et al.* (2017), who analysed JIRAM measurements acquired in nadir geometry over the polar regions during the first Juno's orbit (JM0003), providing preliminary results on H_3^+ and methane emissions in Jupiter's auroral regions. In the present study, a larger number of spectra collected by

JIRAM over Jupiter's north and south pole during orbit JM0003 has been investigated and a more detailed analysis on both H_3^+ and CH_4 emissions has been performed. Moreover, numerous measurements collected outside the auroral regions have been included in the retrieval to determine the background status of the two molecules and use this information as a baseline to process data from successive orbits, which, exhibit weaker auroral signals, due to either the intrinsic auroral variability or to the deterioration of the JIRAM detectors. Therefore, along with the JM0003/JIRAM observations, spectra from the JM0041-JM0091 orbits have been also investigated, retaining only those where JIRAM achieved a good coverage of the auroral regions. Then the most promising spectra have been extracted from all those available and the resulting datasets have been analysed by using an upgraded version of the retrieval code described by *Dinelli et al.* (2017) to determine temperatures and column densities of H_3^+ and CH_4.

5.1.1 Orbits selection

In this thesis, Juno's orbits from JM0003 to JM0091 have been examined to select those where JIRAM's orientation appeared favourable for the study of Jovian auroral phenomena. Apart from orbits JM001, JM002 and JM003, where JIRAM was turned off because of instrumental problems, all the other orbits had the JIRAM instrument operating with good performances. The first step has been to examine all the data and discard the data sequences whose principal targets were not Jupiter's aurorae. With this purpose, all the spectral data sets and geometrical files relative to these orbits have been downloaded and, successively, mosaicked to determine the coverage of the auroral regions achieved by the instrument (for more details see section 4.4.2). These operations have been performed for each orbit, both for the north and south poles, by projecting the IFOVs on an orthographic map in planetocentric coordinates referred to a surface located at 500 km above 1 bar level. Moreover, for preliminary assessment of emissions distribution and intensity over this map, a simple depiction of red-green-blue (RGB) color space has been used, where R = 3.540 μm, G= 3.423 μm, and B = 3.315 μm. Figure 4.1 displays all the projections centred at the north pole (latitude of 90°), and at the south pole(latitude -90°) with a latitude radius of 40° (ranging from 50 to 90 or -50 to -90)north with the dashed lines indicating a latitudinal delta set of 10° and a longitudinal delta of 45°. The 0 longitude is plotted at the top of each map for the north pole and at the bottom for the south pole. Also, to better locate Jupiter's aurorae, two oval shaped curves have been superposed to the projection, where the solid line indicates the position of the UV statistical auroral oval given by Hubble Space Telescope

observations [Groedent et al. (2003)], while the dashed curve represents the position of the oval predicted by the VIP4 model [Connery (1998)].

The final mosaics provide an overall view of the spectral observations of Jupiter's auroral regions and have been used to select the most promising orbits for the retrieval of temperatures and column densities of H_3^+ and CH_4, apart from the already well known JM0003. The projection of the IFOVs gives an immediate idea of the coverage of the planet by JIRAM, as well as the distance from the surface at which the data have been acquired: when the spectrometer collects spectra at larger distances from the surface, its footprint covers a larger area, resulting in a bigger IFOV, hence a wider slit; while, if closer to the surface, the slit appears shorter. Instead, the wavelength color composition (RGB maps) has been used with the purpose to enhance the presence and the distribution of the auroral-emitting species: blue corresponds to the JIRAM channel where methane emission occurs, while red and green are associated to other two channels where only H_3^+ auroral peaks are present. Therefore, relaying on the maps in Fig 5.1 a, b, c, and d, the following evaluations have been made:

- **JM0003** offers an ideal coverage of Jupiter's higher latitudes, providing a large number of spectra to study the aurorae, as well as an extensive set of data to investigate the background signal. As it can be noticed in Fig 5.1a from the RGB map, the presence of methane appears distinctly both in the north and south pole, since CH_4 Q branch shares with H_3^+ auroral emission the JIRAM channel at 3.315 μm and in presence of methane fluorescence and faint H_3^+ emission, the methane signal do prevail the auroral one [Moriconi et al. (2017)]. Moreover, this map shows clearly the main oval emissions, which, being all the three bands equally intense, appear white.

North Pole		South Pole	
IFOV	**RGB**	**IFOV**	**RGB**
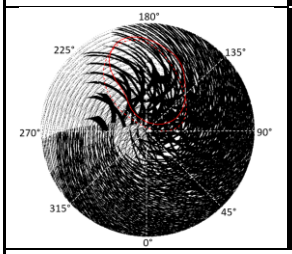	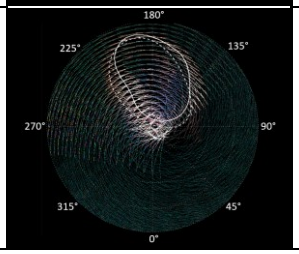	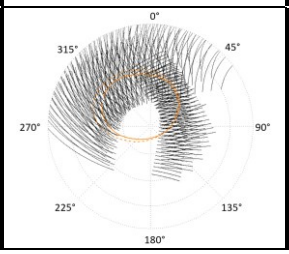	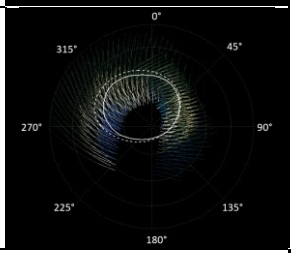

Tab 5.1a Projection of JIRAM data on an orthographic map for Juno's orbit JM0003.

- **JM0041** provides a good coverage of both the auroral regions (Fig 5.1b); however, the auroral signal appears less intense than the previous orbit and the methane is not as visible as for JM0003.

North Pole		South Pole	
IFOV	**RGB**	**IFOV**	**RGB**
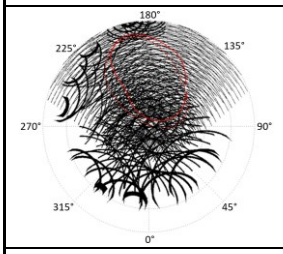	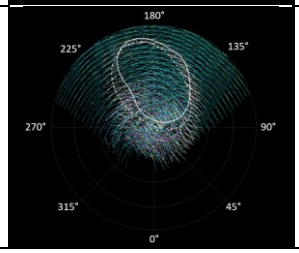	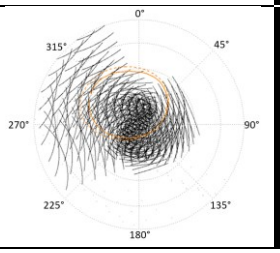	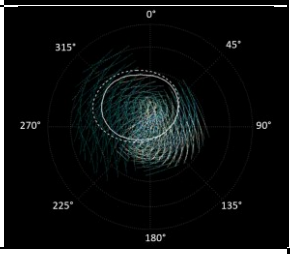

Tab 5.1b Projection of JIRAM data on an orthographic map for Juno's orbit JM0041.

- Looking at orbits **JM0051** and **JM0061** in Fig 5.1c, it can be immediately noticed that only few spectra lie in Jupiter's auroral regions; therefore, these orbits have been excluded from the analysis.

North Pole		South Pole	
IFOV	**RGB**	**IFOV**	**RGB**
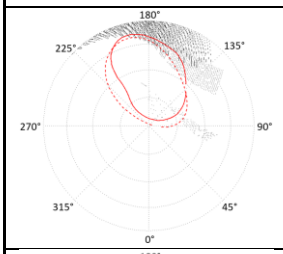	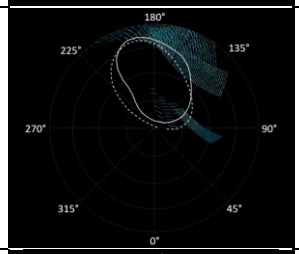	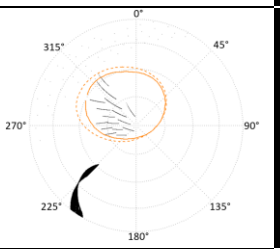	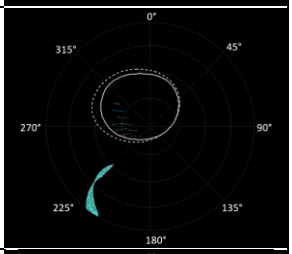
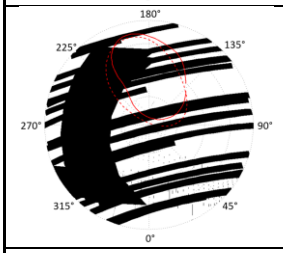	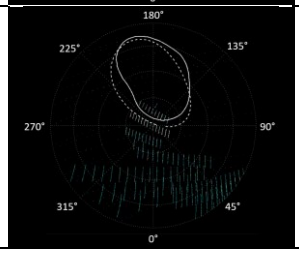	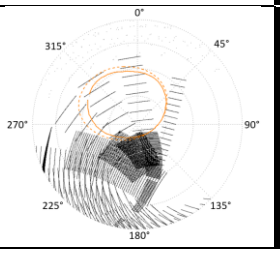	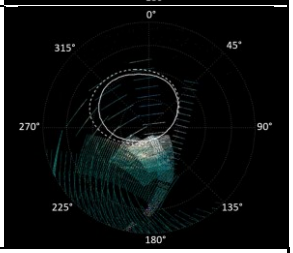

Tab 5.1c Projection of JIRAM data on orthographic map for Juno's orbits JM0051 (*top*) and JM0061 (*bottom*).

- As it can be noticed from Fig 5.1d, while the coverage of Jupiter's north pole is quite low for orbit **JM0071** and **JM0081**, the spectra collected by JIRAM over Jupiter's south pole appears relevant, exhibiting, along with a great coverage, quite intense auroral emissions and the presence of methane near the pole. Therefore, for these two orbits only the southern aurora has been investigated.

North Pole		South Pole	
IFOV	RGB	IFOV	RGB
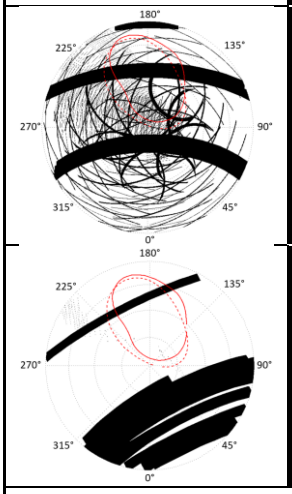	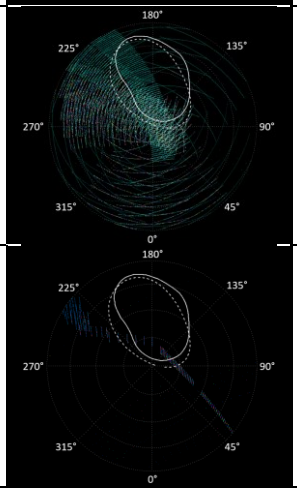	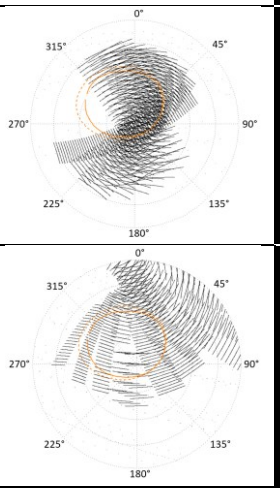	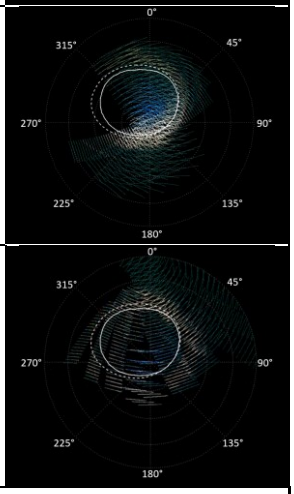

Tab 5.1d Projection of JIRAM data on orthographic map for Juno's orbits JM0071 (*top*) and JM0081 (*bottom*).

- Finally, orbit **JM0091** has been excluded from this analysis, being the coverage over the south pole quite poor and the northern auroral signal rather weak and noisy (Fig 5.1e).

North Pole		South Pole	
IFOV	RGB	IFOV	RGB
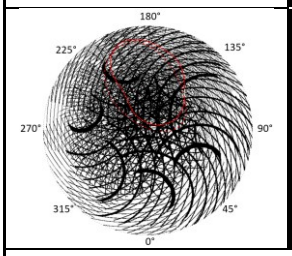	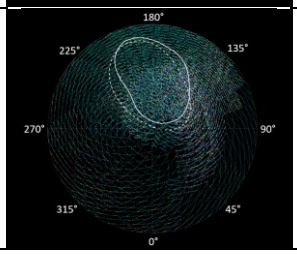	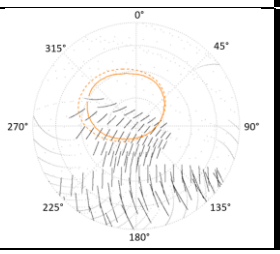	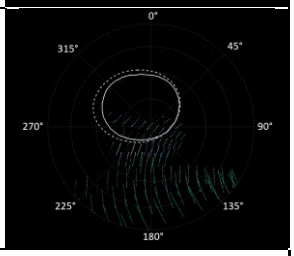

Tab 5.1e Projection of JIRAM data on an orthographic map for Juno's orbit JM0091.

Concluding, in this work JIRAM observations of the northern and southern aurorae during orbits JM0003 and JM0041 have been considered, while for orbits JM0071 and JM0081 the focus has been posed only on the data acquired by the instrument over the south pole. Once determined the orbits which best fit the purpose of this thesis, a dataset has been created for each of them by selecting JIRAM observations according to appropriate criteria, described in next section.

5.1.2 Spectra selection

Before the actual data selection process, the spectral region of interest has been defined. As already seen, JIRAM covers the 2-5 μm spectral interval, sampling each spectrum in 336 channels; however, because wavelengths below 3.2 μm can be affected by solar scattering from the deep atmosphere and because the auroral signal can also be influenced by solar scattering and thermal emissions from the lower atmosphere at wavelength larger than 4 μm, these spectral regions have not been considered. Moreover, by looking at a typical JIRAM spectrum, as the one shown in Fig 5.2, it can be noticed a feature at 3.8 μm, which is associated to an instrumental effect. Since the H_3^+ signal above 3.8 μm is negligible, the wavelength interval used in this analysis is the 3.2060-3.772 μm region.

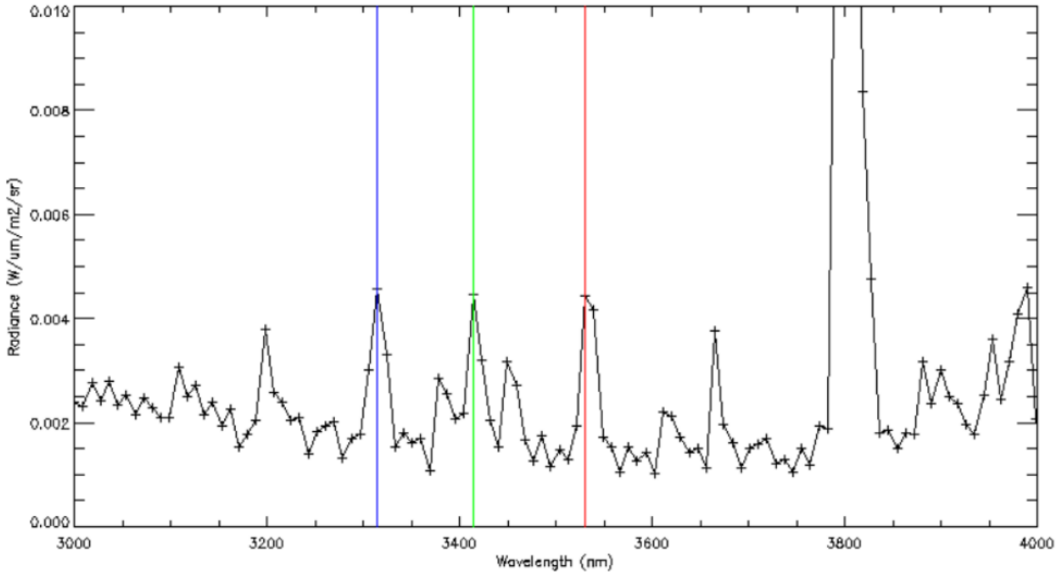

Fig 5.2 JM0003/JIRAM sample spectra in the region 3-4 μm. The blue line marks the wavelength at which methane emission peaks, while red and green lines corresponds to two H_3^+ auroral peaks.

As briefly reported earlier, in order to perform the analysis, the spectral data (provided already calibrated and in nanometer scale) and the geometrical information relative to the selected orbits have been downloaded and merged. In particular, the geometrical files have been generated through an ad hoc algorithm, based on the NAIF-SPICE tool, for each image of the spectrometer and imager channel, referred to a surface located at 500 km over Jupiter's surface level. This procedure, already used in the analyses of JIRAM measurements reported in *Dinelli et al.*, *Adriani et al.*, *Moriconi et al.*, is due to the fact that the 500 km surface is expected to be closer to the real altitude where the main H_3^+ emission occurs. Therefore, in case of slant observations (with large emission angles) the parallax

error in assigning the latitude and longitude of the auroral emissions is reduced. Therefore, each pixel is plotted on a stereographic map located at 500 km above the 1 bar level, where the LOS (line of sight) of the measurement intercepts this surface. However, depending on JIRAM's different time of acquisition and distance from the planet, the emission angle, defined as the angle between LOS and the normal to the 500 km surface, can assume several values and affect the pixel size: the larger is the emission angle the wider is the pixel projection on the map. On top of this, the projection on the 500 km altitude surface of the atmospheric column crossed by JIRAM LOS, as the emission angle increases, covers larger and larger paths, that, given the spatial variability of the auroral regions, may mask out interesting auroral features. Therefore, to prevent errors in interpreting the results by averaging measurements referring to larger regions, and to avoid the geometrical smearing of the observed features, only spectra with an emission angle smaller than 75° have been retained in the analyses.

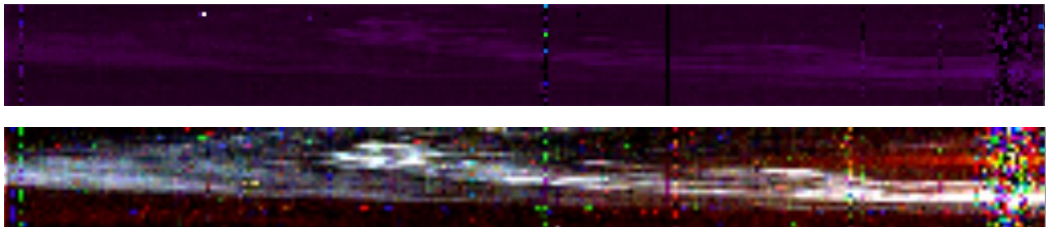

Fig 5.3 (*top*) JIRAM observation session, from which spectrum shown in Fig 5.2 has been extracted. (*bottom*) The same observation session displayed on the top panel after the removal of the continuum signal, resulting from the scattering of sunlight by atmospheric gas, and the correction for the odd-even effect, visualized in RGB color. Blue is associated with methane emission, red and greed with H_3^+ auroral emission. White areas represent locations where all the three signals are strong.

Spectra have also been filtered in terms of radiance to remove the most evident spikes, as the one visible in Fig 5.3. The figure in the *top panel* shows the JIRAM's observation section from which the spectrum in Fig 5.2 has been extracted. Each observative section is characterized *n* samples, namely the number of pixel on the slit (256 pixels) and *m* lines, where each line represents one slit acquisition. Therefore, as already mentioned in 4.4.2, JIRAM spectral datasets have three dimensions: two spatial dimensions (X-Y, one along the slit and one across the slit, along the observational track) and one spectral dimension (λ, provided by the grating). JIRAM thus provides hyperspectral images in the

wavelength range 2-5 μm, which also means that the user can extract a spectrum in the given wavelengths range from each pixel of the image. Hyperspectral images can also be visualized by means RGB maps at specific wavelengths, as the image in the *bottom panel* of Fig 5.3, which represents the same acquisition section shown in the *top panel*, however after the removal of the continuum signal resulting from the scattering of sunlight by atmospheric gas and the correction of the odd-even effect [see section 5.2]. This processed image facilitates the detection of the auroral oval, but also highlights the presence of spikes. As a matter of fact, when the detector intercepts energetic particles one or more spikes can affect the measured spectrum, creating characteristic features such as the red, green, and blue dots and/or swipes visible in the RGB image shown in Fig. 5.3 *bottom*, which have to be removed. While the noise at the extremities of the slit is attributable to the detector and the relative spectra can be easily discarded by excluding the first and last pixels of the slit from the analyses, for the removal of the other spikes a simple procedure has been applied: all the spectral points with an intensity larger than 0.006 $W/m^2\,\mu m\,sr$ have been flagged as spikes and therefore removed from the analysis. Because the auroral emissions can be seen as spikes with respect to the background signal, the radiance threshold has been chosen high enough to avoid the H_3^+ lines to be masked out from the retrieval, but sufficiently low for the most evident spikes to be discarded. Lastly, radiance filters have been used to create the final datasets. In fact, depending on the intensity of the signals, JIRAM measurements can be separated into two populations. This can be noticed in Fig 5.4, where the normalized histograms (obtained by considering the three above-mentioned RGB channels of orbit JM0003), representing the observed radiances distribution, exhibit two distinct peaks: one centred at lower radiances, and a second one shifted toward higher values. By selecting data around the first peak, a large number of spectra outside the auroral oval, hence associated with the background population, can be extracted (*top panel*); instead, when considering radiances larger than a certain threshold value, the auroral emissions, mixed with those of methane, can be detected and analysed (*bottom panel*). However, it has to be said that such a clear separation between the two populations has not been spotted in the other orbits, because weaker auroral emissions mingle with the background signal, making this discrimination less straightforward.

In this thesis, spectra from both the background and auroral regions have been selected to retrieve, along with H_3^+ temperature, column densities and methane concentration within the main oval, the temperature of H_3^+ outside the emissions oval. A summary of the number of JIRAM observations extrapolated from the background and from the auroral region, as well as the total number of spectra to which the retrieval code has been applied, is presented in Tab 5.1.

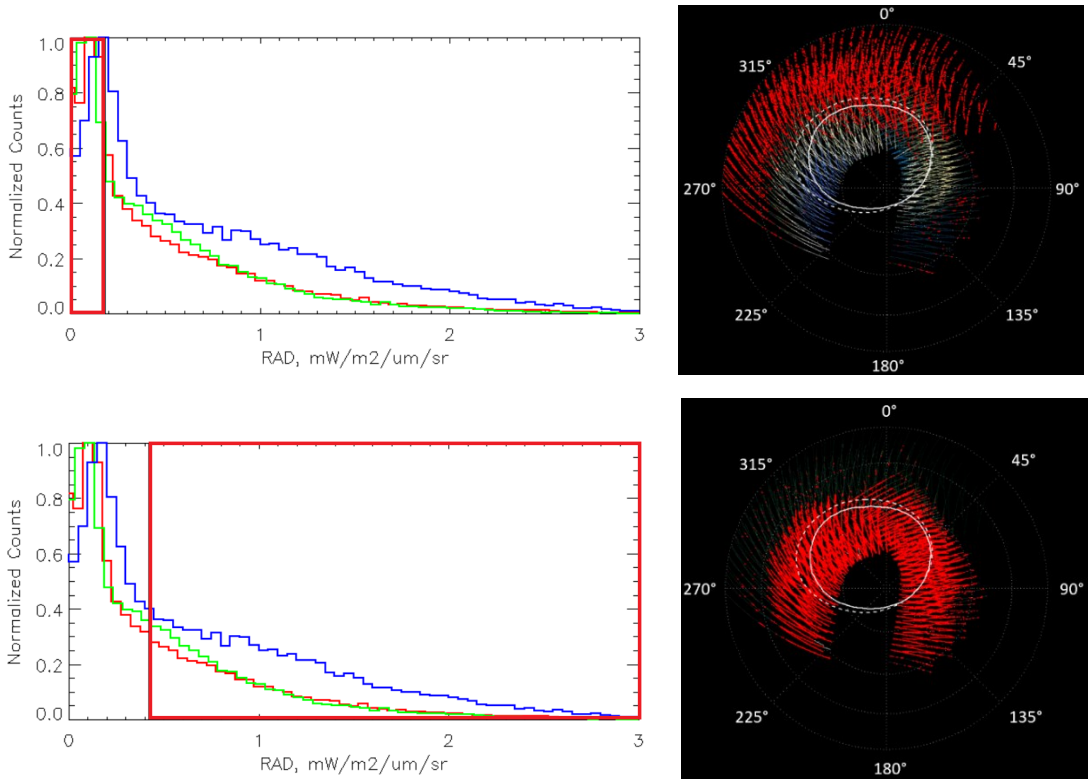

Fig 5.4 Representation of the background (*top panel*) and auroral (*bottom panel*) populations of the JM0003/JIRAM measurements over Jupiter's southern pole. The two classes of data are marked in red in the normalized radiance histograms and the corresponding spectra are projected as red dots on an orthographic map.

NORTH POLE

Orbit	*Background spectra*	*Aurora spectra*	*Total n° of spectra*
JM0003	21182	10518	31700
JM0041	7528	6678	14206
JM0071	/	/	/
JM0081	/	/	/

SOUTH POLE

Orbit	*Background spectra*	*Aurora spectra*	*Total n° of spectra*
JM0003	7445	18805	26250
JM0041	2427	14753	17180
JM0071	6700	11762	18462
JM0081	3656	9887	13543

Tab 5.1 (*top*)Table showing the number of spectra selected in the background and auroral regions in Jupiter's north pole and the total number of selections from each orbit. (*bottom*) Data selected from JIRAM observations over the south pole.

5.2 Odd-Even correction

Array detectors like the ones used by JIRAM, allow many spectral channels to be recorded simultaneously. However, to enhance JIRAM spectral resolution, the final spectra, a sequence of contiguous spectral points, are in reality measured into two steps: first the odd-numbered grid points of the spectrum are measured and, immediately afterward, the array is shifted to acquire the even-numbered points; all of them are then merged to produce the final spectrum. Even if this strategy produces a difference between odd and even points below the instrumental noise level, if the complete spectra are averaged, reducing therefore the measurement noise (a random quantity), the final spectrum is affected by a sawtooth signal that cannot be removed just with the averaging procedure. This effect is called 'odd-even effect'. In order to preserve as much information as possible, JIRAM observations have therefore been corrected for the odd-even effect. The correction is performed by considering the odd- and even-numbered spectral points separately: all the odd points and the even points are separately interpolated with a spline on the spectral grid of the original spectrum. Then, the two resulting spectra are averaged to produce the final spectrum. All the spectra analysed in this thesis have been corrected for the odd-even effect. An example of spectrum before and after the odd-even correction is reported in Fig 5.5.

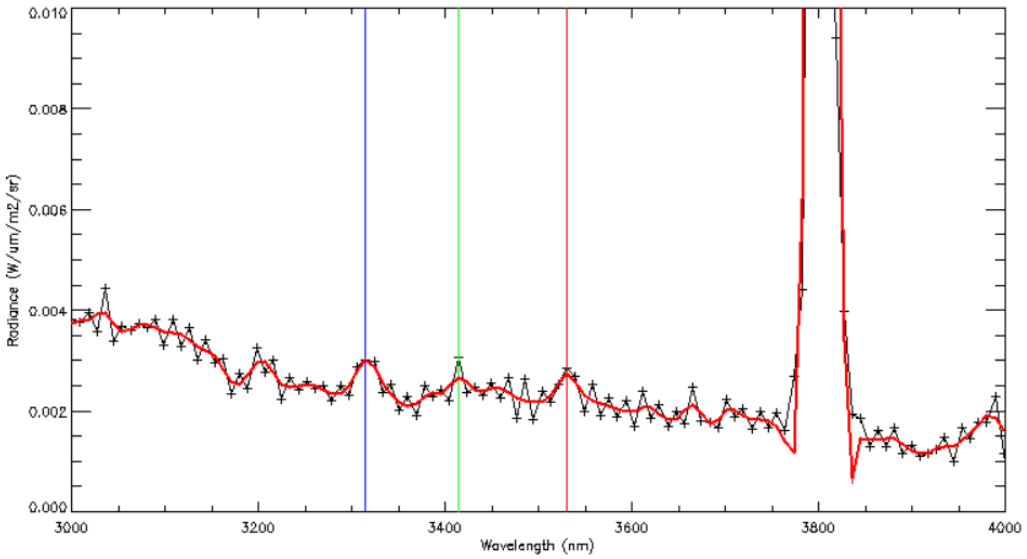

Fig 5.5 JM0003/JIRAM sample spectra in the region 3-4 μm showing a not particularly intense auroral signal. The black line is the original spectrum, where the plus signs mark the spectral points. The red line represents the spectrum after the odd-even correction.

5.3 Retrieval Code

In this study, to retrieve temperature and column density of methane and H_3^+ the retrieval code described in *Dinelli et al.* (2017) has been used. The code consists in an updated version of that developed by *Altieri et al.* (2016) to analyse Galileo/NIMS measurements and is characterized by two modules:

1. The *Forward Model* (FM), that simulates the spectrum by assuming

   - the H_3^+ emissions of the auroral region to be optically thin; this hypothesis is based on ground observations according to which the emitting molecules are all located in the highest Jovian atmospheric layers;
   - the pressure broadening of the spectral lines can be neglected either because the linewidth is much smaller than the resolution of the instrument and because the re-absorption of emitted radiation is not considered;
   - that the emitting gas is located in a single emission layer at a certain effective temperature T_m; therefore, because the majority of auroral emissions originate at altitude where vibrational LTE $(\text{or Quasi-Thermal Equilibrium})$ can be satisfied, a single temperature can be used for all the molecular transitions, resulting in a maximum error of 5% in the simulated radiance $[\text{Dinelli et al. } (2017)]$.

   Moreover, assuming that a single column density might be used for each of the molecules under analysis, the radiation emitted by transition *i* of molecule *m* can be obtained applying the formula $[\text{Altieri et al. } (2016)]$:

$$I_{im} = N_m(2J_{im} + 1)\, g_{im} A_{im} hc\nu_{im}\, \frac{e^{-\left(\frac{hcE_{im}}{KT_m}\right)}}{4\pi Q_m(T_m)} \tag{5.1}$$

   where

   - I_{im} represents the intensity of the *im* transition,
   - N_m denotes the column density $[mol/cm^2]$ along the line of sight of the emitting molecule *m,*
   - T_m is the effective temperature of the molecule $[\mathrm{K}]$,
   - J_{im} is the rotational quantum number of the upper level of the considered transition,
   - ν_{im} is the wavenumber $[cm^{-1}]$ of the transition *i,*
   - g_{im} is the nuclear spin weight,

- A_{im} is the Einstein coefficient for spontaneous emission,
- E_{im} is the energy of the upper level of the considered transition,
- $Q_m(T_m)$ represents the partition function at temperature T_m.

The high-resolution simulated spectra are, hence, obtained by computing the intensity of each transition of the considered gases. Successively, the line-by-line intensities are convolved with the instrumental spectral response function, which is assumed to be a Gaussian function (with a width determined during an on-ground calibration campaign), to reproduce the measured radiation. The odd-even correction is then applied to the simulated measurements.

2. The *Retrieval Module* (RM), that performs the fit of the observed spectra and exploits the Bayesian inversion strategy to retrieve from the observed spectra the effective temperature and the column density along the LOS of the instrument for each of the considered molecules. Also, the RM retrieves some instrumental parameters such as the frequency shift, the width of JIRAM's instrumental response function and the radiometric offset, in order to take into account the problems related to spectral calibration. As it is already been said in Chapter 2, the Bayesian approach minimizes the chi-square test function at each iteration and this loop is stopped when the χ^2 values of two consecutive iterations do not change for more than 1%.

5.4 Initial guesses parameters

Each spectrum in the final datasets has been analysed by using the retrieval code just described, where all the measurements have been assumed to be affected by the same noise equivalent spectral radiance of $1.5 \cdot 10^{-7}\ W/m^2\,nm\,sr$ (derived from the analysis of the deep space spectra). The width of each spectral channel has been set to the value of 12 nm, coming from on ground measurements. The retrieval has been performed into two steps. In the first step, the retrieval state vector (the target parameters) was made of the H_3^+ effective temperature (T) and column density (CD), the CH_4 CD, the spectral intensity offset and the wavelength shift. Successively, the results of the first run have been used to fit a second-order polynomial function to the set of the retrieved wavelength shifts as a function of the position of the spectrum on the slit, in order to estimate the real wavelength scale and

fix it in the retrievals. This has been done to avoid that the retrieval of the wavelength shift was used by the retrieval code to compensate other instrumental or spectral effects. The final retrieval state was hence made of the H_3^+ effective temperature (T) and column density (CD) and the CH_4 CD. Tab 5.2 shows the initial guess value and their a-priori error:

- H_3^+ $T_{a-priori}$ = 700 K, with an initial a-priori error of 500 K
- H_3^+ $CD_{a-priori}$ = $1 \cdot 10^{12}$ mol cm^{-2}, with an a-priori error of $5 \cdot 10^{13}$ mol cm^{-2}
- CH_4 $CD_{a-priori}$ = $1 \cdot 10^{12}$ mol cm^{-2}, with an a-priori error of $1 \cdot 10^{15}$ mol cm^{-2}

Where the a-priori error has been chosen to to limit the constrain on the retrieval's outputs.

5.4.1 Determination of the CH_4 effective temperature

In *Dinelli et al.* (2017) and Adriani et al. (2017) the analysis of the JM0003 measurements over the polar regions was performed by keeping the CH_4 effective temperature fixed at 500°K; in *Moriconi et al.* (2017) the spectra simulated by fixing the CH_4 T values from 200 K to 800 K with steps of 150 K fitted to JIRAM spectra averaged where the CH4 signal was the largest, showed that the lowest χ-test had its lowest values for methane's effective temperature of 500 K in the north pole and 650 K in the south pole. However, these preliminary results were performed only on two averaged spectra and the examined spectra were not corrected for the odd-even effect; therefore, in order to determine the most appropriate value for the CH_4 T, a preparatory analysis has been performed on a set of data selected to better investigate methane's column density and effective temperature at Jupiter's south pole. In particular, two collections of spectra have been analysed: one consisting of observations acquired during the first perijove period $(JM0003)$ above the southern pole, while the other including data from the firth perijove period $(JM0041)$ over the same Jovian region, where a diffuse presence of methane was detected. These data have been analysed using the new code, that correctly takes into account for the odd-even effect. Since the H_3^+ signal in these spectra was very weak, for this test the H_3^+ temperature has been fixed to an a-priori value of 700 K, while the H_3^+ CD has been included into the state vector to take into account the weak variability of the H_3^+ signal. The methane temperature has been fitted, along with its column density, starting from an initial value of 600 K and an a-priori error of 200 K. The retrieval outputs have been then individually examined to mask manually the most evident spikes and finally, the results have been compared with those obtained by

running the old code that did not include the odd-even (O-E) correction . As it can be noticed from Fig 5.6 for the first dataset (JM0003/SP), the implementation of the odd-even correction into the fitting program leads to more consistent results with respect to the case where the O-E effect is not considered; in fact, Fig 5.6b exhibits a temperature distribution sharply peaked at 600 K, while the histogram in Fig 5.6a display two different peaks, one at about 570 K and the other around 600 K. A similar result has been also obtained for the second dataset (JM0041/SP), showing a single peak at 570 K.

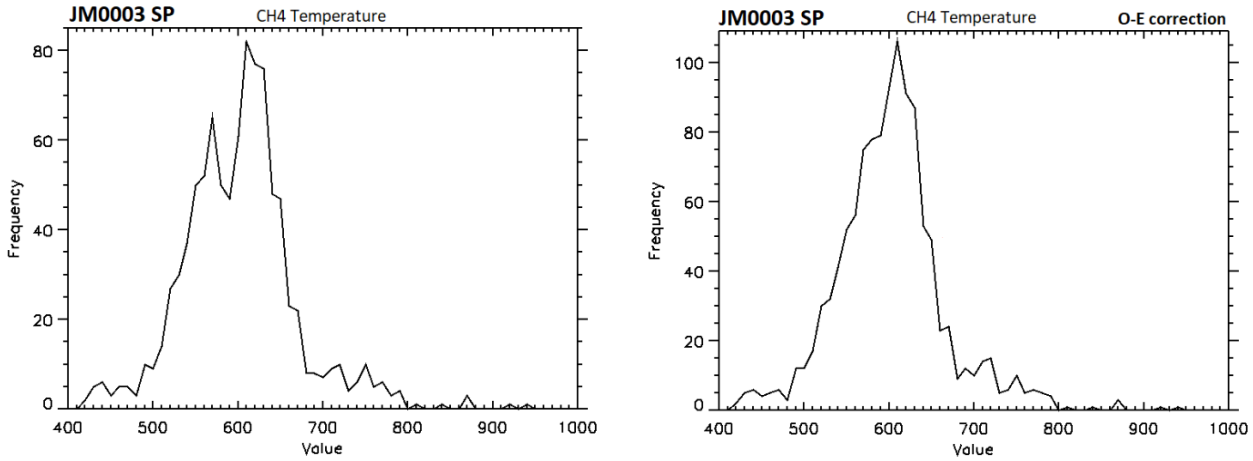

a **b**

Fig 5.6 (a) Histogram of CH_4 effective temperature distribution at Jupiter's south pole during the first perijove period, obtained by running the old retrieval code, hence without the odd-even correction, by fitting the CH_4T with an initial value set at 600 K. Methane's temperature exhibits a double peak: the first at about 570 K and the second around 600 K. **(b)** Methane's temperature distribution where all the simulated spectra are now corrected for the odd-even effect. Here the histogram displays a single peak at 600 K.

Before fixing the CH_4 effective temperature at the value of 600 K to analyse all the datasets selected for this study, a further test has been performed on same two sets of data: to investigate methane's column densities, a second run has been then performed, this one fitting the H_3^+ temperature and fixing the CH_4 T at 600 K. As it can be seen in Fig 5.7 for the JM0003 orbit, but is equally valid for the JM0041, the distribution of the CH_4 CD values do vary considerably after fixing the temperature of methane and appears more consistent with the preliminary results in *Moriconi et al* (2017). On the

basis of these results, it has been decided to conduct the planned analyses keeping the CH_4 T fixed at 600 K. This configuration has been used for the preliminary run used for fixing the value of the frequency shift, in order to prevent the retrieval code to use the frequency shift to partially correct for instrumental problems.

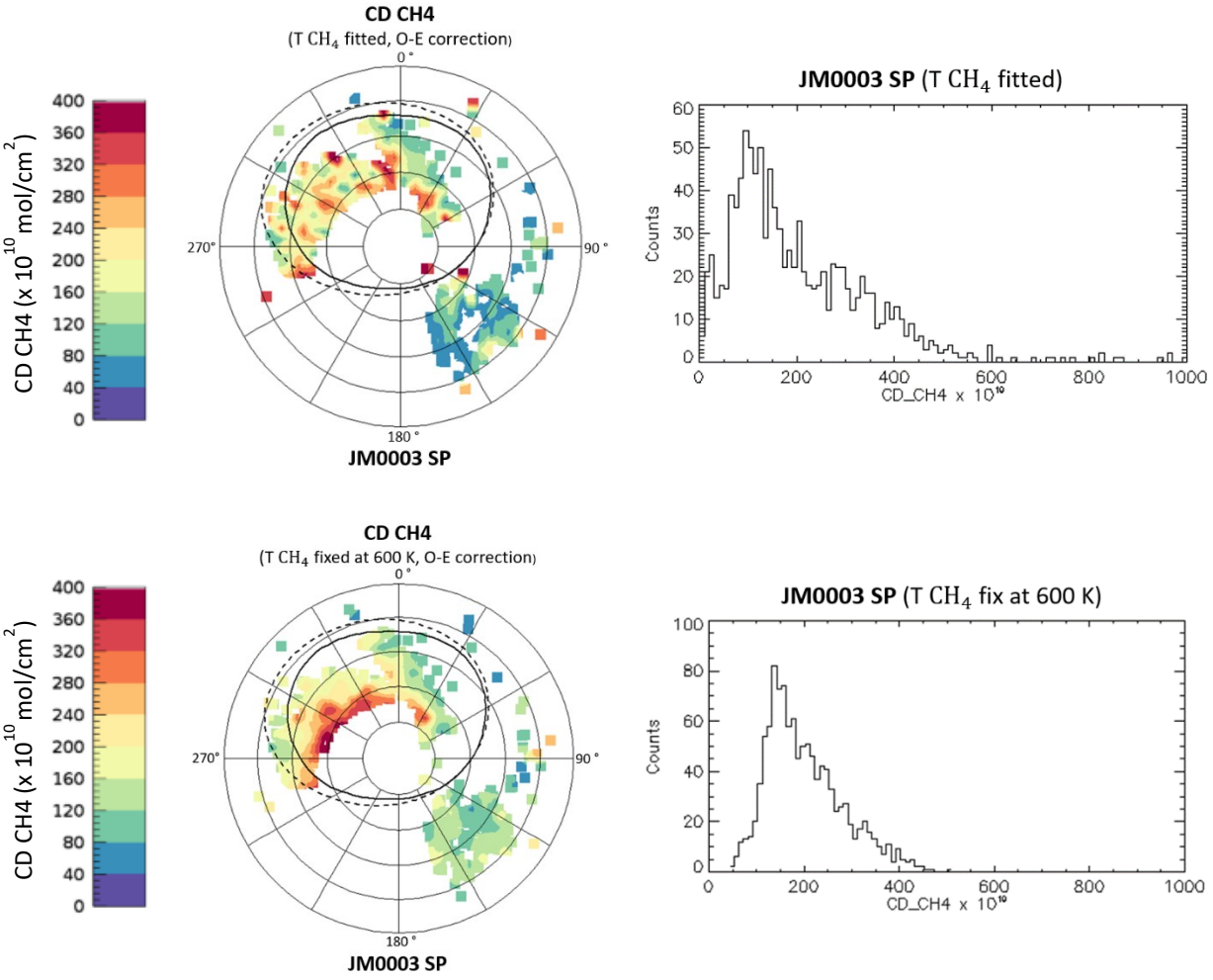

Fig 5.7 (*top*)Distribution map of methane column density over Jupiter's south pole derived from JM0003/JIRAM data when the CH_4 temperature is fitted (with an a-priori value of 600 K) and the corresponding distribution histogram (x-axis in mol/cm^{-2}). Such a map has been obtained by averaging all the CD's values laying in a box which roughly reproduce the JIRAM's IFOV. (b*ottom*) Distribution map for JM0003/JIRAM data selected and the relative distribution histogram (x-axis in mol/cm^{-2}) for the retrieval of methane inside the auroral oval, where the retrieval has been performed keeping T CH_4 fix at 600 K .

5.4.2 Wavelength shift

Since the wavelength calibration of the measured spectra only depends on the position of the pixel on the spectrometer's slit where the measurement is done, in *Dinelli et al.* (2017) a second-order polynomial function was fitted to a set of retrieved wavelength shifts versus the position of the pixel. This polynomial was then implemented in the retrieval code and used to calculate the frequency shift for each pixel on the slit, in order to fix the wavelength shift to the computed values. In this study, it has been verified the viability of this representation on a larger data sample and its consistency between north and south pole and among different orbits.

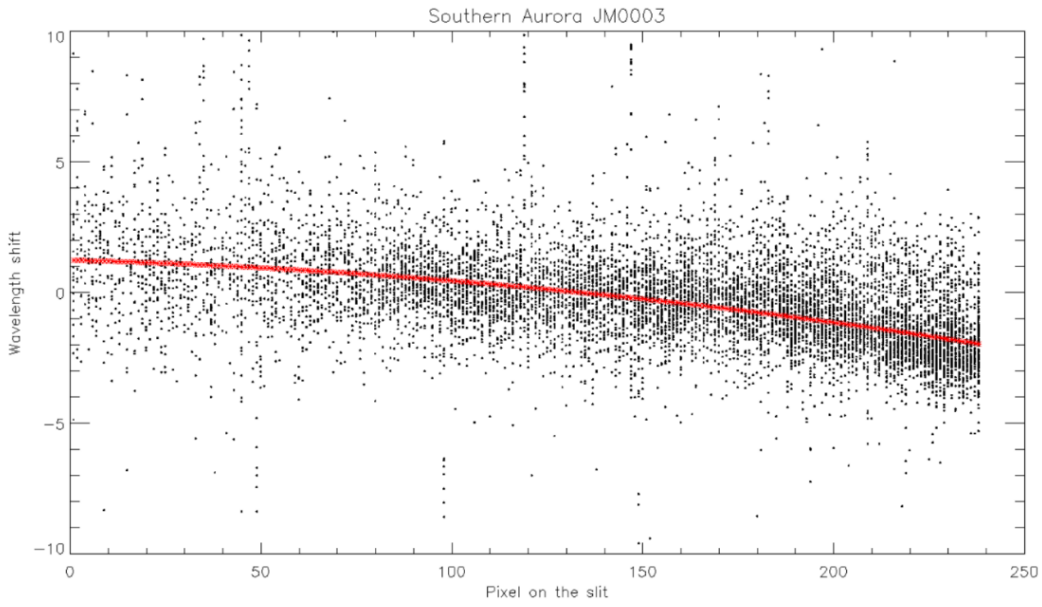

Fig 5.8 Scatterplot relative to the JM0003's southern aurora obtained by plotting the retrieved wavelength shift values vs the positions of the pixels on the slit where the measurements are performed. The red line represents the second-order polynomial function which better fit the plot.

With the purpose to determine the theoretical law relating the wavelength shift and the corresponding pixel's position on the slit, the same procedure adopted by *Dinelli et al* (2017) has been applied to the JM0003/SP dataset, that both provides a large number of observations and some of the most intense auroral signals ever detected. A least-square polynomial fit has been then performed considering the results of the first run (Fig 5.8) and, consequently, three coefficients have been derived to fit a parabola to the set of retrieved wavelength-shift versus pixel position. The obtained

coefficients have been applied to the wavelength shifts retrieved from the other orbits. The tested polynomial function well approximates the wavelength shift observed in all the other datasets, therefore this function has been implemented in the retrieval code, reducing the free parameters of the retrievals to just the H_3^+ T and CD, the methane's CD and the intensity offset, whose initial guesses values and a-priori errors are reported in Tab 5.2.

Parameters	*Initial guess*	*Initial error*	*Fit*
T H_3^+ [K]	700	500	fitted
CD H_3^+ [mol cm^{-2}]	$1.0 \cdot 10^{12}$	$5.0 \cdot 10^{13}$	fitted
T CH_4 [K]	600	–	fixed
CD CH_4 [mol cm^{-2}]	$1.0 \cdot 10^{12}$	$1.0 \cdot 10^{15}$	fitted
Wavelength shift [nm]	*computed*	–	fixed
HWHM [nm]	11	–	fixed
Offset a	0.4	1	fitted

Tab 5.2 Input values of the retrieval parameters and the relative a-priori errors.

5.5 Filtering of the retrievals

The number of the analysed spectra is so high to prevent a visual inspection of the results obtained in the analysis of any single one. Therefore, once the retrievals of all the selected measured spectra have been performed, a strategy to filter all the results exhibiting an unsatisfactory fit of the observed spectrum has to be designed. Such a procedure allows to exclude all the spectra characterized by noise or low auroral signal, which could affect the final maps and, hence, distort the conclusions. In this study, in order to only preserve the most consistent retrievals, four main filters have been used:

1. ***Chi square filter***

   The final χ-test (the sum of the squares of the difference between the measured and simulated spectrum normalised for the measurement noise) of the single retrievals is an indication on how well the observed spectrum is reproduced by the retrieved set of parameters. χ-test values of 1 or below 1 indicate that the measured spectrum is reproduced within the measurement noise. All the analysed datasets show a χ-test occurrence distribution of the retrievals with a peak around small values and a lower frequencies tail of larger values (Fig 5.9). Such a result proves that the majority of the observed measurements are well reproduced by the retrieval code. However, the code cannot

reproduce spectra characterized by anomalous spikes. Therefore, it is necessary to set a χ^2-threshold beyond which the results of the retrieval should be rejected: here, only the final results for which the χ-test was smaller than 40 have been retained.

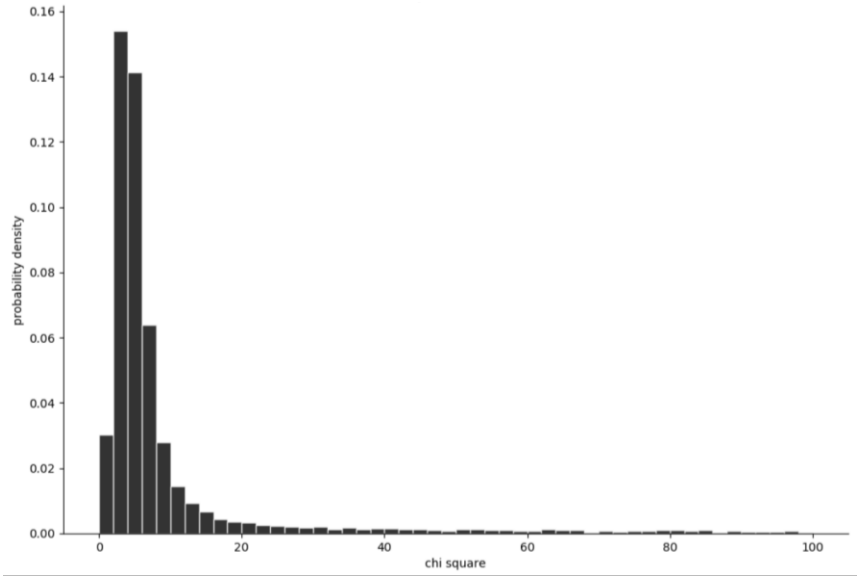

Fig 5.9 Histogram of the χ-test distribution for the retrievals resulting from the analysis of the JM0081 dataset.

2. ***Filter on the value of the Marquardt's lambda***

In section 2.4 the Levenberg-Marquardt method and the damping factor λ_{LM} have been introduced to solve non-linear least square problems. Given an initial guess for the set of fitted parameters, λ_{LM} has to be initialized to a modest value λ_0 (here 0.1) and a factor ν>1 has to be used to adjust the damping term at each iteration of the retrieval. Initially, the χ-test value is computed for $\lambda_{LM} = \lambda_0$ and secondly for $\lambda_{LM} = \lambda_0/\nu$. If in both the cases the χ^2 results larger than the initial point, the damping parameter is increased by successive multiplication by ν, until a better point is not found. If the λ_0/ν leads to a reduction of the χ-test value, then this is taken as the new λ_{LM} and the process continues, iterating till convergence is achieved. Because the λ_{LM} increases when χ^2 increases and decreases when χ^2 decreases, when the Marquardt's lambda stays fix at its initial value some problems may have occurred during the retrieval process. Therefore, all the retrievals showing $\lambda_{LM} \geq 0.1$ have been removed from the final results.

3. ***Column density error filter***

In order to consider only those retrievals whose results are mainly coming from the analysed observation, along with the chi square, the error associated with the retrieved data have to be

considered. In fact, all the results from observations containing small information, which tendentially remain close to the a-priori value (used also as initial guess of the retrieval) usually exhibit a large percentage retrieval error and have to be removed. Therefore, in this study, the retrieved column densities of the emitting species with a percentage retrieval error larger than 50% have been filtered out. In Fig 5.10 the histograms of the H_3^+ and CH_4 column densities before and after the filtering process are shown, highlighting the variation of the distributions.

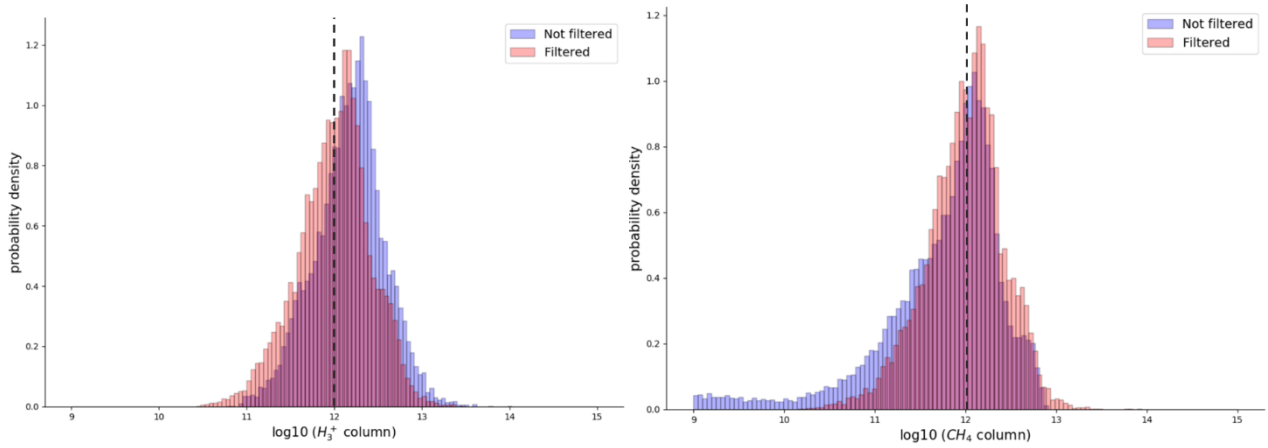

Fig 5.10 (a) Histogram representing the H_3^+ column density distribution before (blue) and after (red) filtering for the retrieval errors. **(b)** CH_4 density distribution before and after removing the retrievals with a percentage error larger than 50%. The black dashed lines represent the a-priori values of the H_3^+ and CH_4 column densities.

4. *Temperature error filter*

As for the column densities, the H_3^+ temperatures have also been filtered considering only the results where some information about the retrieved quantity was extracted from the measurements. To determine the contribution of each observation, a quantifier q has been adopted, defined as:

$$q_{ij} = -\frac{1}{2} log_2 \left(\frac{S_{rj}}{S_{aj}} \right) \tag{5.2}$$

where S_{rj} represents the diagonal element of the variance-covariance matrix of the retrieval, while S_{aj} is the diagonal element of the variance-covariance matrix of the a-priori information for a particular point j. This quantifier, also called *individual information gain,* gives a measure of the information gain provided by the analysed measurements with respect to the a-priori knowledge

of each retrieved value: when the information in the measurements is low, the retrieval error gets close to the a-priori error and q is almost null; instead, when the quantifier is larger than zero it means that some information has been extracted from the measurements. Usually, for values of q lower than 0.5 (corresponding to a reduction of the a-priori error by a factor $\sqrt{2}$) the retrieved estimate is considered to come mainly from the initial guess of the target quantity; therefore, in this thesis only temperatures associated with $q \geq 0.5$ have been retained [Dinelli et al. (2010)]. As it can be seen from Fig 4.6, after filtering for the individual information gain, retrievals with errors larger than 250 K are removed (Fig 5.11b). As a consequence, the bias in the temperature retrieval is reduced and the number of occurrences around the a-priori value in the H_3^+ temperatures distribution decreases (Fig 5.12).

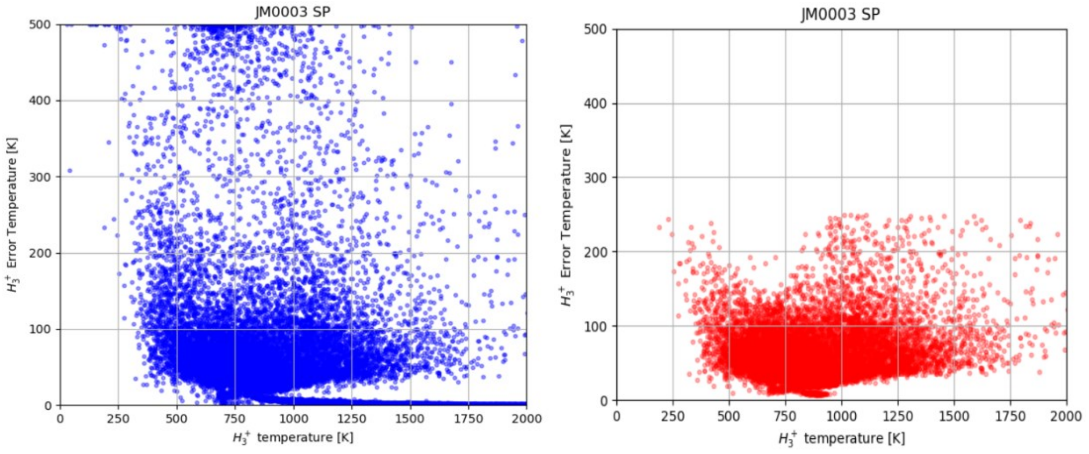

a **b**

Fig 5.11 (a) Scatterplot of H_3^+ temperatures vs H_3^+ temperature error before filtering for $q \geq 0.5$. **(b)** Scatterplot of H_3^+ temperatures vs H_3^+ temperature error considering $q \geq 0.5$.

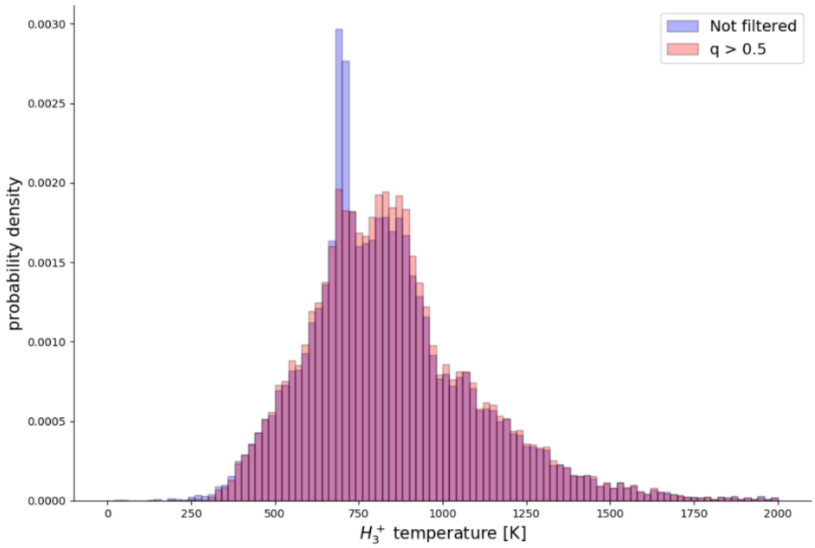

Fig 5.12 H_3^+ temperature distribution before (blue) and after (red) filtering for $q \geq 0.5$.

Finally, in Fig 5.13, the three-variable scatterplots representing the retrieval results before any filtering (top) and after the combining of all the filters $(bottom)$ are shown. In Fig 5.13b the plot highlights the anticorrelation between H_3^+ column densities and temperatures.

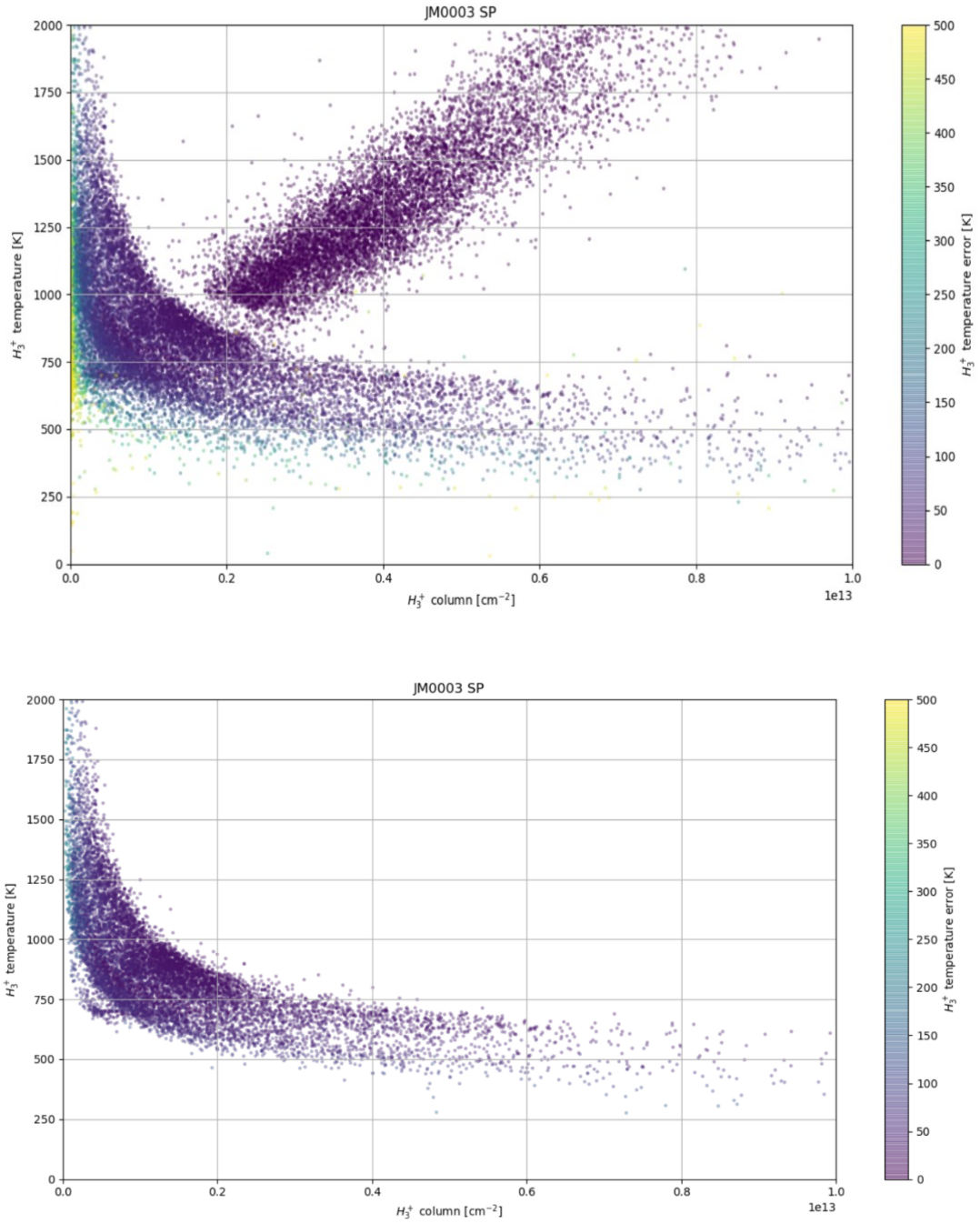

Fig 5.13 (a) Scatterplot of H_3^+ column density vs H_3^+ temperatures and in color the H_3^+ temperature error before any filtering **(b)** Scatterplot of H_3^+ column density vs H_3^+ temperatures and in color the H_3^+ temperature error after filtering for $\chi^2 < 40$, λ_{LM}<0.1, column density's percentage error <50% and q≥0.5.

5.6 H_3^+ column density and temperature in Jupiter's polar regions

With the purpose to identify patterns and compare the final results of the analysis with the images obtained using the L-band imager and detect morphological variations of the aurorae, we represent the results as distribution maps. These maps consist in contour plots of the average bin quantities, which have been obtained by diving the area in the orthographic projections into bins and averaging all the retrievals and corresponding errors inside each bin. Because the emission angle of the analysed measurements can assume a wide range of values and because the retrieved column densities are proportional to the optical path of the slant column, before generating the maps all the retrieved CD values have been multiplied by the cosine of the corresponding emission angles, generating in this way a set of vertical column densities. The vertical layer containing the emitting species has then been assumed to be constant at each geolocation bin.

5.6.1 H_3^+ column density and effective temperature maps for the North aurora

Among the two orbits selected and analysed for the study of the north aurora, only the retrievals relative to the JM0003 have been mapped and examined. In fact, JIRAM data from orbit JM0041 show very low auroral signals, making the detection of both H_3^+ and methane emissions difficult. For this reason, it has been decided to set this dataset aside for further analyses, that are necessary to get as much information as possible from these measurements. Therefore, in this thesis the study of the north aurora has been based on the results from the orbit JM0003, which are here reported in Fig 5.14. In panel *a*, as a confirmation of *Dinelli et al.* (2017) study, the distribution of H_3^+ column densities shows a peak in correspondence of the right side of the auroral oval, mainly above the model oval (dashed line) and in part almost coincident with the statistical oval (solid line). This structure can be also clearly identified in panel *b*, by looking at the map of the relative errors on the retrieved column densities; in fact, this region shows low error values, ranging around 10-20%, highlighting the consistency of the retrieval results. Also, on the left side of the main oval, another area with large H_3^+ abundances and small relative errors can be found lying well inside the two reference ovals and spreading out toward the pole. This structure appears more distinctly in Fig 5.14b, while no emission arc as sharp as the one on the right can be identified by looking at the abundances map. This may be attributable to the inclusion in the analysis of the large number of spectra from the background population, which, as it has been observed, in several cases has led to the retrieval of anomalously high CD values and rather low relative errors. Consequently, these results have not been cut out by

the filters and might have caused the degradation of the auroral signal. Nevertheless, the addition of new data to the analysis has allowed the detection of a narrow arc of high H_3^+ column between the statistical and model oval, at longitudes of 180°-210°, not visible in the previous analysis. Also, a relevant abundance of H_3^+ can be spotted over the pole.

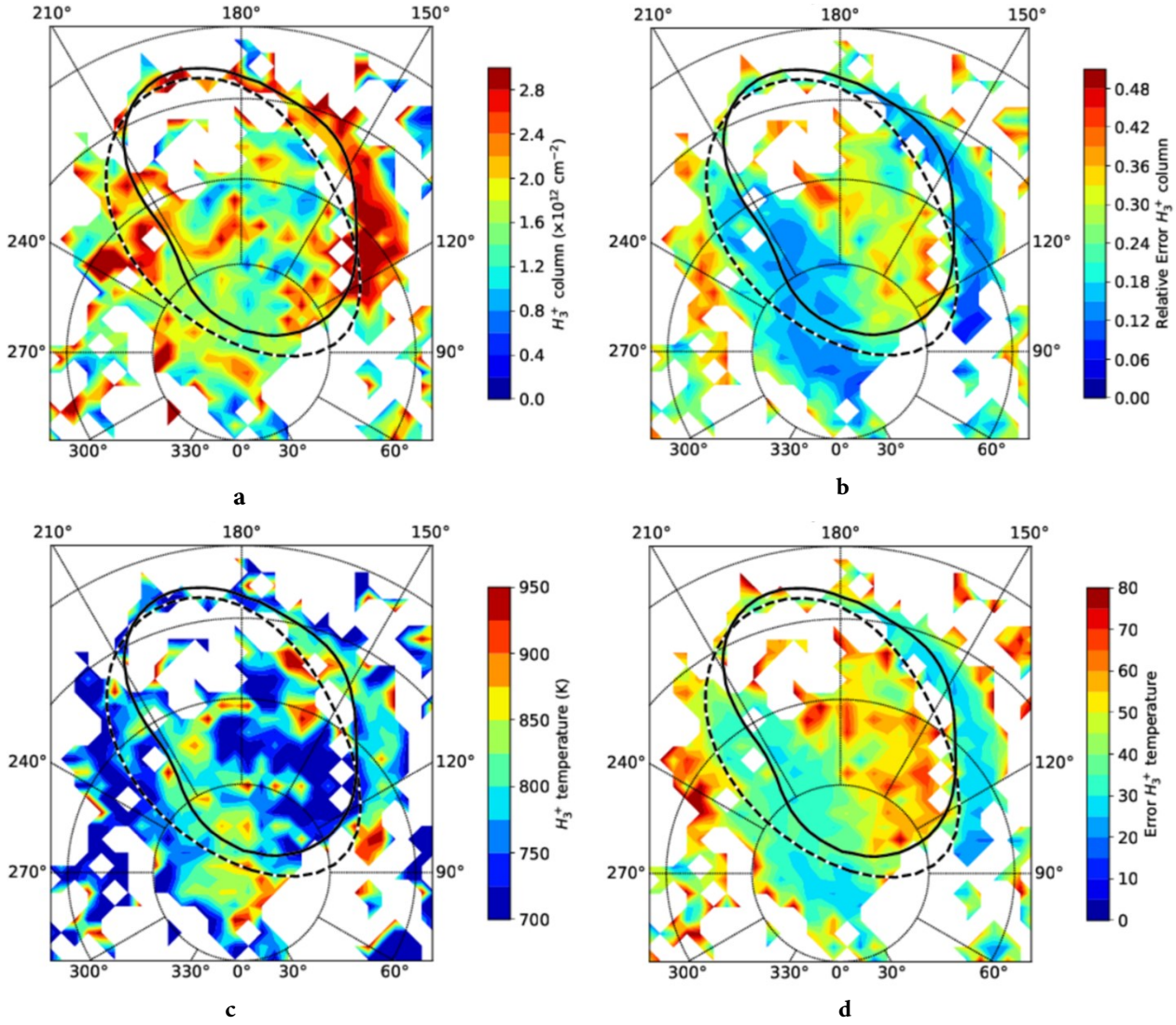

Fig 5.14 JM0003 North Pole. **(a)** Map representing the distribution of the retrieved H_3^+ column density; **(b)** Map of the average retrieval error on the retrieved column densities of H_3^+; **(c)** Map of the retrieved H_3^+ effective temperature; **(d)** Map of the average retrieval error on the retrieved temperature of H_3^+.

The regions where the larger amounts of H_3^+ can be observed coincide with those where the higher effective temperatures lay, showing a variability between 800-950 K (Fig 5.14c). Moreover, from Fig 5.13d it can be noticed that the higher temperatures are associated with the lower errors on the retrieved H_3^+ T; in particular, the larger errors can be found inside the oval and in the background region, where the H_3^+ concentrations are low. Therefore, as already pointed out in section 5.5 [see Fig 5.13], H_3^+ column densities and temperatures appear anticorrelated. This anticorrelation may be explained, even if not completely, by considering the H_3^+ *thermostat effect,* according to which large H_3^+ abundances lead to an infrared cooling of the Jovian upper atmosphere, lowering the temperatures.

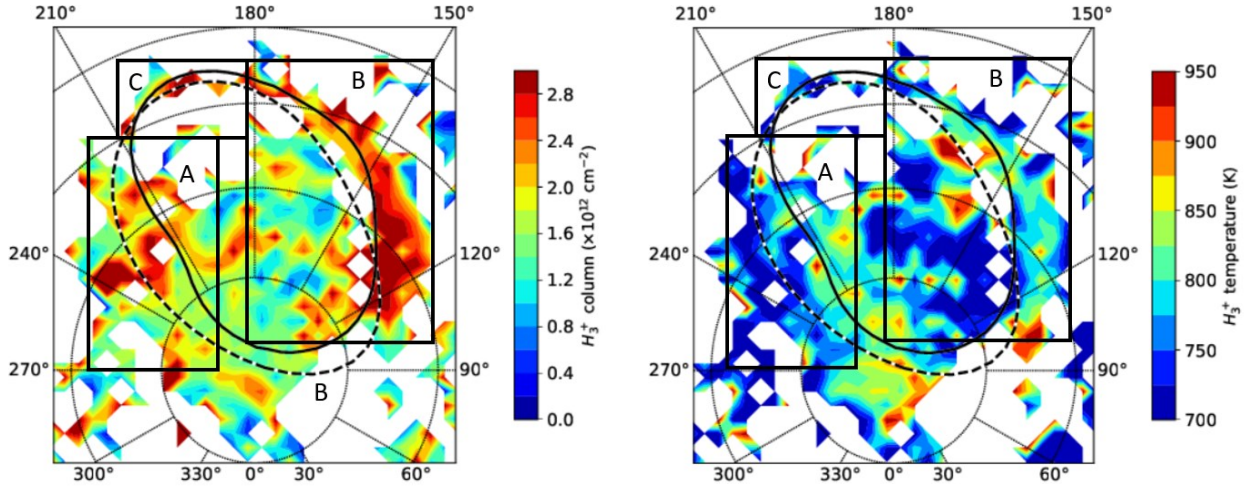

Fig 5.15 Comparison between H_3^+ column density (*left*) and temperature (*right*) distributions for the orbit JM0003 NP.

To better describe Jupiter's north aurora, in Fig 5.15 three regions of main interest have been identified and a comparison between the distribution of the H_3^+ column densities and temperatures has been performed.

- **A** [longitudes from 210° to 240° and latitudes from 90°N to 65°N] → In this region the higher H_3^+ column densities are located inside the model oval and show variation from $2.2 \cdot 10^{12}$ cm^{-2} to $2.8 \cdot 10^{12}$ cm^{-2}. Instead, anomalously high-density values laying outside the reference ovals can be attributed to some background measurements for which the retrieval failed. At the pole, inside the statistical oval and close to it, the H_3^+ temperature range around 775-900K, showing few spots with temperatures larger 900 K.

- **B** [longitudes from 110° to 180° and latitudes from 75°N to 58°N] → At higher latitudes, just above the model oval and closer to the statistical one, we see the highest H_3^+ column density values, which exceed $2.8 \cdot 10^{12}$ cm^{-2}. Equatorward, where the auroral signal almost coincide with the statistical oval, the abundance of H_3^+ ranges around $2.0\text{-}2.8 \cdot 10^{12}$ cm^{-2}. Along the main oval the H_3^+ temperatures are quite low, showing values within the interval of 775-825 K. Instead poleward, close to the model oval, a peak of temperature can be detected ($\sim$ 925 K) in a region where the H_3^+ concentrations are low.

- **C** [longitudes from 180° to 210° and latitudes from 55° to 60°N] → Thanks to the larger dataset used in this work, the region inside frame C displays a structure not observed in the previous analysis: a narrow arc of high H_3^+ column densities laying above the statistical oval. This result finds confirmation in the imager L-band's image of the north aurora realized by Mura [see section 5.8], where a fine auroral emission along the main oval can be observed.

5.6.2 H_3^+ column density and effective temperature maps for the South aurora

For the study of Jupiter's south aurora, the orbit JM0041 have been disregarded for the reasons already discussed in the previous section. The focus has been then posed on the orbits JM0003, JM0071 and JM0081 and the contour plots of the corresponding retrievals are here shown in Fig 5.16, Fig 5.17, and Fig 5.18, respectively.

1. **Orbit JM0003**

   In Fig 5.16a the main oval emission appears quite distinctly close to the model oval, where significative abundances of H_3^+ can be detected. On the left side of the map, the CDs distribution appears narrower than on the right side and H_3^+ concentrations result lower. In fact, between 330°-240° of longitude and 60°-70°S of latitude the H_3^+ column densities vary from $1 \cdot 10^{12} cm^{-2}$ to $1.8 \cdot 10^{12}$ cm^{-2}; instead, in the region confined between 0°-90° of longitude and 60°-70°S of latitude, other than a more diffuse distribution of H_3^+ inside the statistical oval with an average value of $1.7 \cdot 10^{12} cm^{-2}$, peaks of density can be spotted just above the model oval and are estimated to be around $2\text{-}2.8 \cdot 10^{12}$ cm^{-2}. As it can be notice from panel *b*, these regions are also associated to low retrieval errors, whereas outside of the auroral region H_3^+ column densities

which appear anomalously high are also characterized by large errors and have been, hence, interpreted as noise from the background. As already observed in the north aurora, panel *c* exhibits a relevant anticorrelation between column density and temperature of H_3^+, suggesting that the thermostat effect may play an important role in the south aurora too. In fact, all the regions characterized by higher H_3^+ densities show temperatures of about 850-900 K, while in those area inside the main oval where H_3^+ concentrations are lower effective temperatures may rise to values larger than 950 K. Moreover, along and close to the model oval the retrieval errors on temperature appear among the lowest, ranging around 25-45% (*panel d*)

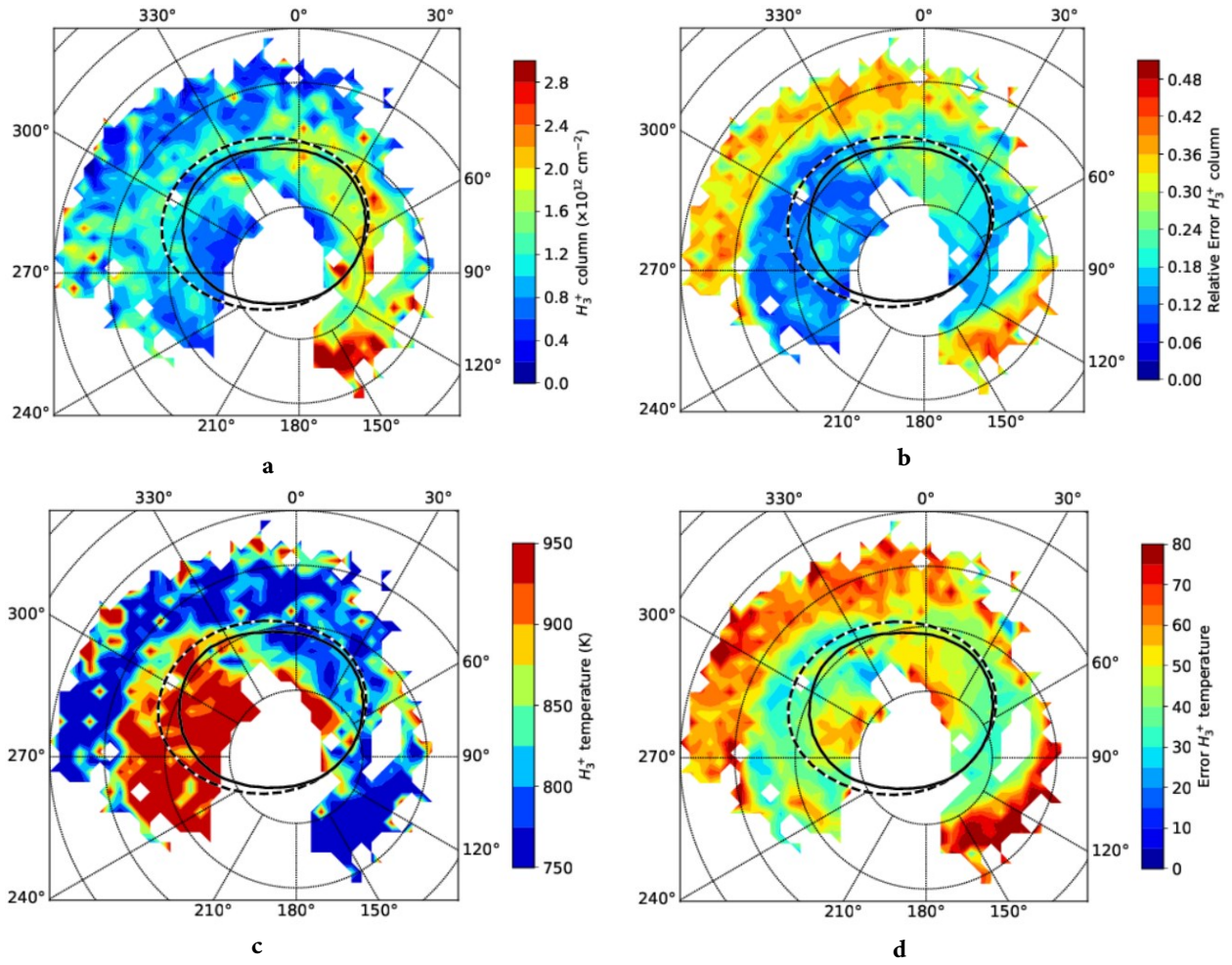

Fig 5.16 JM0003 South Pole. **(a)** Map representing the distribution of the retrieved H_3^+ column density; **(b)** Map of the average retrieval error on the retrieved column densities of H_3^+; **(c)** Map of the retrieved H_3^+ effective temperature; **(d)** Map of the average retrieval error on the retrieved temperature of H_3^+.

2. Orbit JM0071

The map in Fig 5.17a displays distinctly the auroral oval. In fact, between the range 0°-90° of longitudes, just above the model oval, an arc-shaped structure exhibiting high H_3^+ concentrations can be identified. In this region, CD values show a variability between 2.2-2.8· 10^{12} cm^{-2} and several peaks larger than 2.8· 10^{12} cm^{-2}. As for the orbit JM0003, anomalously high abundance values can be noticed quite far from the main oval, which have been flagged as residual noises from the background. As a confirmation of this evaluation, in Fig 5.17b the higher retrieval errors can be found in those regions where unsure retrievals fall, while smaller errors are located closer to the main oval.

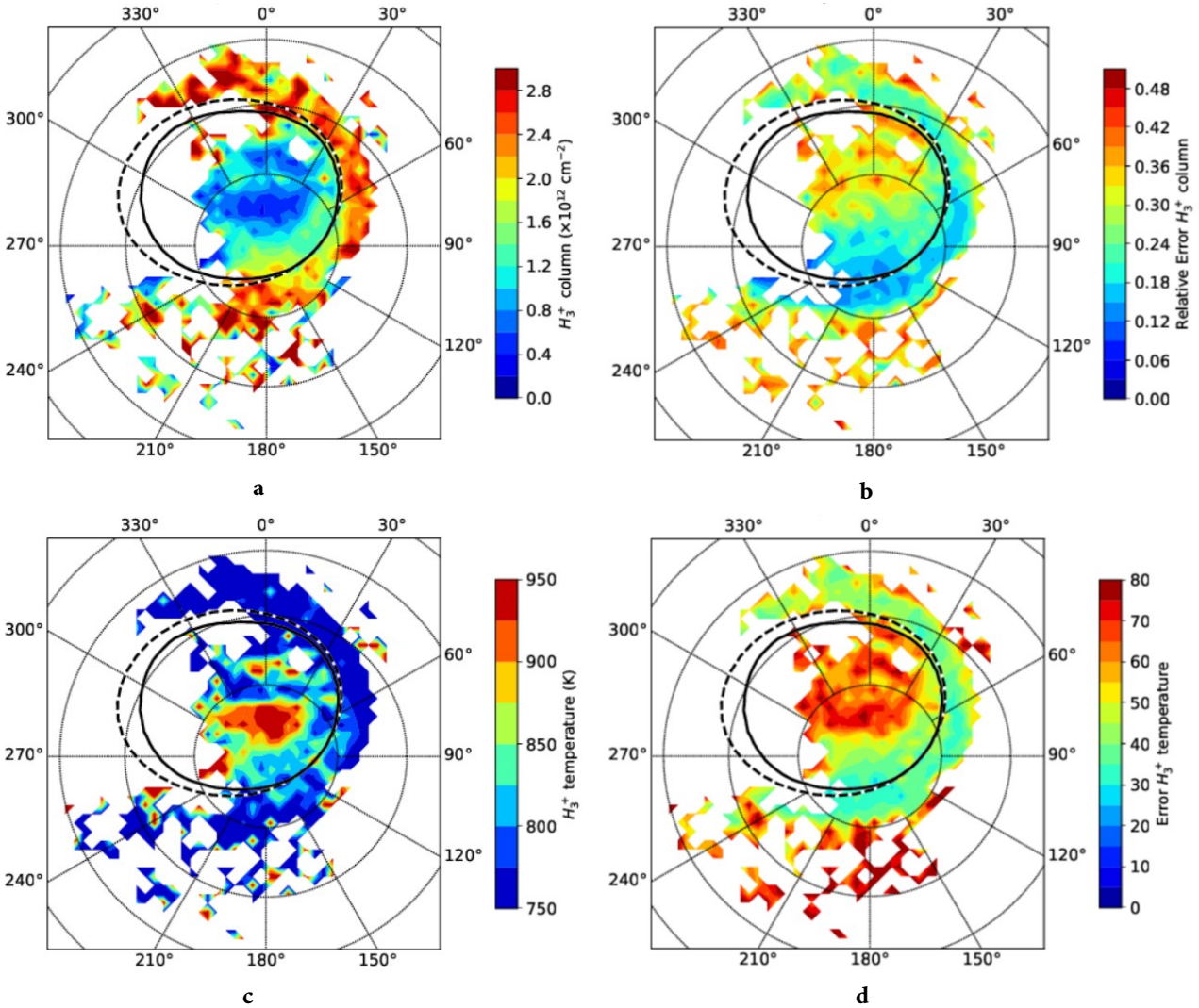

Fig 5.17 JM0071 South Pole. **(a)** Map representing the distribution of the retrieved H_3^+ column density; **(b)** Map of the average retrieval error on the retrieved column densities of H_3^+; **(c)** Map of the retrieved H_3^+ effective temperature; **(d)** Map of the average retrieval error on the retrieved temperature of H_3^+.

The map in panel *b* also facilitates the detection of significative H_3^+ concentrations above the pole between the two reference ovals, where the auroral signals mingle with the noisy background appearing less evident in panel *a*; in fact, the region between 120°-210° of longitude and 80°-90°S of latitude displays the lowest relative errors on the retrieval of H_3^+ CD, with an average estimate of 15%. Panel *c* confirms what already seen for the previous two orbits: to higher H_3^+ concentrations values correspond lower effective temperatures. In particular, a large area above the pole exhibits temperatures larger than 900 K. As will be seen in the next section, this region is characterized by diffuse presence of methane, whose emission overcome that of the H_3^+ justifying the retrieval of such high temperatures and low H_3^+ abundances. Moreover, the various spots of high H_3^+ T far from the main oval suggest that multiple unreliable values may have been included in the final results; therefore, further analyses are necessary to investigate the origins of these anomalies, with the aim to improve their retrieval.

3. Orbit JM0081

The maps in Fig 5.18 display the result of the retrieval for the orbit JM0081, during which JIRAM achieved a great coverage of the southern auroral region, providing an almost complete detection of the entire main oval. In fact, in Fig 5.18a an oval-shaped distribution of high H_3^+ column densities can be detected between 65°-80°S, apparently shifted with respect to the reference ovals. In this map four main regions of interest have been identified:

1. [longitudes from 0° to 40° and latitudes from 65°S to 75°S] → In this region high H_3^+ column densities lie just above, and partially along, the model oval, assuming a sharp and narrow shape. Here the abundances range between $2\cdot 10^{12}$ and $2.6\cdot 10^{12}$ cm^{-2} and their retrieval errors do not exceed 15% (panel *b*). Also, this region is characterized by an average H_3^+ temperature of 800 K, whose retrieval error is about 30 K.

2. [longitudes from 40° to 150° and latitudes from 70°S to 82°S] → At 40° of longitude the emission oval departs from the reference oval: it is shifted equatorward and remains almost totally confined within 70°-80°S. In this region, the H_3^+ column densities amount around 2.4-$2.8\cdot 10^{12}$ cm^{-2} and are associated with low retrieval errors which vary from 10% to 18%, while the temperatures stay always below 850 K.

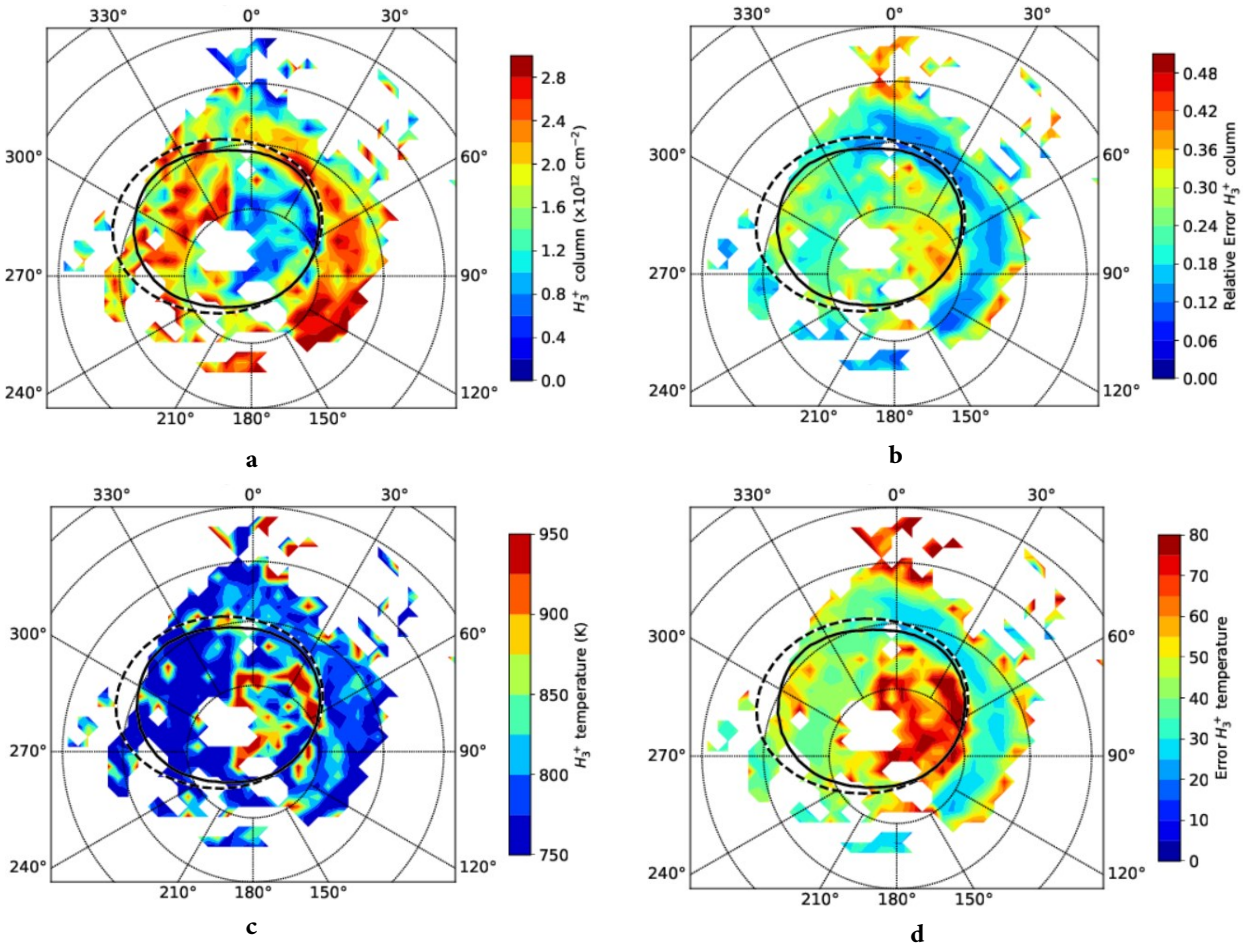

Fig 5.18 JM0081 South Pole. **(a)** Map representing the distribution of the retrieved H_3^+ column densities; **(b)** Map of the average retrieval error on the retrieved column densities of H_3^+; **(c)** Map of the retrieved H_3^+ effective temperature; **(d)** Map of the average retrieval error on the retrieved temperature of H_3^+.

3. [longitudes from 270° to 350° and latitudes from 65°S to 80°S] → At these longitudes, inside the statistical oval, high concentration of H_3^+ ($2.6 \cdot 10^{12}$ cm^{-2}), with peaks exceeding $2.8 \cdot 10^{12}$ cm^{-2}, can be detected. This area is affected by errors on the retrieval of the column densities which appear higher than those on the right side, but still smaller than 20%; while, the temperatures are below 775 K, with a relative error of 40 K. Therefore, in this region the retrieval errors result generally higher than those on the right side and the H_3^+ CDs distribution appears quite patchy and less sharp with respect to the other two regions just described.

4. [longitudes from 170° to 270° and latitudes from 67°S to 80°S] → At these longitudes, quite far from the reference ovals, few areas with large H_3^+ densities (higher than $2 \cdot 10^{12}$ cm^{-2}), temperatures below 850 K and low retrieval errors can be identified. These structures may suggest some variations in the auroral morphology; therefore, in section 5.8 Fig 5.18a will be

compared with the image of the aurora acquired by JIRAM in the L-band, to verify if this area actually coincides with intense auroral emissions.

Finally, similarly to the orbit JM0071, high temperature values can be observed inside the main oval, near the pole. As it will be seen in the next section, this region exhibits large concentration of methane and it is hence associate to low H_3^+ densities.

5.7 CH_4 distribution in Jupiter's polar regions

In this section, the maps of the CH_4 distribution both at the north and south pole are presented and discussed. These plots have been realized by using the results of the retrieval analysis, which has been performed starting from the assumption that the observed methane emission is optically thin [Altieri et al. (2016)]. Also, as for the H_3^+ CDs, all the retrieved methane slant column densities have been multiplied for the cosine of the emission angles of the corresponding measurement and turned into vertical columns. The final maps are reported in Fig 5.19 and show the relative CH_4 abundance for each of the orbits under study. In fact, since the methane column densities are 100% correlated to the temperature value assumed in the retrievals, their values can only be used to represent the methane contribution to the observed spectra [Moriconi et al. (2017)]. For this reason, to enhance the spatial distribution of methane, the CH_4 column densities have been divided by the highest value obtained for the corresponding polar region. As it can be noticed from Fig 5.19, all the four projections show a major contribution of methane inside the main oval, with peaks of concentration apparently shifted with respect to the center of the emission oval. However, CH_4 can also be detected outside the main oval, usually in lower concentration, and it is thought to spread outward due to atmospheric circulation [Caldwell et al. (1983)]. Therefore, in order to highlight analogies and differences between north and south auroras, as well as any evolution of the CH_4 distribution at Jupiter's south pole, a more detailed description of these maps is reported below.

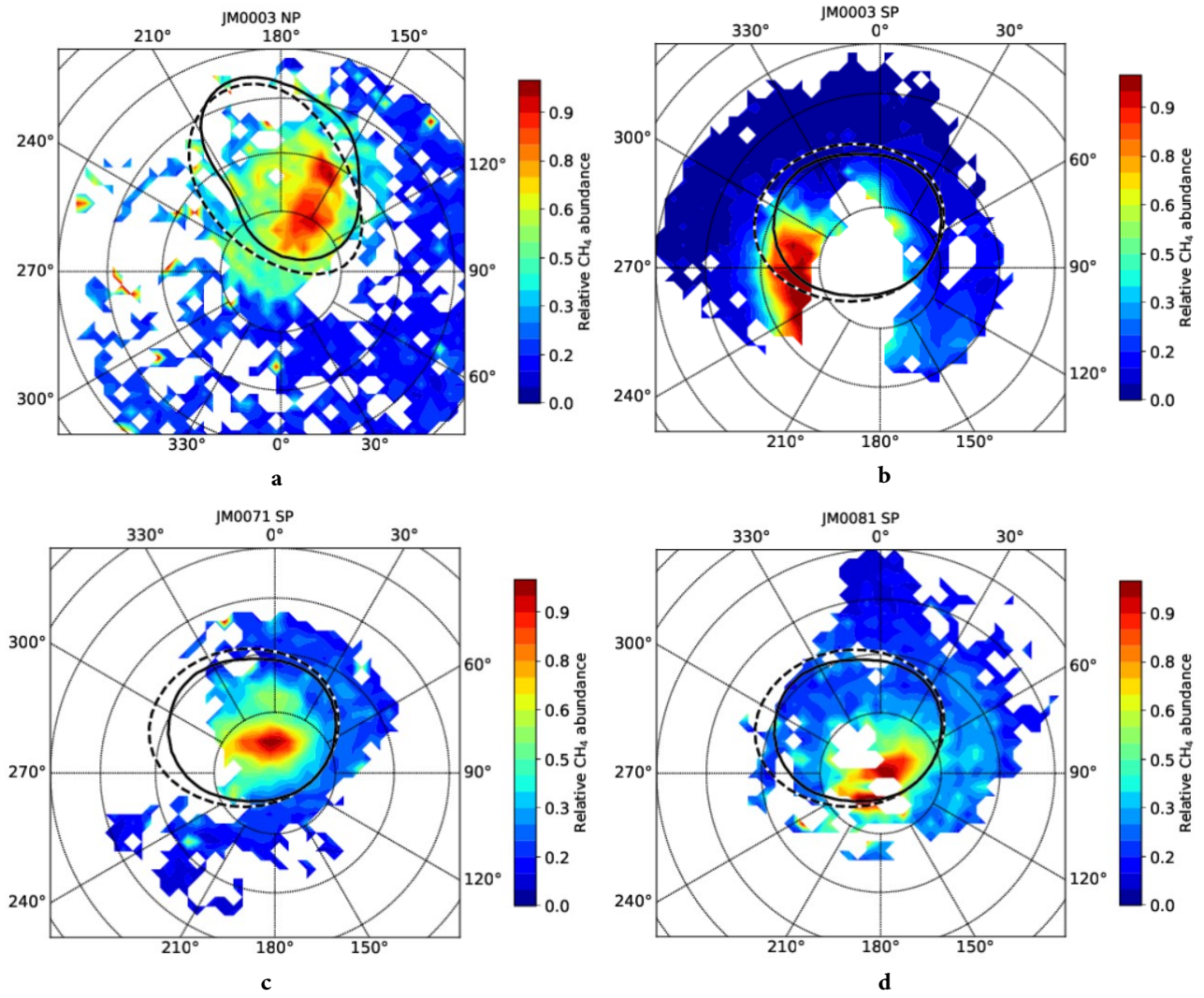

Fig 5.19 Maps of the relative abundances of CH_4 at both Jupiter's poles retrieved from the 3.3 μm emission for the 600 K effective temperature. **(a)** CH_4 relative abundance retrieved in the north aurora using data from the orbit JM0003; **(b)** CH_4 relative abundance retrieved in the south aurora using data from the orbit JM0003; **(c)** CH_4 relative abundance retrieved in the south aurora using data from the orbit JM0071; **(d)** CH_4 relative abundance retrieved in the south aurora using data from the orbit JM0081.

a. JM0003 North Pole

In the north pole the distribution of the normalized column densities of methane is almost totally concentrated inside the main oval, in the region between 160°-180° of longitude and 70°-85°N of latitude. Here, two main peaks of relative abundance can be detected: one above the 90th parallel and the other around 72° of latitude. Also, fainter contribution by methane can be observed diffusing poleward, outside the emission oval.

b. JM0003 South Pole

During orbit JM0003 JIRAM did not covered a large portion inside the south aurora oval, missing the majority of the region poleward 80°S and in between 180°-220° of longitude. The results of our analysis suggest that the peak methane contribution occurs exactly in the not covered area. In fact, three main CH_4 enhancements have been detected:

- [longitudes between -30° to 60° and latitude from 75°S to 85°S]→ In this region a significative concentration of methane can be spotted just inside the statistical oval and it is supposed to extend toward the center.
- [longitudes between 220° to 320° and latitude from 70°S to 80°S]→ Here most of the methane contribution is located, partially confined inside the main oval, while in the region 220°-250° it spreads outside, equatorward.
- [longitudes between 150° to 180° and latitude from 70°S to 80°S]→ In this region, quite far from the main oval, a spot of high CH_4 relative abundance can be observed and will be better examined in future analyses.

As already pointed out by *Moriconi et al* (2017), this distribution is expected to have a peak well inside the auroral oval. This hypothesis is confirmed by the work performed in this thesis through the analysis of data from orbit JM0071 and JM0081, which display a clear CH_4 enhancement over the south pole.

c. JM0071 South Pole

In this map, the expected peak of the CH_4 emission can be actually observed at latitudes larger than 80°S. It lies completely inside the main oval, departing from its center by only few degrees.

d. JM0081 South Pole

This plot displays an evolution in the morphology of the south aurora. In fact, with respect to the orbit JM0071, here the methane distribution exhibits a peak directly over the south pole and spreads outside the model oval between 150°-240° of longitudes. However, comparing these results with those relative to the retrieval of the H_3^+ column densities and temperatures (Fig 5.18), the CH_4 enhancement seems to lie inside the main oval, which, instead, appears shifted with respect to the reference ovals.

To support these results, in Fig 5.20 the maps of the relative errors on the retrieval of CH_4 column densities are shown. As it can be notice, all the structures above described coincide with regions of low retrieval errors, which never exceed 20%. Therefore, the plots confirm the robustness of the CH_4 retrievals both for the north and south aurora.

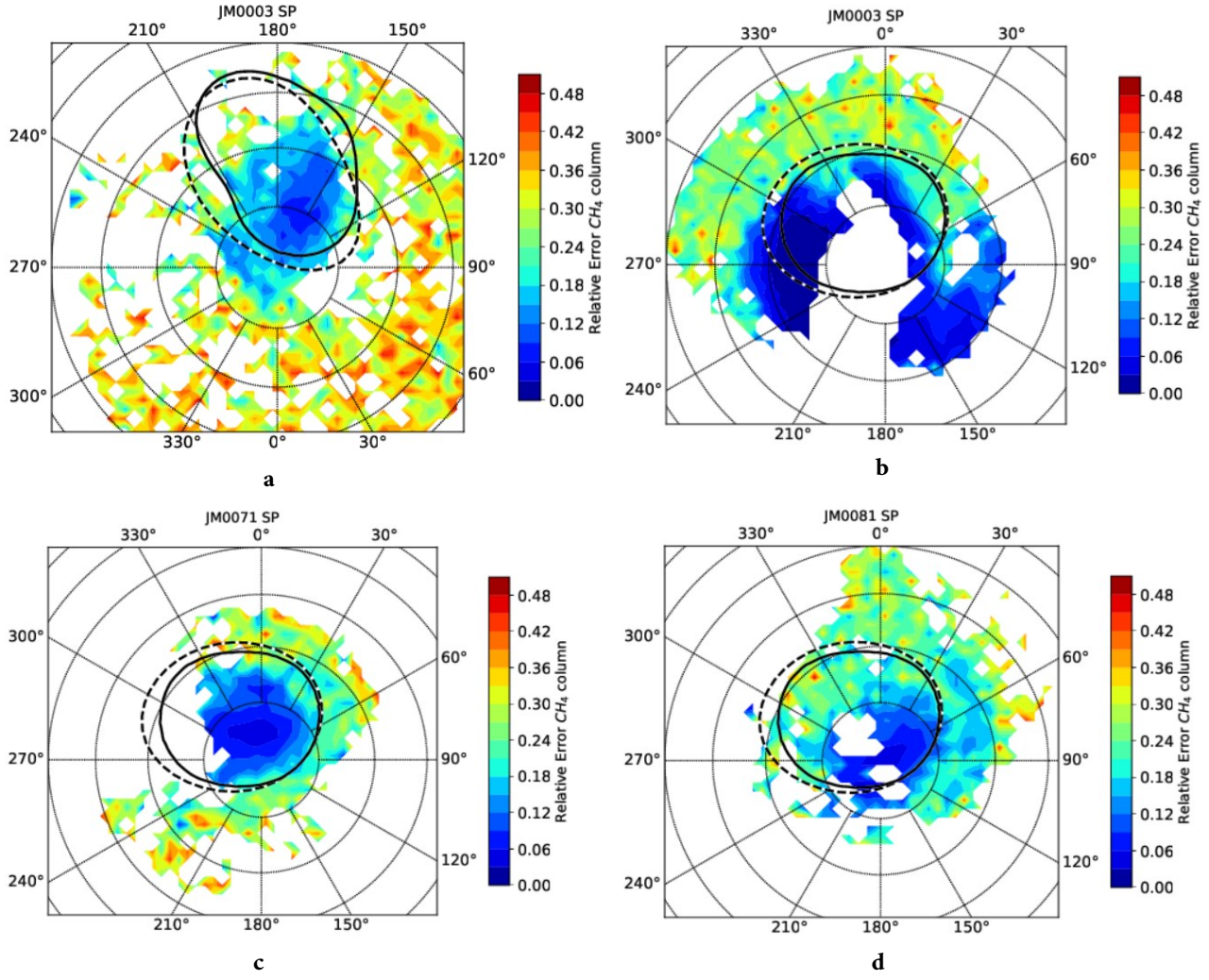

Fig 5.20 Maps of the relative error on the retrieval of the CH_4 column densities at both Jupiter's poles. **(a)** Orbit JM0003 north pole; **(b)** orbit JM0003 south pole; **(c)** orbit JM0071 south pole; **(d)** orbit JM0081 south pole.

5.8 Aurorae's morphology: comparison with the imager

As a conclusion of this work, for each of the analysed orbits the final maps of H_3^+ and methane abundances have been compared with the images (kindly made available by A. Mura) using the imager L band. These images have been realized mapping the measured radiances onto the reference surface of 500 km above the 1 bar level and consist of mosaic maps of the auroral emission. The imager has acquired the measurements at different times than the spectrometer and with a much higher spatial resolution. Therefore, the images can be used to study the morphology of the auroral emissions, but they cannot help in distinguishing among the emissions of different molecules, nor can they be used to infer the temperatures and abundances. The spectrometer, despite the lower spatial resolution, can help in assigning the measured emissions to the different molecules and evaluate their coarse abundance and temperature distribution. Therefore, the images provide an excellent picture of the spatial and temporal distribution of the Jovian aurorae, and show the morphology of the main oval, the polar region, and the satellite footprints [Mura et al. (2017)].

5.8.1 North aurora as seen from the spectrometer and from the imager

In Fig 5.21 the maps of the H_3^+ column densities (*left*) and the relative abundance of CH_4 (*center*) are compared with the results of JIRAM's imager observations of the H_3^+ infrared emission (*right*) collected around the first Juno's perijove at the north pole (JM0003). As it can be noticed from the map on the left, the peak of H_3^+ concentrations on the right side of the statistical oval, just above it, corresponds to a sharp arc of intense auroral emissions; instead, on the left side of the map high values of H_3^+ column densities spread toward the center of the main oval, in a region where the imager sees a broad emission composed by a series of coherent arcs. Other intense auroral signals can be observed by the imager above the pole, as well as between 180°-150° longitude and 70°-80°N, where significative abundances of H_3^+ lie. Finally, different from what will be observed in the south pole, in the region inside the main oval, where a large CH_4 contribution can be noiced (*center*), no significative emission has been detected by the imager.

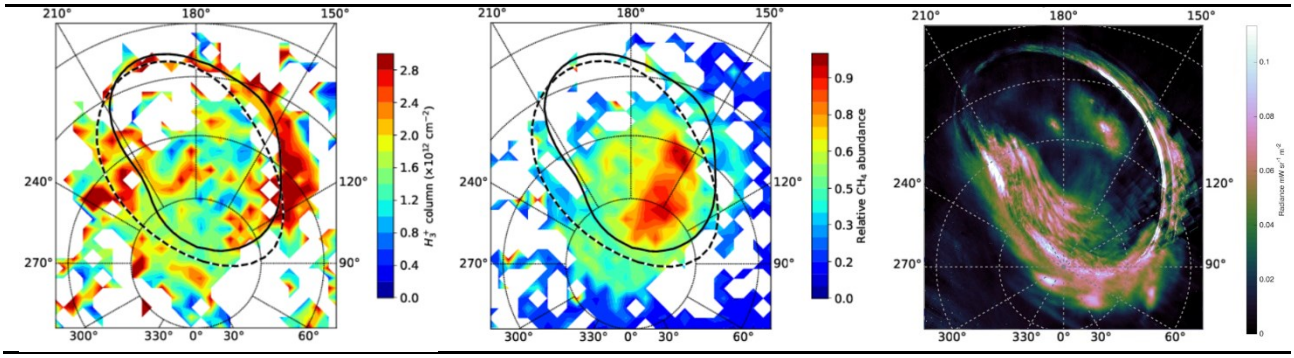

Fig 5.21 Comparison between the maps of the retrieved H_3^+ column densities $(left)$ and the maps of CH_4 relative abundances $(center)$ and the imager mosaic image $[mW\ sr^{-1}m^{-2}](right)$ for the orbit JM0003 NP.

5.8.2 South aurora as seen from the spectrometer and from the imager

Analogously to the north aurora, the morphology of the south aurora has been analysed for each of the selected orbits. The distribution maps obtained from this study and the images realized using observations of the L-band imager have been compared. Moreover, having available the maps covering the south pole for three successive orbits, some evaluations have been done on the spatial evolution over time of the southern aurora.

1. **Orbit JM0003**

   In the top panel of Fig 5.22, the imager's mosaic map $(right)$ shows a wide area of intense emissions on the right of the auroral oval, at latitudes larger than 70°S. In the same region, the map on the left shows significative abundances of H_3^+, with peaks of concentration where the emissions appear stronger. Moreover, the narrow arc of high H_3^+ column densities, laying on the left side of model oval, is seen as a sharp emission feature in the L-band images. As it has been already pointed out in the previous sections, during orbit JM0003 the spectrometer did not totally covered the region poleward 80°S, which instead was observed by the imager. Here, an intense signal coming from the pole can be identified, probably attributable to methane's emission which is supposed to peak at this latitude, inside the main oval. As a confirmation, in correspondence of the two areas of high CH_4 concentration other two emission structures can be noticed.

2. Orbit JM0071

The middle panel of Fig 5.22 shows a correspondence between the map of H_3^+ CDs distribution $(left)$ and the imager's map $(right)$: the region over the pole, above the model oval, where diffuse presence of H_3^+ large concentrations can be seen, is characterized by the highest radiance values, which mainly lie above 80°S. These emissions further extend along the auroral oval both eastward and westward, as the emission arc becomes more and more thin. Because at these longitudes no successful retrievals is present and because the imager did only cover regions at latitudes lower than the 65°N, the arc-shaped distribution of high H_3^+ abundances visible in the map on the left, can only be partially observed in the L-band's map as a faint auroral arc at higher latitudes. Also, inside the main oval, due to the presence of high CH_4 concentration, a significative methane emission can be observed.

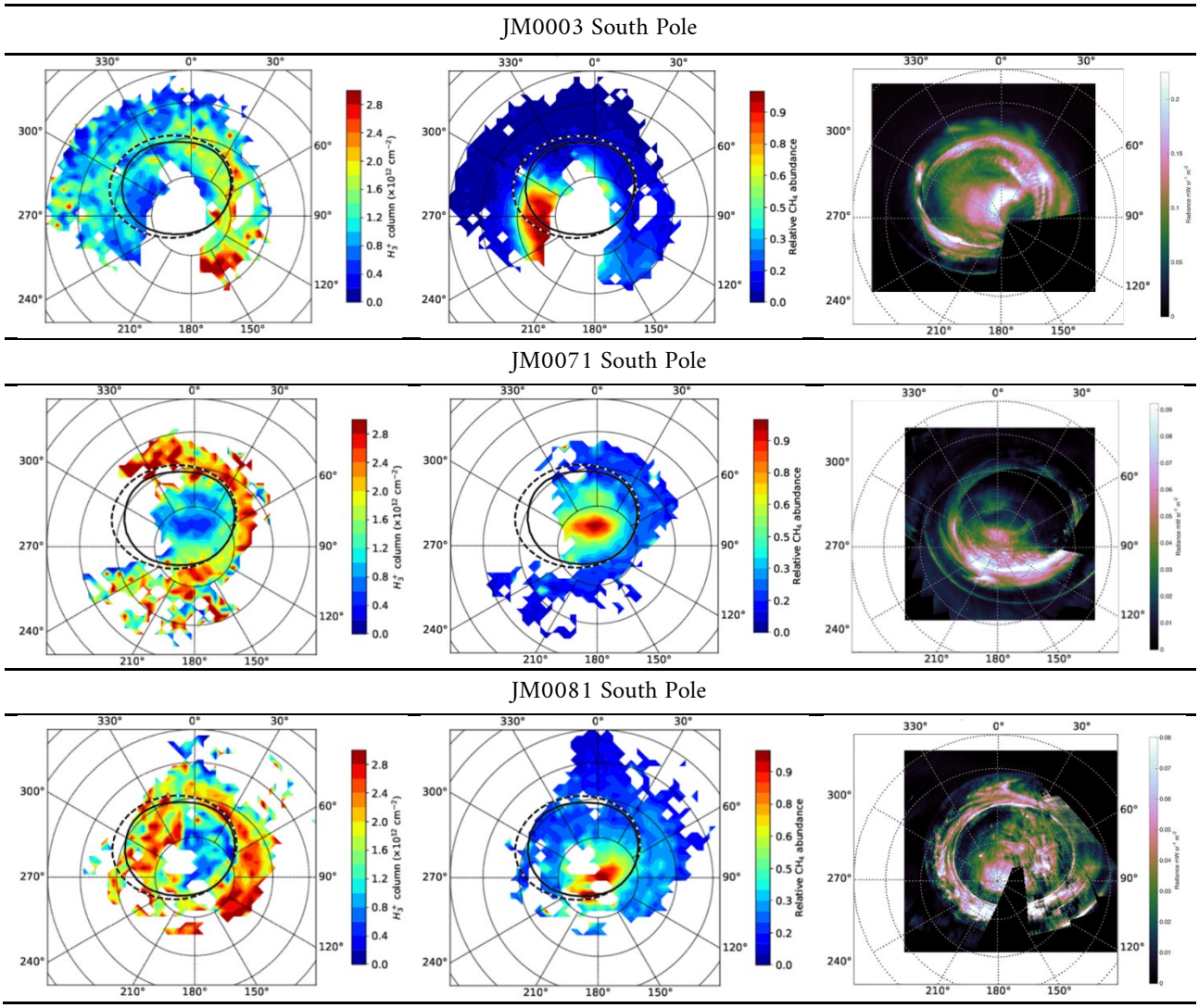

Fig 5.22 Comparison between the maps of the retrieved H_3^+ column densities $(left)$ and the maps of CH_4 relative abundances $(center)$ and the imager mosaic images $[mW\ sr^{-1}m^{-2}](right)$ for all the orbits analysed for the south aurora.

3. **JM0081**

In the bottom panel of Fig 5.22, the main oval is almost completely covered by all the three maps. However, the auroral emissions $(right)$ appear less coherent and noisier compared to the previous two orbits, probably affected by strong signals from the background. Nevertheless, several correspondences with the distribution maps can be found; in fact, the larger H_3^+ column densities lie along an oval-shaped structure almost coincident with the auroral emissions. This is more evident on the right side, where the higher H_3^+ CDs distribution appears sharper and the peak of concentration between 90°-150° of longitude correspond to a region of intense emissions. Instead, the patchier distribution of H_3^+ abundances on the left less fit the auroral oval. As for orbits JM0003 and JM0071, a strong methane emission can be observed just above the pole, enhancing the presence of high CH_4 concentrations, which strongly contribute to the observed spectra.

As already observed in previous studies [Mura et al. (2017)], in both the hemispheres the main oval is characterised by multiple structures of coherent pattern, e.g. concentric arcs of similar morphology and the south aurora shows higher intensity. Moreover, the hypothesis discussed in sections 5.6 and 5.7 of a spatial displacement of the southern aurora, seems to find confirmation in the imager's mosaic images. In fact, comparing the auroral emissions detected during the orbits from JM0003 to JM0081, the shape of the oval does not show relevant changes; however, in the JM0071 and JM0081 the main oval appears shifted of few degrees westward with respect to its location in the JM0003. In particular, for the orbit JM0003 the left side of the auroral oval lies around 65°-70°S, while its right side at about 70°S; instead, for the orbits JM0071 and JM0081, the right side of the aurora is located at latitudes larger than 70°-75°S and the right side is displaced toward 65°S.

Conclusions

After a preliminary investigation of the coverage of Jupiter's auroral regions achieved by JIRAM throughout the first ten Juno's perijoves, the orbit JM0003 has been selected for the study of the north aurora, while orbits JM0003, JM0071 and JM0081 have been considered to investigate the variability of the southern auroral environment. During these orbits, the aurorae have been mapped by both the spectrometer and the L band imager with unprecedent spatial resolution. This has enabled to retrieve the H_3^+ abundance, effective temperature and the CH_4 column density in the auroral regions, as well as to study the morphological evolution of the emission ovals.

For the retrieval of the emitting species, JIRAM spectral measurements in the 3-4 μm region have been inverted using the retrieval code described by *Dinelli et al.* (2017), which is based on a bayesian approach. The results of this analysis have been then used to produce distribution maps for both the polar regions, which have generally confirmed the locations of the maximum H_3^+ concentration and the anticorrelation between H_3^+ CD and H_3^+ T suggested by previous studies [Dinelli et al.; Adriani et al.; Moriconi et al.]. At the north pole, the higher H_3^+ abundances lie in the region at longitudes between 110° and 180°, close to the statistical oval. Here the H_3^+ column densities range between $2.0 \cdot 10^{12}$ cm^{-2} and $2.8 \cdot 10^{12}$ cm^{-2} and display some peaks exceeding $2.8 \cdot 10^{12}$ cm^{-2} at latitudes larger than 65°N. The temperatures along the main oval span between 700-950 K and show an apparent anticorrelation with the H_3^+ CDs, even if not as evident as in the south aurora. In fact, in the southern region, along the main oval, the distribution map of the H_3^+ abundances show values comparable with those retrieved in the northern region; however, on the auroral oval the temperatures never exceed 825 K. Moreover, the south aurora in the JM0071 and JM0081's distribution maps appears dislocated few degrees westward with respect to its position in the JM0003. The L band images reconfirm this shift, as well as show intense emissions just above the south pole where, according to the previous studies, the CH_4 contribution is supposed to peak. In this regard, the analysis has confirmed the diffuse presence of methane at both poles, inside the auroral ovals. Such a result may validate the hypothesis that the excitation leading to enhanced CH_4 infrared emissions is linked to magnetospheric phenomena, such as the auroral particle precipitation in the polar caps; however, the origin of this occurrence is still unsure.

In conclusion, the large number of spectral measurements analysed in this work has led to the detection of new structures and variations in the Jupiter's aurorae; however, it has also disclosed new problems, highlighting the necessity for further analysis. In particular, the origin of the anomalous peaks affecting the distribution maps of the H_3^+ column densities and temperatures, which are mainly located outside the main oval and hence have been flagged as residual noise from the background, will have to be better investigated in the future in order to improve their retrievals. The strong methane signal present in some of the auroral regions suggests that with an appropriate selection of the spectra to be analysed, we might be able to retrieve also the methane effective temperature, helping in this way to understand the origin of its enhanced emissions.

To date, being the NASA/Juno mission so recent, the study of Jupiter's aurorae from JIRAM measurements is just at its preliminary state. Many other data have yet to be analysed and they will be study material for the years to come. However, much remains to do on the spectra considered so far. In fact, along with the above-mentioned enhancements, some other analysis might be performed to increase the knowledge of the Jupiter's aurorae from the results of these preliminary retrievals. Firstly, orbit JM0041 has to be studied in more detail. In fact, despite of the great coverage of the polar regions provided by JIRAM, this orbit has been excluded from the analysis because of the weakness of the auroral signals and, consequently, the difficulty in detecting both the auroral and methane emissions from the spectral measurements. Therefore, a future challenge will be to get as much information as possible from these observations and this will also give the opportunity to identify some variations in the shape and/or location of the northern aurora with respect to the orbit JM0003. Other analysis can be based on the study of the correlation between the auroral signals and the local time, representing the correlation of the observed signals with the solar position with respect to the observational attitude. This research will be primarily useful to determine the excitation mechanism leading to the observed enhanced methane emissions, which may be associate either to auroral particle precipitation and/or Joule heating effect. Finally, because all the maps presented here are georeferenced in System III planetocentric geographical coordinates, it would be interesting to see these distributions plotted as a function of the magnetic coordinates.

Bibliography

Adriani, A. et al. (2014). JIRAM, the Jovian Infrared Auroral Mapper. Space Science Reviews. 213. 10.1007/s11214-014-0094-y.

Adriani, A. et al. (2017). Preliminary JIRAM results from Juno polar observations: 2. Analysis of the Jupiter southern H_3^+ emissions and comparison with the north aurora: Jupiter Southern Aurora from Juno. Geophysical Research Letters. 44. 10.1002/2017GL072905.

Adriani, A. et al. (2018). Clusters of cyclones encircling Jupiter's poles. Nature 555 (2018): 216-219.

Altieri, F. et al. (2016). Mapping of Hydrocarbons and H_3^+ Emissions at Jupiter's North Pole Using Galileo/NIMS Data: Hydrocarbons and H_3^+ by Galileo/NIMS. Geophysical Research Letters. 43. 0.1002/2016GL070787.

Bagenal, F. (2007). The magnetosphere of Jupiter: Coupling the equator to the poles. Journal of Atmospheric and Solar-Terrestrial Physics 69 387–40.

Bagenal, F. (2013). Planetary magnetosphere. T.D. Oswalt, L. French, P. Kalas (eds.), Planets, Stars and Stellar Systems. Volume 3: Solar and Stellar Planetary Systems, DOI 10.1007/978-94-007-5606-9_6.

Baumjohann, W., et al. (2010). Current Systems in Planetary Magnetospheres and Ionospheres. Space Science Reviews 152(1-4): 99-134, doi: 10.1007/s11214-010-9629-z.

Bolton, S., et al. (2017). Juno's first glimpse of Jupiter's complexity. Geophys. Res. Lett., 44, 7663–7667, doi:10.1002/2017GL074118.

Brown, R. A. (1983). Observed departure of the Io plasma torus from rigid corotation with Jupiter. Astrophysical Journal, Part 2, Letters to the Editor (ISSN 0004-637X), vol. 268, May 1, 1983, p. L47-L50.

Caldwell, J. A. et al. (1983). Further observations of 8-μm polar brightenings of Jupiter, Icarus, 53, 133–140, doi:10.1016/0019-1035(83)90026-X

Clarke, J., et al. (2002). Ultraviolet emissions from the magnetic footprints of Io, Ganymede and Europa on Jupiter. Nature. 415. 997-1000. 10.1038/415997a.

Connerney, J. and Satoh, T. (2000). The H_3^+ ion: A remote diagnostic of the jovian magnetosphere. Philosophical Transactions of The Royal Society B: Biological Sciences. 358. 2471-2483. 10.1098/rsta.2000.0661.

Cowley, S. W. H. and Bunce, E. J. (2001). Origin of the main auroral oval in Jupiter's coupled magnetosphere-ionosphere system. Planetary and Space Science 49, 1067–1088.

Delamere, P., et al. (2003). Momentum transfer between the Io plasma wake and Jupiter's ionosphere. Journal of Geophysical Research (Space Physics), Vol. 108, No. A6, 1241, doi:10.1029/2002JA009530.

Demtröder, W. (2006). Atoms, Molecules, and Photons. Springer.

Dinelli, B. M. et al. (2010). The MIPAS2D database of MIPAS/ENVISAT measurements retrieved with a multi-target 2-dimensional tomographic approach. Atmospheric Measurement Techniques. 3. 10.5194/amt-3-355-2010.

Dinelli, B. M. et al. (2017). Preliminary JIRAM results from Juno polar observations: 1. Methodology and analysis applied to the Jovian northern polar region. Geophysical Research Letters. 44, 4625-4632, doi:10.1002/2017GL072929.

Dinelli, B. M. et al. (2019). JUNO/JIRAM's view of Jupiter's H_3^+ emissions. Phil. Trans. R. Soc. A.37720180406.

Drossart, P., et al. (1989), Detection of H_3^+ on Jupiter, Nature, 340, 539–541, doi:10.1038/340539a0.

Ergun, R., et al. (2009). Generation of parallel electric fields in the Jupiter–Io torus wake region. Journal of Geophysical Research. 114. 10.1029/2008JA013968.

Fabiano, F. (2018). Inversion of remote sensing measurements of Middle and Upper Planetary Atmospheres under non-equilibrium conditions. Alma Mater Studiorum Università di Bologna. doi:10.6092/unibo/amsdottorato/8332.

Gérard, J.C et al. (2017). Jovian aurora from Juno perijove passes: comparison of ultraviolet and infrared images. EPSC2017-1004.

Grodent, D., et al. (2003). Jupiter's main auroral oval observed with HST-STIS, J. Geophys. Res., 108(A11), 1389, doi:10.1029/2003JA009921.

Grodent, D., et al. (2008). Jupiter's changing auroral location. Journal of Geophysical Research (Space Physics). 113. 1206.

Hamilton, D. C., et al. (1980). Detection of energetic hydrogen molecules in Jupiter's magnetosphere by Voyager 2: Evidence for an ionospheric plasma source. Geophys. Res. Lett., 7, 813 - 816.

Ingersoll, A. D., et al. (2004). Dynamics of Jupiter's Atmosphere. Jupiter. The Planet, Satellites and Magnetosphere. 105-128.

Johnson, R., et al. (2017). Jupiter's polar ionospheric flows: High resolution mapping of spectral intensity and line-of-sight velocity of H_3^+ ions. Journal of Geophysical Research 122 (2017): 7599-7618.

Khurana, K., et al. (2004). The configuration of Jupiter's magnetosphere. Jupiter: the Planet, Satellites, and Magnetosphere, edited by F. Bagenal et al., Cambridge Univ. Press, New York.

Kim, S. J. et al. (2015). Hot CH4 in the polar regions of Jupiter. Icarus, 257, 217–220, https://doi.org/10.1016/j.icarus.2015.05.008.

Kivelson, M. G., et al. (2004). Magnetospheric interactions with satellites. Jupiter: Planet, Satellites, and Magnetosphere, (Cambridge University Press), p. 513.

Kivelson, M. (2005). The Current Systems of the Jovian Magnetosphere and Ionosphere and Predictions for Saturn. doi:10.1007/1-4020-4038-5_16.

Lanzerotti, L. J. and Krimigis, S. L. (1986). Comparative magnetosphere. Johns Hopkins A PL Technical Digesc, Volume 7, Number 4.

Louarn, P., et al. (2015). Magnetic Reconnection and Associated Transient Phenomena Within the Magnetospheres of Jupiter and Saturn. Space Sci Rev 187, 181–227 (2015), doi:10.1007/s11214-014-0047-5.

Lunine, J., et al. (2004). The origin of Jupiter. Jupiter. The Planet, Satellites and Magnetosphere.

Maestri, T. (2019). Physics of planetary atmospheres. Alma Mater Studiorum University of Bologna.

Migliorini, A. et al. (2019). H_3^+ characteristics in the Jupiter atmosphere as observed at limb with Juno/JIRAM. Icarus 329 (2019): 132-139.

Modest, M. (2003). Chapter 1 – Fundamentals of thermal radiation. doi:10.1016/B978-012503163-9/50002-3.

Moriconi, M. (2017). Preliminary JIRAM results from Juno polar observations: 3. Evidence of diffuse methane presence in the Jupiter auroral regions: CH4 Emission in Jupiter Auroral Regions. Geophysical Research Letters. 44. 10.1002/2017GL073592.

Mottez, F. et al. (2010). Explanation of dominant oblique radio emission at Jupiter and comparison to the terrestrial case. Planetary and Space Science. 58. 1414-1422. 10.1016/j.pss.2010.05.012.

Mura, A. et al. (2017). Infrared observations of jovian aurora from juno's first orbits: Main oval and satellite footprints. Geophysical Research Letters, 44(11):5308-5316.

Mura et al. (2018). Juno observations of spot structures and a split tail in Io-induced aurorae on Jupiter.\ Science 361, 774–777. doi:10.1126/science.aat1450.

Noschese, R., et al. (2019). Juno/JIRAM: Planning and commanding activities. Advances in Space Research. 65. 10.1016/j.asr.2019.09.052.

Oka, T. (1980). Observation of the infrared spectrum of H_3^+. Phys. Rev. Lett. 45, 531, https://doi.org/10.1103/PhysRevLett.45.531.

Orton, G. S., et al. (2017). The first close-up images of Jupiter's polar regions: Results from the Juno mission JunoCam instrument. Geophys. Res. Lett., 44, 4599–4606, doi:10.1002/2016GL072443.

Radioti, A. (2006). Energetic ion composition and acceleration mechanisms in the magnetosphere of Jupiter. Univ. Zugl.: Braunschweig, doi.org/10.23689/fidgeo-121.

Ridolfi, M. (2013). Modulo "FAM" nel Laboratorio di Fisica Applicata. Alma Mater Studiorum University of Bologna.

Rizzi, R. (2018). Radiative transfer and remote sensing. Università di Bologna.

Rybicki, G., and Lightman, A. (1979). Radiation Processes in Astrophysics (New York, Wiley).

Saur, J. (2003). An acceleration mechanism for the generation of the main auroral oval on Jupiter. Geophysical Research Letters - GEOPHYS RES LETT. 30. 10.1029/2002GL015761.

Stallard, T. et al (2002). On the dynamics of the jovian ionosphere and thermosphere: II. The measurement of h3+ vibrational temperature, column density, and total emission. Icarus, 156(2):498-514.

Steinrueck, M. (2017). The atmosphere of Jupiter. Lunar and Planetary Laboratory, University of Arizona.

Stephens, S. K. (2015). The Juno mission to Jupiter: Lessons from cruise and plans for orbital operations and science return. 2015 IEEE Aerospace Conference, Big Sky, MT, pp. 1-20, doi:10.1109/AERO.2015.7118972.

Stoner, J. O., et al. (2018). Spectroscopy. Encyclopaedia Britannica.

Su, Y. (2008). Electromagnetic interaction between Jupiter's ionosphere and the Io plasma torus. Proceedings of the International Astronomical Union. 4. 271 - 282. 10.1017/S1743921309030610.

Taylor, F. W., et al. (2004). The composition of the atmosphere of Jupiter. Jupiter (F. Bagenal, ed.) Cambridge Univ. Press, pp 59-78.

Tennyson, J. & Miller, S., (1994). H_3^+: from first principles to Jupiter. Contemporary Physics. 35. 105-116. 10.1080/00107519408224454.

van der Meer, F., (2018). Near-infrared laboratory spectroscopy of mineral chemistry: A review. International Journal of Applied Earth Observation and Geoinformation (JAG), Vol. 65, p. 71-78, doi:10.1016/j.jag.2017.10.004.

Vogt, M. (2012). The Structure and Dynamics of Jupiter's Magnetosphere. University of California, PhD thesis.

Wallace, J. M. and Hobbs, P. V, (1997). Atmospheric Science: An Introductory Survey. Academic Press, 1997.

Watson, S. C. et al. (1984). The infrared spectrum of the ν_2 fundamental band of the molecular ion. Canadian Journal of Physics. 62(12): 1875-1885, https://doi.org/10.1139/p84-231.

Zhang, Y. et al. (2016). Theoretical Foundation and Basic Properties of Thermal Radiation. 10.1016/B978-0-12-800966-6.00001-6.

Sitography

https://nssdc.gsfc.nasa.gov

https://www.nasa.gov/

https://astrobiology.nasa.gov/

https://www.jpl.nasa.gov/

https://www.missionjuno.swri.edu/

https://spaceflight101.com/

Acknowledgements

Per concludere questa tesi, vorrei ringraziare chiunque abbia contribuito alla sua realizzazione, a partire dal Prof.re Tiziano Maestri, senza la cui disponibilità questo lavoro non si sarebbe potuto concretizzare. Un ringraziamento speciale va alla Dott.ssa Bianca Maria Dinelli, perché è solo grazie a lei se ho avuto la possibilità di lavorare a ciò che desideravo, ma soprattutto la ringrazio per tutto quello che mi ha insegnato. Altrettanto importante è stata la Dott.ssa Francesca Altieri, che ringrazio per tutto il tempo che mi ha dedicato e per gentilezza e disponibilità sempre dimostratemi. Un grazie sincero va al Dott. Enzo Papandrea, il cui aiuto è stato fondamentale, così come ogni suo consiglio. Un grosso riconoscimento va anche al Dott. Alessandro Mura e al Dott. Federico Fabiano, i cui contributi hanno permesso di realizzare parti importanti di questa tesi, e a chiunque nel JIRAM team abbia avuto anche solo il minimo ruolo in questo progetto.

Non posso che ringraziare la mia amica Giulia Nizzi e i miei colleghi/amici Anna, Eugenio, Federico, Giulia, Leonardo, Lorenzo, Luca, Luigi, Riccardo e Valeria per aver reso questi anni estremamente felici. Infine, il grazie più sentito va alla mia famiglia, che mi ha sempre dato il supporto migliore che si possa desiderare, e ai miei nonni e genitori spetta il pensiero più grande.